Dynamic mechanical properties of metal foams

A thesis submitted to The University of Manchester
for the degree of

Doctor of Philosophy

in the Faculty of Engineering and Physical Sciences

2005

Puay Joo, Tan

School of Mechanical, Aerospace and Civil Engineering

Contents

The main body of this thesis consists of 26,311 words.

Abstract

The dynamic mechanical properties of two commercial aluminium-based foams, viz. Cymat/Hydro (closed-cell) and Duocel (open-cell), were investigated using a direct-impact technique for a range of velocities from 10 to 210 ms^{-1} and are reported in this thesis. Elastic wave dispersion and attenuation in the pressure bar was corrected using a force deconvolution technique. A method for locating the point of densification in the nominal stress-strain curves of the foams is proposed, which then provides a consistent framework for the definition of the plateau stress. Data for the uniaxial, plastic collapse and plateau stresses are presented and they show that the plastic collapse strength changes significantly with compression rate. This phenomenon is discussed, and the distinctive roles of microinertia and 'shock' formation are described. The effects of compression rates on the initiation, development and distribution of cell crushing are also examined. Tests were carried out to study the effects of density gradient and of specimen gauge length at different rates of compression and the results are discussed. The origin of the conflicting conclusions in the literature on the correlation between nominal engineering strain rate and the dynamic mechanical properties of aluminium foams is identified and explained.

One-dimensional 'steady-shock' models based on a rate-independent, rigid, perfectly-plastic, locking (r-p-p-l) idealisation of the quasi-static stress–strain curves of the foams are formulated for two different impact scenarios to provide a first-order understanding of the dynamic compaction process. A thermo-mechanical approach is used in the derivation of their governing equations. Predictions by the models are compared with experimental data and with the results of finite-element simulations of two-dimensional Voronoi honeycombs. A kinematic existence condition for continuing 'steady-shock' propagation in the foams is established using thermodynamics arguments and its predictions compare well with the experimental data. Finally, the energy formula from thermodynamics is used to highlight the apparently incorrect energy balance approach to describe 'shock' propagation in cellular materials which appears in some current literature.

Declaration

I declare that no portion of the work referred to in the thesis has been submitted in support of an application for another degree or qualification of this or any other university or other institution of learning.

Copyright Statement

Acknowledgements

The theme of this thesis is a seismic shift from the original intention of studying the resistance of wood to free-flying projectiles. This led to a protraction of the research work which would, otherwise, not have seen fruition without the unstinting support and encouragement of Prof. Stephen Reid to whom the author wishes to acknowledge here his indebtedness.

The author has greatly benefited from the advice, comments and critical readings of sections of the thesis by many helpful colleagues and friends; in particular, he would like to acknowledge those of Prof. Stephen Reid, Drs. Zhenmin Zou, John Harrigan and Shuguang Li of the School of MACE, Manchester; Prof. Magnus. Langseth and Dr. Arve G. Hanssen of the structural impact laboratory at NTNU, Norway; Dr. T. Yella Reddy of Bangalore, India. Comments and suggestions made by anonymous referees have been particularly helpful. The assistance provided by members of the technical staffs; in particular, those of Mr. Paul Tennant, Peter Hassall, Bill Storey and Trevor White are also gratefully acknowledged.

Last, but not least, the author acknowledges the support and encouragement of his parents and siblings throughout the long-drawn-out project.

Chapter 1

Introduction and literature survey

1.1 Introduction

Metal foams are a new, as yet imperfectly characterised, class of materials with low densities and novel physical, mechanical, thermal, electrical and acoustic properties. They offer a plethora of potential applications such as for energy absorption (in packaging and crash protection), for blast-resistant lightweight structures (in the cores of sandwich panels, for example) and for thermal management (Ashby et al., 2000). However, it is in energy absorption and lightweight structures where metal foam appears to hold the greatest promise. When metal foam is loaded in compression, energy is absorbed as their cell walls bend and stretch plastically, or buckle, or fracture (depending on the material of which it is made) and, depending on whether the cells are open or closed, by the compression of the gas within the system of cells. The presence of a long collapse plateau in their compressive load-deflection curve allows the foam to absorb energy whilst keeping the peak force (or deceleration or acceleration) on the packaged object below the limit which will cause damage or injury. Understanding how the topological arrangement of the cell structure in the foam and the material behaviour of the solid phase, relate to the strength properties of a foam and its macroscopic response at different loading rates is, therefore, essential to their successful implementation. Although a sizeable amount of literature on the mechanics of foams exists – an excellent introduction is given in the book by Gibson and Ashby (1997) – there are comparatively fewer studies on the dynamic response of metal foams to impact loadings although it is growing quickly.

The current literature contains conflicting, and sometimes confusing, conclusions on the correlation between loading rate (particularly when referred to the nominal

engineering strain rate $\dot{\varepsilon} \equiv V_i/l_o$, where V_i is the impact velocity and l_o the initial gauge length of the specimen) and the dynamic strength of aluminium-based foams. Kenny (1996) reported that the specific energy absorption of Alcan[1] foams is independent of nominal compression rates from 10^{-3} to $10^3 s^{-1}$ (an impact velocity of $10ms^{-1}$ corresponding to a nominal compression rate of $10^3 s^{-1}$ in his tests); similarly, for Duocel foams (Lankford and Dannemann, 1998; Dannemann and Lankford, 2000). The study by Deshpande and Fleck (2000) on Alulight and Duocel foams showed that their plateau strength remains rate insensitive up to a nominal strain rate of $5 \times 10^3 s^{-1}$ (corresponding to an impact velocity of $50ms^{-1}$). This contradicts the experimental results of Mukai et al. (1999a,b) who reported a 50-100% enhancement of the quasi-static plateau strength in closed-cell Alporas foams for compression rates greater than $10^3 s^{-1}$ (corresponding to an impact velocity of $6ms^{-1}$). The confusion relates to several factors including different interpretations of the underlying mechanisms responsible for dynamic strength enhancement, inconsistencies in the definition of key material parameters such as the strain at which densification occurs, the definition of the plateau strength and, partly, to the choice of experimental technique. The motivation for this study is the need to clarify the underlying inconsistencies in the current literature on the relationship between loading rates and the dynamic properties of metal foams; this need arises because they are used increasingly as materials for energy absorption and in lightweight structures designed to resist blast and impact loadings (Hanssen, 2000; Fleck and Deshpande, 2004; Deshpande and Fleck, 2005). This thesis presents the results of a systematic and extensive investigation into the dynamic mechanical properties of metal foams.

1.2 Outline of the thesis

Almost any metal can be foamed although most commercial metal foams are based on either aluminium or nickel. The dynamic mechanical properties of two

---

[1] Alcan, Duocel, Alulight, Cymat and Alporas are product names of various commercial aluminium-based foams (of either open or closed cells). See Ashby et al. (2000) for information on their manufacturers.

9

commercial aluminium-based foams, viz. Cymat/Hydro[2] (closed-cell) and Duocel (open-cell), are studied in the present thesis. The thesis begins with an evaluation of the basic parameters which characterise the structure of the foams. The limitations of the two common high-rate testing techniques are discussed and the most appropriate technique for metal foams testing is highlighted. A description of the test apparatus follows and an account is given of the deconvolution technique used to correct the measured force pulses for elastic wave dispersion and attenuation in the pressure bar (Chapter 2). Chapter 3 proposes a new method of locating the densification strain based on the *efficiency* of the foam, defined according to its performance, in absorbing energy. This lays the foundation for a consistent framework to which key material parameters can be extracted from the nominal stress-strain curves of any cellular materials without recourse to ad-hoc criteria. The quasi-static and dynamic mechanical properties of the Cymat and Duocel foams are next presented and discussed. In chapter 4, one-dimensional 'steady-shock' models are formulated which enable the dynamic mechanical properties of the metal foams measured under impact loading conditions to be predicted. The predictions by the model are compared with the experimental data and with the results of finite-element simulations of two-dimensional (2D) Voronoi honeycombs. The latter highlights the mechanisms by which metal foams absorb energy under impact loading conditions. Chapter 5 identifies and explains the source of some anomalies which arise between the theory presented in Chapter 4 and those in the current literature. Finally, in Chapter 6, suggestions for further research and conclusions are given.

1.3 A brief survey of recent literature

A number of papers have recently appeared in the literature some of which adds to the confusion on whether or not the dynamic mechanical properties of metal foams are affected by the loading rate and they are summarised in Table 1.1. The common theme in these papers is the characterisation of the foams' dynamic properties (and/or the energy absorbed) in terms of the nominal engineering strain rate at the

---

[2] Cymat and Norsk Hydro had merged their aluminium foam process technologies with the former having acquired all of Norsk Hydro's intellectual property and production assets related to aluminium foam production.

Product name and/or process-routes	Testing technique	Nominal strain rate $\dot{\varepsilon}$ (impact velocity)	Summary of results	Reference
Infiltration process (OC)	SHPB	$10^2 - 10^4\,s^{-1}$ ($1 - 100ms^{-1}$)	• Yield strength and energy absorption of foams insensitive to strain rate	Wang et al. (2006)
Duocel (OC)	SHPB & Direct-impact tests	$250 - 3300s^{-1}$ ($6 - 84ms^{-1}$)	• No significant effect on the plateau stress for the range of strain rate	Lee et al. (2005)
Infiltration (OC) and Powder metallurgy (CC)	SHPB	$500 - 1900s^{-1}$ ($5 - 19ms^{-1}$)	• Plateau stress sensitive to strain rate • Cell size has significant effect on the plateau stress	Yu et al. (2005)
Cymat (CC), M-Pore (OC) & Schunk (CC)	Bi-pendulum impactor	up to $100s^{-1}$ ($2.5ms^{-1}$)	• Plateau strength of Cymat & M-Pore independent of strain rate but not Schunk • Peak stress of Cymat sensitive to loading rate	Montanini (2005)
Cymat (CC)	MTS machine	$10^{-3} - 10^{+1}\,s^{-1}$ (up to $0.5ms^{-1}$)	• Plateau stress insensitive to strain rate	Ruan et al. (2002)
Cymat (CC) & IFAM (CC)	SHPB & Direct-impact tests	up to $910s^{-1}$ ($50ms^{-1}$)	• Mean crushing strength exhibits significant strain rate sensitivity	Zhao et al. (2005)
Powder metallurgy (OC)	SHPB	$700 - 2600s^{-1}$ ($7 - 26ms^{-1}$)	• Both yield strength and energy absorbed increases with increasing strain rate	Yi et al. (2001)

Table 1.1 – Summary of recent literature on the dynamic mechanical properties of metal foams. Note that OC and CC denote open and closed-cell, respectively.

Product name and/or process-routes	Testing technique	Nominal strain rate $\dot{\varepsilon}$ (equivalent velocity)	Summary of results	Reference
Powder metallurgy (CC)	SHPB	up to $2000s^{-1}$ ($24ms^{-1}$)	• Compression flow stress exhibits little or no strain rate sensitivity	Hall et al. (2000)
Alporas (CC)	Not stated	$3.33\times10^{-5}-1.6\times10^{-1}s^{-1}$ ($1.6\times10^{-6}-8\times10^{-3}ms^{-1}$)	• Plastic strength and energy absorbed increase by 31% and 52.5%, respectively, with strain rate	Paul and Ramamurty (2000)
Duocel (OC) & Alporas (CC)	SHPB	$400-2500s^{-1}$ ($7.6-63ms^{-1}$)	• Strain rate effect reported in Alporas especially for high density (15%) foams • No increase in energy absorption at higher loading rates for Duocel	Dannemann and Lankford (2000) ; Lankford and Dannemann (1998)
Alporas (CC)	SHPB	$2500s^{-1}$ ($15ms^{-1}$)	• Yield strength of foam is highly sensitive to strain rate	Mukai et al. (1999a,b)
Alulight (CC) & Duocel (OC)	SHPB & Direct impact tests	up to $5000s^{-1}$ ($50ms^{-1}$)	• Plateau stress is almost insensitive to strain rate	Deshpande and Fleck (2000)
Alcan (CC)	SHPB	up to $1000s^{-1}$ ($50ms^{-1}$)	• Specific energy absorption independent of strain rate	Kenny (1996)

Table 1.1 continued.

temperature of their intended application. Unlike solid metals, the relatively large cell sizes in metal foams (of the order of millimetres) meant that its dynamic properties are dominated by the structural response of the individual cell walls at the meso (cell) scale. It will be shown in Chapter 3 that a direct correlation, similar to the well-known Cowper-Symonds empirical correlation for solid metals, is not viable.

(a)

(b)
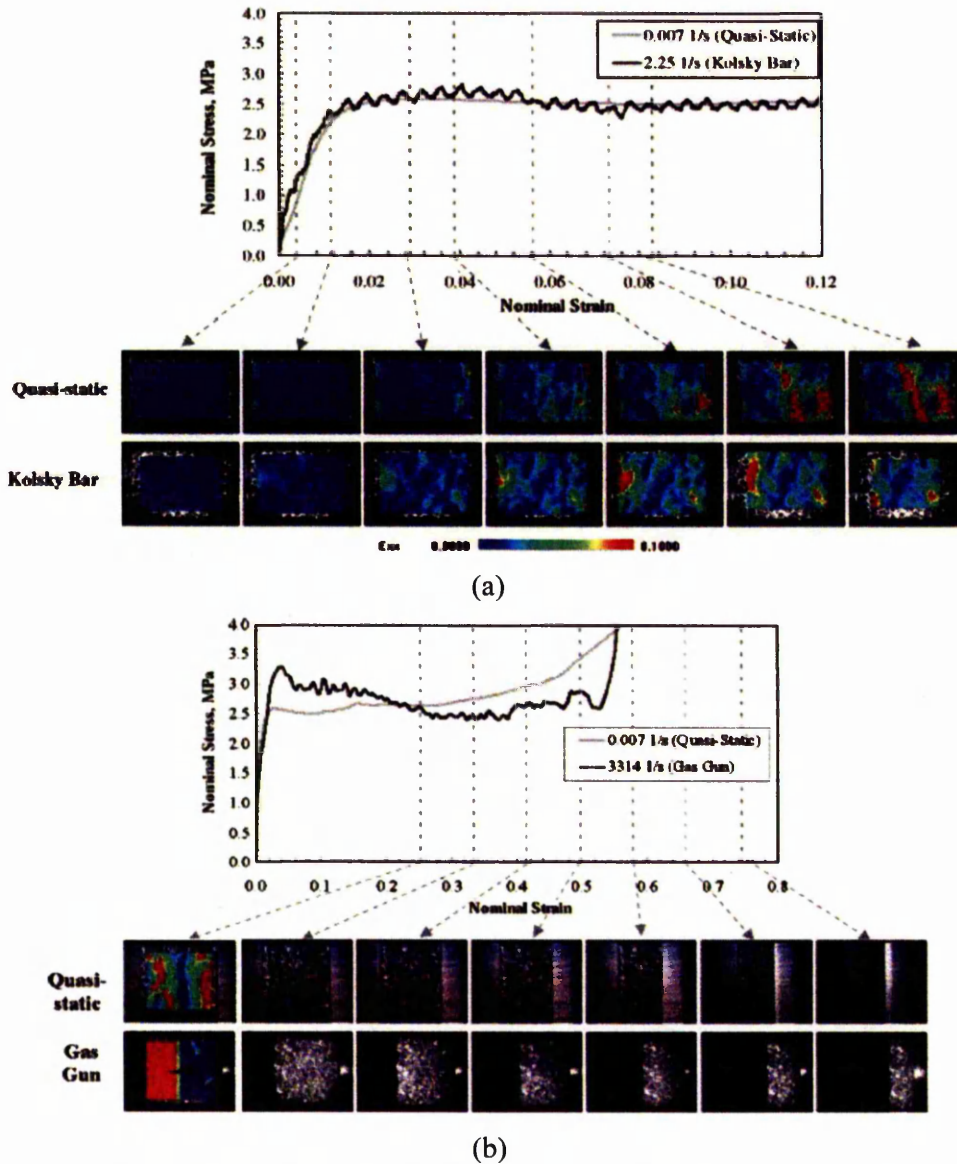
Figure 1.1 – Comparison of the local deformation fields in Duocel foam between those under quasi-static loading and those measured during (a) SHPB and (b) direct-impact tests (reprinted from Lee et al., 2005)

A split-Hopkinson pressure bar (SHPB or Kolsky) apparatus was used in most of the studies listed in Table 1.1 although it is not clear whether the assumptions of force equilibrium and uniform deformation (see Appendix A) were satisfied for their test specimens. *In-situ* measurements of the local deformation (strain) field in Duocel test specimens at different nominal strain rates by Lee et al. (2005) suggest the latter may not have been; see Fig. 1.1. This raises the question of the appropriateness of the SHPB test on metal foams which is addressed in Chapter 2. Also, the ad-hoc nature in which the plateau stress is defined meant that a direct comparison of the data from different studies is often not possible (this is addressed in Chapter 3). Finally, most commercial aluminium-based foams suffer from some form of cell shape anisotropy but no distinction is made of how the properties are affected by the cell orientation in most of those studies.

The mechanical properties of a metal foam are influenced by its relative density and cell structure, particularly by anisotropy and by defects such as wiggly, buckled or broken cell walls, and cells of exceptional size and shape (Ashby et al., 2000). In general, they are independent of the process-route used to make the foams but a recent study by Montanini (2005) appears to suggest otherwise. He reported that the dynamic plateau stresses of the M-Pore and Cymat foams are insensitive to strain rate whilst that of Schunk is sensitive. However, this can be due to differences in the cell microstructure and orientation, arising from the ways in which the foams were manufactured. Of relevance to the present study is his finding that the peak stress, known as the plastic collapse stress in the present study, of Cymat foam changes significantly with loading rate.

A recent paper by Miysohi et al. (2002) suggests that the sensitivity of the measured foam properties to strain rate can be altered by modifying the chemical constituents of the cell wall material. They reported that the plateau stress is "effectively enhanced with the combined effect of strengthening solid alloy and increasing the aspect ratio of cell wall thickness against cell edge length". Note that the latter scales linearly with the relative density (ρ_o/ρ_s, the density ρ_o of the foam divided by that of the solid of which it is made ρ_s) of the foam. Therefore, it is

unclear whether the observed strength enhancement is a result of alloy strengthening or an increase in relative density. They further reported that the plateau stress of the modified foam, after adding strengthening alloys of 0.5 wt.% Mg and 7 wt.% Zn to the aluminium cell walls, is independent of strain rate as opposed to one without. This being the case the plateau enhancement must be due to increase in the relative density of the foam. It is interesting to note that commercial aluminium 6106-T6 alloy, too, contains similar components of the so-called 'strengthening alloy' (see http://www.matweb.com) but it is also well-known that Al 6106-T6 alloy is insensitive to strain rate below $5000s^{-1}$.

Analysing three-dimensional (3D) foams is a difficult business: the cell walls form an intricate three-dimensional network which distorts during deformation in ways which are hard to describe. Two dimensional foams (Voronoi honeycombs) are much easier to analyse and their results shed light on the mechanics of 3D foams. Recent numerical simulations of 2D foams have established an understanding of the mechanisms that will underpin much of the later discussion on the dynamic properties of 3D foams. Ruan et al. (2003) studied the in-plane dynamic compressive response of regular honeycombs through finite element simulations. Three deformation patterns were observed which depends on the direction of loading, the impact velocity and the relative density – they are summarised in a mode classification chart. Of relevance to the present study is the effect of impact velocity on the distribution of cell deformation within the honeycomb structure which is reminiscent of that observed in 3D metal foams – see Chapter 3 of the present thesis.

An interesting recent study is that by Hönig and Stronge (2002a,b). Their simulations on the in-plane dynamic compression of honeycomb reveal the existence of a critical impact velocity beyond which crushing first initiates in the layer of cells adjacent to the impact surface. At velocities lower than the critical value, the location of the initial crush band is determined by the distribution and the extent of initial imperfections in the honeycomb structure. This phenomenon is also observed in 3D metal foams to be discussed later in Chapter 3. Finally, and most importantly, they found that the translational inertia of the cell edges leads to an increase in the

transverse force acting on the row of collapsing cells, leading to an enhancement of the hydrostatic pressure and, consequently, the crushing stress. By contrast, rotational inertia of the cell edges was found to play a negligible role.

Previous works on the dynamic compression of cellular structures (assemblies of metal tubes and honeycombs) and materials (primarily wood) was surveyed in a comprehensive review by Reid et al. (1993). It highlights the common features reflecting the common mechanisms that influence the behaviour of cellular structures and materials under dynamic compression. The central theme is on how microinertia of the cell walls/edges produces force/stress enhancements that are considerably greater than those resulting from the strain-rate sensitivity of the material also apply to the present work on metal foams. The review by Reid et al. (1993) is essential background reading for anyone wishing to gain a further insight into this topic.

1.4 Contributions to existing literature

The bulk of the research work reported in this thesis has now been published and/or presented at symposiums and seminars. A list of the papers published, submitted for publication and currently under preparation in which the present thesis is based is as follows:

1. "Inertial effects in the uniaxial dynamic compression of a closed-cell aluminium alloy foam" (with J.J. Harrigan, S.R. Reid), *Materials Science and Technology* 18 (2002), 480-488.

2. "Dynamic compressive strength properties of metal foams. Part I – Experimental data and observations" (with S.R. Reid, J.J. Harrigan, Z. Zou, S. Li), *Journal of the Mechanics and Physics of Solids* 53 (2005), 2174 – 2205.

3. "Dynamic compressive strength properties of metal foams. Part II – 'Shock' theory and comparison with experimental data and numerical models" (with S.R. Reid, J.J. Harrigan, Z. Zou, S. Li), *Journal of the Mechanics and Physics of Solids* 53 (2005), 2206 – 2230.

4. "Discussion: 'The resistance of clamped sandwich beams to shock loading' (Fleck, N.A. and Deshpande, V.S., 2004, ASME J. Appl. Mech., 71, pp.386-401)" (with S. R. Reid, J.J. Harrigan), *ASME Journal of Applied Mechanics* 72 (2005), 978 – 979.

5. "Dynamic crushing of two-dimensional cellular materials and the effects of irregularities" (with Z. Zou, S.R. Reid, S. Li, J.J. Harrigan), Submitted (2005).

6. "On the mechanical strength properties of materials with a densification regime" (with S.R. Reid, Z. Zou), In preparation (2005).

7. "Dynamic crushing of honeycombs and features of shock wave front" (with Z. Zou, S.R. Reid, S. Li, J.J. Harrigan), In preparation (2005).

8. "Influence of cell size and morphology on the dynamic compressive strength of aluminium alloy foams" (with J.J. Harrigan, S.R. Reid), In *Cellular Metals and Metal Foaming Technology* (J. Banhart, M.F. Ashby, N.A. Fleck, Eds.), Verlag-MIT Publishing, Bremen (Germany), (2001) pp. 345-350.

9. "The crushing strength of aluminium alloy foam at high rates of strain" (with S.R. Reid, J.J. Harrigan), Invited Lecture, *Proc. 4th Int. Symposium on Impact Engineering*, Kumamoto, Japan, 16-19th July 2001, Elsevier Science.

10. "Effects of non-periodic microstructure and imperfections on the dynamic response of two-dimensional cellular materials" (with Z. Zou, S. Li, J.J. Harrigan, S.R. Reid), *Mechanics and Materials Conference*, Scottsdale, Arizona, 17-21st June 2003.

11. "High-rate compaction of aluminium alloy foams" (with J.J. Harrigan, Y.C. Hung, N.K. Bourne, P.J. Withers, S.R. Reid, J.C.F. Millet, A.M. Milne), In *Shock Compression of Condensed Matter* (M.D. Furnish, Editor), American Institute of Physics, Melville, New York (2005).

It is hoped that the dissemination of the work reported herein will lead, in some ways, towards a better understanding of how the cell features and the structural response at the meso-scale affects the dynamic mechanical properties of metal foams, and of the way these properties could be exploited in the engineering design for energy absorption and shock-resistant sandwich structures.

Chapter 2

Description of materials, force measurement techniques and signal processing

2.1 Introduction

The purpose of this chapter is to present the basic parameters which characterise the structure of the closed and open cell foams, viz. Cymat/Hydro and Duocel respectively, to be studied. The information needed to analyse their properties is contained in a record of the material of which each foam is made, such as their relative density, on whether they have open or closed cells, average cell diameter, shape anisotropy-ratios, etc. (Gibson and Ashby, 1997). They are presented in the form of a characterisation chart for each type of foams. A brief review of the two common experimental techniques used in the high-rate testing of metal foams, viz. the split Hopkinson pressure bar (SHPB) and the direct impact techniques, is given next. The main emphases, however, are to contrast the limitations of each technique, and to discuss important considerations in the design of test specimens. Standard terminologies such as incident/input and transmitter/output bars are used throughout the thesis and they have their usual meanings in the context of a standard SHPB set-up whilst only the latter is used in a direct-impact set-up. Finally, the force deconvolution technique which was employed to correct the dynamic force-time pulses for elastic wave dispersion and attenuation in the pressure bars is reviewed.

2.2 Material Description

The information which characterises each foam material are obtained/measured using standard laboratory apparatus, and those of their micro-structural features were

18

obtained from optical and/or scanning-electron micrographs and using the commercial image-processing software Image Pro®. Further details are available on the respective manufacturers' web-site (see Ashby et al., 2000).

2.2.1 Cymat/Hydro foams

The commercial Cymat/Hydro foams were manufactured using a melt gas injection technique; details of which are given by Ashby et al. (2000). The solid phase (cell wall) material was an aluminium-based alloy of constituents Al – Si (7-9%) – Mg (0.5-1%). It has a density (ρ_s) of $2730 kgm^{-3}$, Young's modulus (E_s) of $70 GPa$ and yield strength (σ_{ys}) of $185 MPa$ (Hanssen, 2000). The three mutually perpendicular principal directions in a typical foam panel, viz. *casting* (x), *transverse* (y) and *gravity* (z), are illustrated in Fig. 2.1. In order to characterise their directional properties, circular cylinders with their axes in either the y or the z directions – their strength differences are greatest between these two directions – were cut from a panel by spark machining. All the cylindrical Cymat specimens had equal gauge length l_o and diameter d_o of approximately 45mm unless stated otherwise.

(a) (b)
Typical foam specimens with
either a z or a y axis.
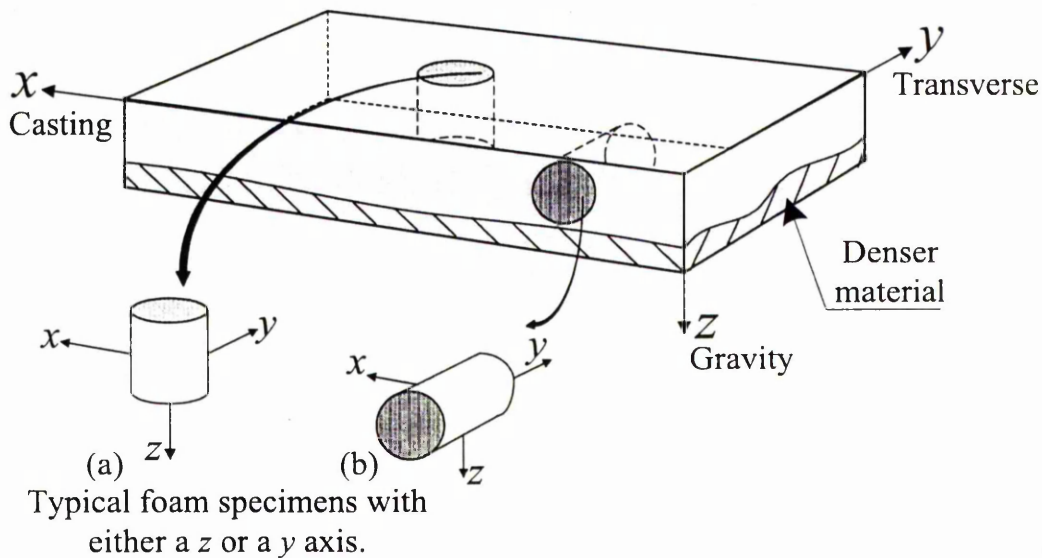
Figure 2.1 – Reference system of a typical Hydro/Cymat foam panel.

The specimens are comprised of approximately equiaxed, closed-polyhedral cells with approximately 10-15 faces. Each cell has an approximate diameter of $d_c = 2 \cdot \sqrt{A_c/\pi}$ where A_c is the projected cell area onto a plane. Figure 2.2 shows the frequency of occurrence, $f(d_c)$, of a given cell diameter d_c, against d_c, for two y-axis specimens with different average cell sizes. The average cell diameter of a specimen is defined by (Gibson and Ashby, 1997)

$$\bar{d} = \int_0^\infty d_c \cdot f(d_c) \mathrm{d}(d_c) , \qquad (2.1)$$

and the cell diameter dispersion (standard deviation) is

$$\mu_{\bar{d}} = \int_0^\infty (d_c - \bar{d})^2 \cdot f(d_c) \mathrm{d}(d_c) . \qquad (2.2)$$
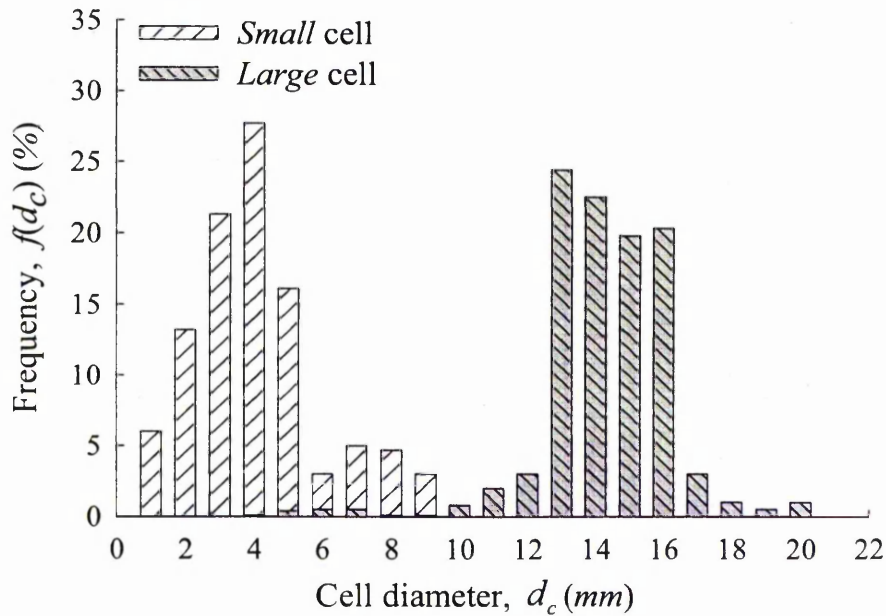
Figure 2.2 – Cell diameter distribution in typical *small* and *large* cell y-axis specimens.

In Fig. 2.2, the two average cell sizes are approximately 14mm and 4mm; for brevity, they will be referred to as *large* cell and *small* cell Cymat specimens, respectively, hereinafter. The former has greater cell diameter dispersion. With the choice of dimensions, the *small* and *large* cell Cymat specimens have more than 10 cells and approximately 3-5 cells, respectively, in the transverse circular plane perpendicular to the direction of compression. Consequently, it is anticipated that the properties of the latter are likely to be affected by size effects – defined as the effect of specimen size, relative to the cell size, on the measured properties (Onck et al., 2001) – and the reasons for studying these specimens will be explained later. Primarily due to the manufacturing process, cylinders of the *large* and *small* cell Cymat specimens have average densities ρ_o that range from $107 - 346$ and $187 - 512 \, kg.m^{-3}$, respectively. Common cell morphological defects, such as missing cells, non-uniform cell wall thickness, fractured cell walls, cell size variations,

Commercial Name	Cymat/Hydro	
Cell wall composition	AlSi8Mg (base alloy), SiC (particle type)	
Density, ρ_0 ($kg.m^{-3}$)	187 - 512	107 - 346
Open or closed cells	Closed	
Average cell diameter, $\bar{d}$ (mm)	4 (*small*-cell)	14 (*large*-cell)
Standard deviation of $\bar{d}$, $\mu_{\bar{d}}$ (mm)	3.51	3.56
Largest principal cell dimension, $\bar{L}_y$ (mm)	4.12	15.96
Smallest principal cell dimension, $\bar{L}_z$ (mm)	3.66	13.25
Intermediate principal cell dimension, $\bar{L}_x$ (mm)	3.87	14.04
Shape anisotropy ratios, R_{yz}, R_{yx}	$R_{yz} = 1.13$ $R_{yx} = 1.06$	$R_{yz} = 1.20$ $R_{yx} = 1.14$
Other specific features	Non-uniform density distribution along the z-axis (see Figure 2.3)	

Table 2.1 – Characterisation chart for Cymat/Hydro foams
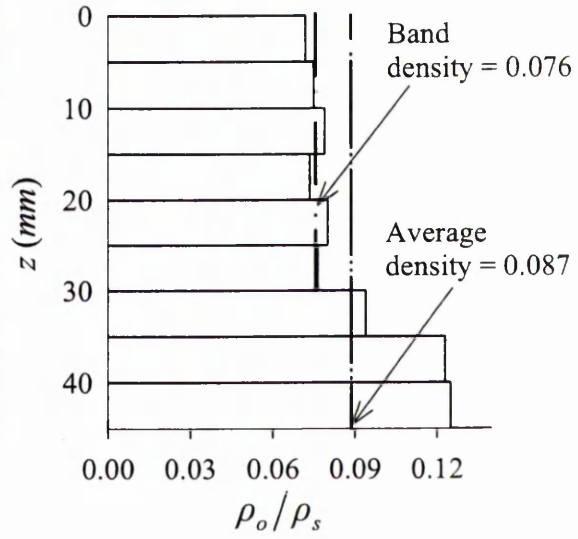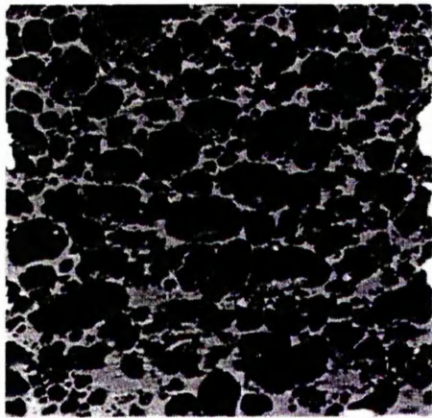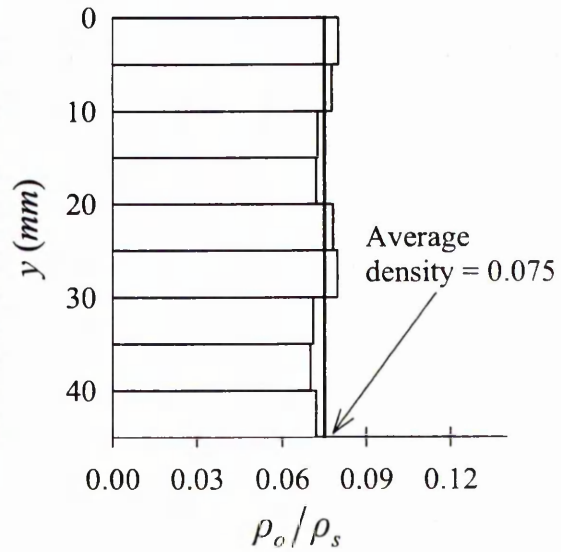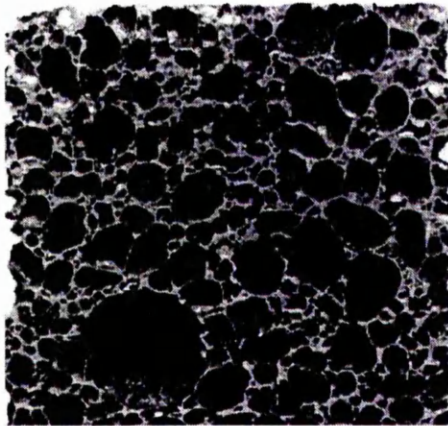
Figure 2.3 – Density distribution in two *small* cell specimens in the (a) *z*, and the (b) *y* direction. Both cylindrical specimens ($l_o = d_o = 45mm$) were sectioned along their respective diametrical mid-plane.

misalignment of cell walls and cell wall waviness, are present in all the specimens (Chen et al., 1999), being most severe in the *large* cell Cymat specimens. A detailed analysis is beyond the scope of the present work; nonetheless, some of the more important cell geometrical characteristics are summarised in Table 2.1.

The density (normalised by the density of the cell wall material ρ_s) distributions along the z-axis and the y-axis of two typical *small* cell Cymat specimens are shown in Figs 2.3a and b, respectively. The former has cell edges (and also their cell faces) that tend to greater thickness in the positive z-direction. This is due to foam drifts caused by alternate impellers rotating in opposite directions during the foaming process (Harte and Nichol, 2001). Specimens with axes aligned along (in) the z-direction are non-homogeneous, with spatial variations of density that have an approximate step-distribution. In contrast, the density distributions in specimens aligned in the y-direction are relatively uniform. The same trend is also observed for the *large* cell Cymat specimens. If the band of cells with greater wall thickness is parallel to the loading axis, it acts to reduce the effects of imperfections by strengthening and stabilising the specimen during compression (Chastel et al., 1999). For this reason the cutting of cylindrical specimens along the y-axis was carried out in a manner in which the denser material at the base of the foam slab is avoided – see schematic in Fig. 2.1b.

Macroscopic anisotropy due to cell elongation in the foam is characterised by the shape anisotropy ratios, $R_{ij} = \overline{L}_i / \overline{L}_j$ and $R_{ik} = \overline{L}_i / \overline{L}_k$, where $\overline{L}_i$ is the largest principal cell dimension and the subscripts i, j and k refer to the three principal directions in Fig. 2.1 (Gibson and Ashby, 1997). The shape anisotropy ratios for the two average cell sizes are listed in Table 2.1. In both cases, the slightly elongated cells have their largest principal dimension in the *transverse* (y) direction. The data for the *small* cell Cymat specimen suggests that the mean cell diameter in the y-direction is marginally larger by factors of $R_{yz} = 1.13$ and $R_{yx} = 1.06$ compared to those in the z and the x directions, respectively. The same can also be said of the *large* cell Cymat specimens but with different factors.

2.2.2 Duocel (ERG) foams

An investment casting method is used to manufacture the Duocel foams although details of the proprietary process remain undisclosed (Ashby et al., 2000). The foam has a reticulated structure of open, duodecahedronal-shaped cells connected by continuous, solid metal ligaments. The ligaments are made of the aluminium alloy Al6106 – T6 which has a density (ρ_s) of $2700 kgm^{-3}$, Young's modulus (E_s) of $70GPa$ and yield strength (σ_{ys}) of $193MPa$. Unlike the Cymat foams, the matrix of cells and ligaments is almost periodic; hence, the test specimens have uniform densities and do not suffer from any obvious cell morphological defects except for minor variations in their cell size and cell elongation. All the Duocel specimens were supplied by ERG as finished circular cylinders of $d_o = 45mm$ and $l_o = 50mm$, unless stated otherwise; they come in two different pore sizes of 10 and 40 pores per inch (PPI) with a corresponding average cell diameter of approximately $4mm$ and $2.0mm$ respectively. Table 2.2 lists some of the relevant information which characterises the Duocel foams.

Commercial Name	Duocel	
Cell wall composition	Al6106 – T6	
Density, ρ_0 ($kg.m^{-3}$)	257 - 287	210 - 271
Open or closed cells	Open	
Average cell diameter, $\bar{d}$ (mm)	4 (10 PPI)	2.0 (40 PPI)
Standard deviation of $\bar{d}$, $\mu_{\bar{d}}$ (mm)	0.2	0.07
Largest principal cell dimension, $\bar{L}_1$ (mm)	5.6	2.7
Smallest principal cell dimension, $\bar{L}_3$ (mm)	3.1	1.8
Intermediate principal cell dimension, $\bar{L}_2$ (mm)	4.1	2.1
Shape anisotropy ratios, R_{12}, R_{13}	$R_{12} = 1.37$ $R_{13} = 1.81$	$R_{12} = 1.29$ $R_{13} = 1.50$

Table 2.2 – Characterisation chart for Duocel foams

Macroscopic anisotropy exists due to cell elongation caused by directional cooling during the casting process (Ashby et al., 2000). Their shape anisotropy ratios are listed in Table 2.2. To investigate whether these affect the strength properties measured, the specimens supplied have either the smallest or largest principal dimension of their constituent cells aligned parallel to the axis of compression. Both directions were investigated for the 10PPI foam; for brevity, a *10PPI-transverse* (*10T*) or *10PPI-longitudinal* (*10L*) specimen denotes one where all their cells are orientated with its smallest or largest principal dimension along the axis of compression, respectively. Photographs of sectioned samples are shown in Figure 2.4. However, only '*40PPI-longitudinal (40L)*' specimens were studied in the present thesis.

(a) *10-PPI transverse*   (b) *10-PPI longitudinal*
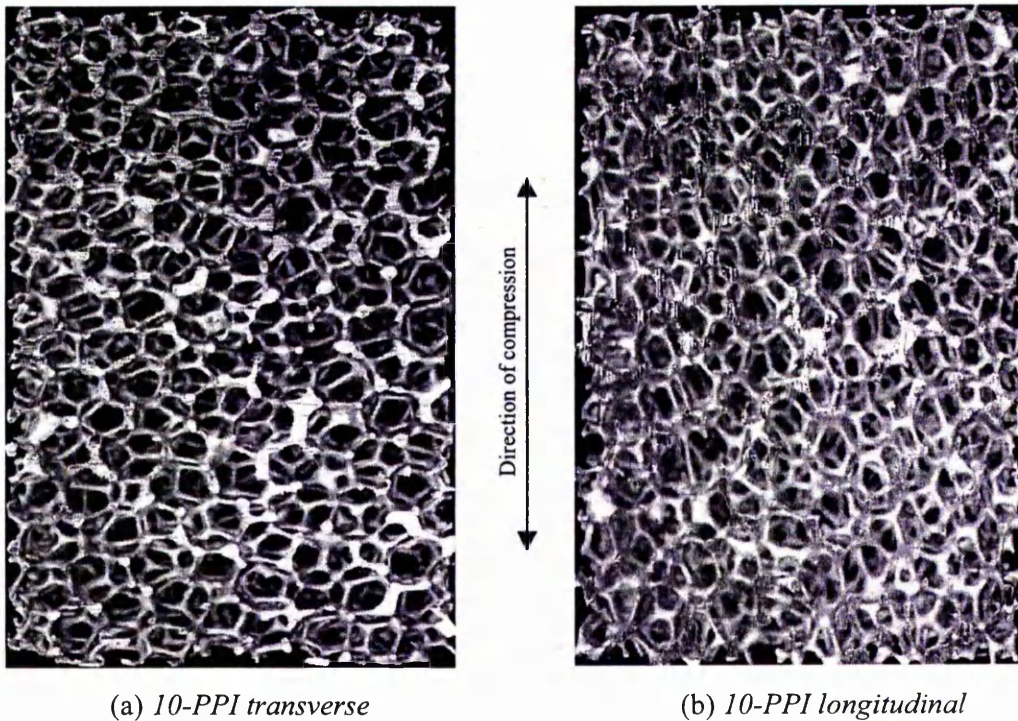
Figure 2.4 – Photographs of two undeformed 10PPI Duocel specimens (40 x 60*mm*) sectioned along their mid plane where the constituent cells have their (a) smallest and (b) largest principal dimension orientated along the axis of compression.

2.3 Force measurement – SHPB versus Direct-impact techniques

The two common experimental techniques used in the high-rate testing of metal foams are the split Hopkinson pressure bar ($200 < \dot{\varepsilon} < 10^4 s^{-1}$) and direct-impact ($10^3 < \dot{\varepsilon} < 10^5 s^{-1}$) tests, where $\dot{\varepsilon}$ is the nominal engineering strain rate defined as the ratio of the change in length of the test specimen. Both are well-established methods and the theory behind each technique is given in Appendix A. The focus here is on discussing their limitations and the important considerations in the design of test specimens with a cellular microstructure.

Both techniques utilise strain-gauged, cylindrical pressure bar(s) as the basis for a mechanical method of measuring stress (or, more precisely, strain) wave pulses generated by impact. The sensitivity of the pressure bar is determined by the properties of the material of the bar (density ρ_b), the type of strain gauge used and the characteristics of the associated instrumentation. Although the bar can be made of any solid material, the elastic wave impedance ($\equiv \rho_o C_e$ where C_e is the elastic wave speed) of the material to be tested usually dictates the choice. Imagine a homogeneous foam specimen (only those aligned along the y-axis for the Cymat foams or any Duocel foams) idealised as a one-dimensional chain of particles of equal mass m ($= \rho_o A_o \overline{d}$) that are interconnected by identical, massless linear elastic springs of stiffness e ($= E_f A_o / \overline{d}$), where E_f is Young's modulus of the foam and A_o is the cross sectional area of the undeformed specimen. If dispersion effects and wave attenuation are neglected then the speed of an elastic wave (plane stress) propagating in this chain is given by (Brillouin, 1946)

$$C_e = \overline{d} \cdot \sqrt{e/m} = \sqrt{\left(E_f / \rho_o \right)}. \tag{2.3}$$

Using Eqn. (2.3) the wave impedance of a typical *small* cell Cymat specimen ($\rho_o = 350 kg.m^{-3}$ and $E_f \approx 1.6 GPa$), assuming the effects of gas compression within the cells are negligible, is estimated to be $\sim 0.75 \times 10^6 kg.m^{-2}.s^{-1}$ and that of a

10L Duocel specimen ($\rho_o = 272 kg.m^{-3}$ and $E_f \approx 0.3 GPa$) to be $\sim 0.29 \times 10^6 kg.m^{-2}.s^{-1}$ - both are two orders of magnitude lower by comparison with that of standard steel ($\sim 40 \times 10^6 kg.m^{-2}.s^{-1}$). The high impedance mismatch suggests that a pressure bar with lower acoustic impedance is needed for the SHPB test. Otherwise, the forces at the specimen-input bar interface cannot be resolved accurately – the incident and reflected force pulses being almost identical and so essentially cancels each other (see Eqn. A10 in Appendix A). The transmitted strain pulse may, as a consequence, become too small to be measured accurately. However one of the difficulties with, for example, polymer bars, such as PMMA, is the need to employ complex geometry-dependent viscoelastic model analysis of the pressure bar signals to deduce the specimen behaviour. This contrasts with the straightforward data reduction if steel bars are used. If, on the other hand, a linear elastic data reduction is used with polymer bars, errors of up to 52% may be expected (Wang et al., 1994). Finally, it is noted that the simplified technique used by Deshpande and Fleck (2000) to justify a linear elastic data reduction may not have fully considered the range of possible signal frequencies encountered during the impact testing of their metal foams (Bacon, 1998 & 1999). Therefore, their results must be treated with caution for the above reason and require further validation.

Careful considerations must also be given to the design of test specimen for a SHPB test; in particular, for a cellular material. The errors due to the radial and the longitudinal inertia of the specimen have to be minimised by choosing a specimen aspect ratio of (Davies and Hunter, 1963)

$$d_o / l_o = 2 / \sqrt{3.v_f}$$
(2.4)

where v_f is the Poisson's ratio: typically between 0.31 – 0.34 for both the Cymat and Duocel foams (Ashby et al., 2000). The errors due to friction at the specimen-pressure bar interfaces must be minimised by reducing the areal mismatch between specimen and bars. A short specimen length is generally required for rapid 'ring-up' (often described as attaining equilibrium) to a uniform uniaxial stress state. If the

27

deformation in the test specimen follows the Taylor-von Karman theory, then the minimum 'ring-up' time is given by Davies and Hunter (1963) to be

$$t \geq \pi \cdot l_o \sqrt{\rho_o / (\partial \sigma / \partial \varepsilon)} \qquad (2.5)$$

where $\partial \sigma / \partial \varepsilon$ is the tangent modulus of the specimen's true stress-strain curve. Although a shorter specimen achieves uniform stress much quicker (Eqn. 2.5), l_o cannot be reduced without a concomitant reduction in both the specimen (Eqn. 2.4) and pressure bar diameters. A minimum diameter ratio of $d_o / \overline{d} \geq 5$ for a metal foam specimen is also necessary to avoid size effect (Onck et al., 2001). As a rule of thumb, it is recommended that the diameter of the test specimen should at least be ten times that of $\overline{d}$. Lastly, the specimen gauge length must be greater than the length scale that defines the continuum limit of the foam (this is to be discussed in Chapter 3). However, it is often not possible for the test specimen to satisfy all of the above criteria and its final design is usually a compromise.

The most important characteristic of the SHPB apparatus is that it allows high strain rate deformation while the test specimen is, in fact, in 'dynamic equilibrium', i.e. the stress gradient is essentially zero along the specimen. This allows the deduction of the dynamic uniaxial stress-strain response on the premise that internal force equilibrium and uniform deformation always exists within the test specimen. Since localisation is a distinctive feature of the deformation of metal foams – this is evident in the local deformation fields of the Duocel foams in Fig. 1.1 – the requirement for uniform deformation of the test specimen in a SHPB test is, strictly speaking, not met initially or at all unless l_o is of the order $O(\overline{d})$. Therefore, the results of a SHPB test on metal foams have to be interpreted with care.

In a direct-impact test, the test specimen is attached to one end of the striker bar (better termed, in this case, the backing mass) and this end is projected by a gas gun so that it impacts the output bar directly. The transmitted wave signal measures the variation of the interface force at the proximal (impact) end of the specimen with

time (see Appendix A) and this is used to deduce the crushing stress in the test specimen. Although this technique increases the maximum loading rate achievable and avoids the dispersion problem in the incident bar it, too, poses several difficulties. Neither the nominal strain nor the nominal strain rate in the specimen can be evaluated without an incident bar. However this limitation may be overcome (see Gorham et al., 1992). A constant strain rate is not achieved because the specimen lacks internal force equilibrium. Therefore, the ratio V_i/l_o is, at best, an overestimate of the actual strain rate in the specimen; nevertheless, it provides a useful value for test design. Just as with the SHPB technique, specimens must also be sized to avoid size effect and specimen length effect. Finally, whilst the direct impact test as described above can be used to measure the force pulse behind the deformation front, the pulse exerted at the support surface of the specimen can be measured by placing the specimen at the end of the output bar and striking it with the input bar. The direct-impact technique is recommended for metal foam testing because, unlike a SHPB test, no assumptions on uniform deformation and force equilibrium within the test specimens need to be made.

2.4 Apparatus and experimental set-up

A thick-walled, tool-steel chamber of 45mm inner diameter was used to stop the premature break-up of the specimens by buckling and/or shear banding during the quasi-static and the dynamic compression tests. In order to reduce the effect of frictional restraint, the contact surfaces between the specimen and pressure bar/chamber were lubricated with PTFE spray. To examine the influence of the radial constraint on the mechanical characteristics of the foam, quasi-static compression tests were carried out using small cell Cymat specimens (at 16% relative density) with (uniaxial strain) and without (uniaxial stress) the radial constraint. The results are plotted in Figure 2.5.

Significant differences between their compressive responses are only observed for the densification régime, i.e. after the point of densification (to be defined in Chapter 3). Because the present study is concerned with the mechanical properties

defined in the pre-densification régime (compare the data for the plastic collapse σ_{cr}^{qs} and plateau σ_{pl}^{qs} stresses in Fig. 2.5), it is concluded that the radial confinement had negligible effect. Likewise, for specimens subjected to dynamic compression. Radford et al. (2005) recently presented a similar comparison for closed-cell Alporas foam and the same conclusion was reached with their data. Similarly, it was found that the mechanical properties of the Duocel foams are also unaffected by the radial constraint.
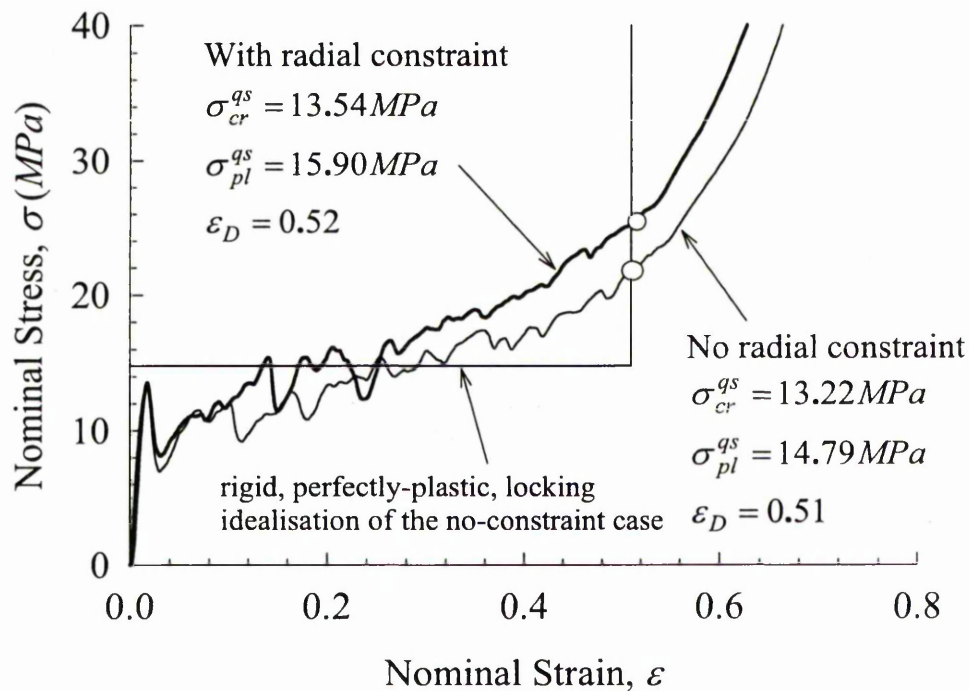
Figure 2.5 - Quasi-static stress-strain curves of Cymat specimens (16% relative density) with and without a radial constraint. The open circle marks the point of densification. The *r-p-p-l* idealisation of the stress-strain curve is plotted for the one without a radial constraint.

Quasi-static compression of the specimens was carried out using an Instron-4507 testing machine under room temperature conditions ($18^{o}C$, 55% relative humidity) at a constant displacement rate $\dot{\delta}$ of $45\mu ms^{-1}$. A direct-impact technique was used for the dynamic compression of the foam specimens. Because a steel output bar was

chosen (due to the more straightforward data reduction), modifications to the original experimental set-up – described in detail by Reid & Peng (1997) – were needed to increase the signal to noise ratio of the strain gauge measurements (the location of the strain gauges on the output bar is shown in Fig. 2.6).

This was achieved in two ways. The diameter of the output bar was reduced to 20*mm*. This increased the strength of the signal. Also the upper frequency limit of the
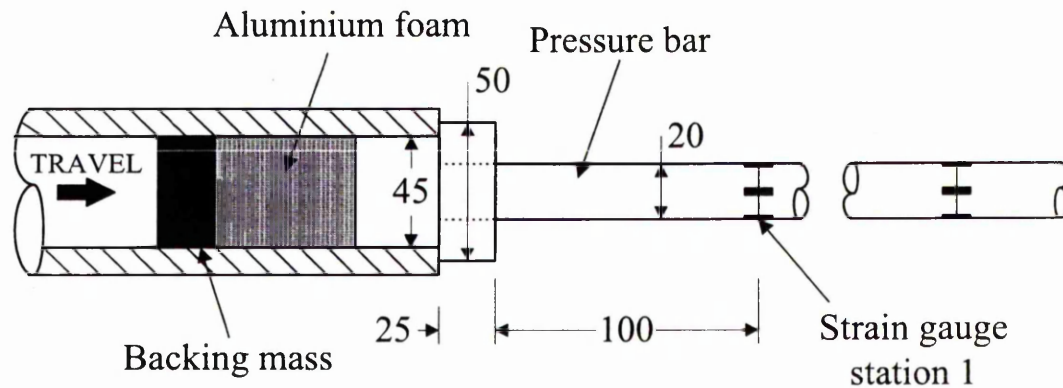
Figure 2.6 – Schematic of experimental set-up for direct impact testing of aluminium foam projectiles.

amplifier ('Fylde' H359-TA) was lowered to 160*kHz* – this reduced the effects of high frequency noise. Because the bar diameter used was then less than those of the specimens, the areal mismatch was dealt with by fitting an anvil of 50*mm* outer diameter (similar to that used in Harrigan et al., 1998c) to one end of the bar (see Fig. 2.6). Both the bar and anvil were made of silver steel. A simple static calibration then allows the conversion of the strain gauge signal into a corresponding force pulse. The gain of the amplifier was 500 and the bandwidth of the oscilloscope (LECROY) was set to its lowest value of 30*MHz*.

An aluminium backing mass (with a diameter of ~45*mm*) was attached to the rear (distal) end of each specimen (see schematic in Fig. 2.6). This has two purposes: it helped with the alignment of the specimen in the barrel of the pneumatic launcher;

and it provided additional kinetic energy for specimen crushing. The biggest possible backing mass that will not yield the pressure bar was chosen for each specimen. It is convenient to introduce a dimensionless mass ratio

$$M_r = M_b/M_f = 4M_b/\pi\rho_o l_o d_o^2 \tag{2.6}$$

where M_f and M_b are the mass of the specimen and backing mass, respectively. In general, a higher mass ratio is needed for complete crushing of the specimen at the lower impact velocities. Useful information is normally restricted to the first 800 μs of the force pulse – known as the bar transit time – because of signal reflection from the free end of the output bar. The bar transit time is determined by the properties of the material of the bar.

2.5 Deconvolution method for the indirect measurement of impact force

Inoue et al. (2001) described an inverse analysis using deconvolution to estimate the impact forces induced by a collision of two bodies of arbitrary shape. Dispersion of the elastic waves in the output pressure bar due to three-dimensional (3D) elastic wave propagation and the presence of the anvil effect the signal oscillations and cause a gradual increase in the rise time of the force pulse with propagation distance. Consequently, the pulse measured by the strain gauges does not accurately reflect the actual force pulse generated at the point of impact (see Fig. 2.6). In this section, the basic principles behind the force deconvolution technique are presented.

A time-dependent force pulse is a superposition of plane waves of many frequencies, each of which will travel at a different velocity when dispersion is present. Assuming that the transfer function is independent of the input amplitude and of the presence and absence of any other frequency components, there then exists a linear mapping of the unknown force pulse $F_c(t)$, generated at the common plane of impact, onto $F_m(t)$, measured by the strain gauges. They are related to each

other according to the convolution or Faltung's theorem as follows (Arfken and Weber, 1995):

$$F_m(t) = \int_0^\infty \Phi(t - \tau) F_c(\tau) d\tau \qquad (2.7)$$

where $\Phi(t - \tau)$ is an amplitude and phase modifying (or transfer) function. The
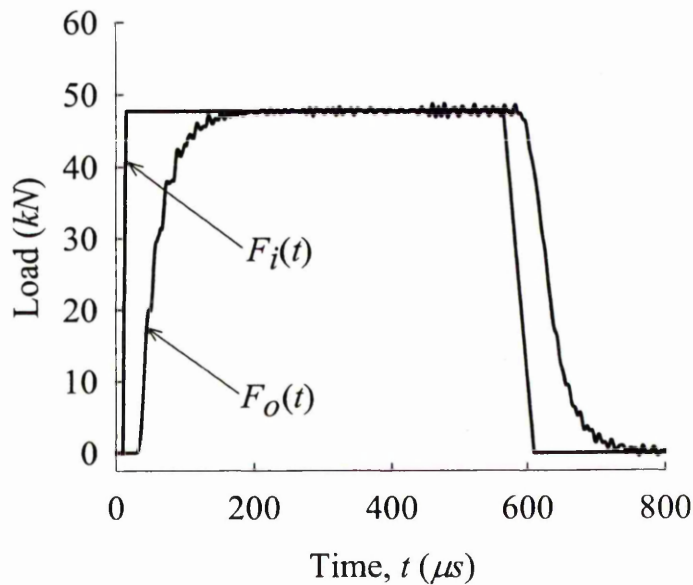
Figure 2.7 – The prediction by *ABAQUS* of the output force pulse $F_o(t)$, measured at strain gauge station 1, for a prescribed input force pulse $F_i(t)$, acting at the specimen-pressure bar interface (Harrigan and Reid, 1998b).

concept of causality is invoked requiring $\tau < t$ in Eqn. (2.7) (Arfken and Weber, 1995). Taking the Laplace transform of the definite integral in Eqn. (2.7) gives

$$\overline{F}_m(s) = \overline{\Phi}(s)\overline{F}_c(s) \qquad (2.8)$$

where the over-bar denotes the Laplace transform of the corresponding function in

Eqn. (2.7).

The transfer function $\overline{\Phi}(s)$ is normally derived from a calibration experiment (Inoue et al., 2001). Here, the approach by Harrigan et al. (1998c) was adopted and the transfer function was derived numerically using finite elements (ABAQUS) because of the practical difficulties with attaching strain gauges to foam projectiles. A numerical calibration also has the advantage over an experimental one in that the calibration process is free from the effects of extraneous noise often associated with such experiments. The accurate specification of the pressure bar geometry, the material properties of the bar (including material damping), the boundary and support conditions in the finite-element model is, of course, critical to its implementation. A mesh sensitivity study was also carried out (see Harrigan et al., 1998c; Inoue et al., 2001). Figure 2.7 shows the difference between the predicted response, $F_o(t)$, at strain gauge station 1, for a prescribed input force pulse $F_i(t)$, acting at the specimen-input bar interface, as predicted by ABAQUS.

Accordingly, the transfer function (in the transform space) is

$$\overline{\Phi}(s) = \overline{F}_o(s)/\overline{F}_i(s).$$ (2.9)

Substituting Eqn. (2.9) into (2.8), and applying the inverse Laplace transform, the unknown force pulse $F_c(t)$ at the point of impact is given by (Inoue et al., 2001)

$$F_c(t) = \frac{1}{2\pi i} \int_{\gamma-i\infty}^{\gamma+i\infty} \left[\overline{F}_i(s) \cdot \overline{F}_m(s)/\overline{F}_o(s)\right] \cdot e^{st} ds.$$ (2.10)

All the Laplace and inverse transformations were carried out numerically by fast Fourier transforms (see Inoue et al., 1992).

All the dynamic force pulses were smoothed, in an 11-point moving average process, before they were corrected by deconvolution (see Harrigan et al., 1998b,c).

34

Figure 2.8 shows typical force pulses of a *small* and a *large* cell Cymat specimen before and after deconvolution. Unlike the former, the corrected force pulses of the *large* cell Cymat specimen fluctuated wildly. For the *small* cell Cymat specimens, noise contributions are typically less than 5.5% of the plateau force measured at an

(a)

(b)
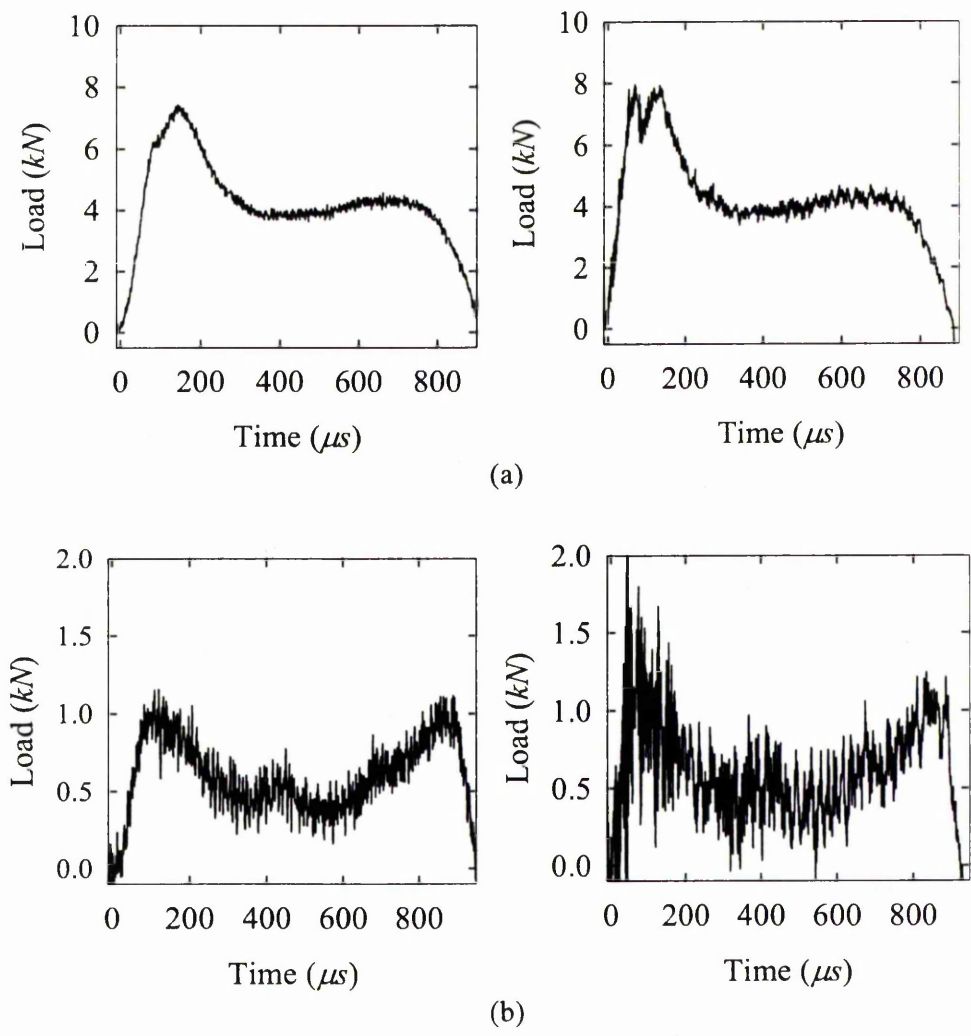
Figure 2.8: Force pulse of a *small* and a *large* cell y-axis Cymat specimen before (left) and after (right) deconvolution (a) *small* cell Cymat specimen, $V_i = 13.44 ms^{-1}$, $\rho_o/\rho_s = 0.122$, $M_r = 16.87$ and, (b) *large* cell Cymat specimen, $V_i = 12.01 ms^{-1}$, $\rho_o/\rho_s = 0.0503$, $M_r = 56.94$.

impact velocity of $13.44ms^{-1}$. Hence, any changes in $\overline{F}_m(s)$ are less significant after inversion as seen in Fig. 2.8a. By contrast, noise contributions are up to 60% of the plateau force in *large* cell Cymat specimens measured at impact velocities of $V_i \leq 20ms^{-1}$ (Fig. 2.8b).

For these reasons, the measured force pulses of all the *large* cell Cymat specimens were not corrected by deconvolution in this study; rather their raw signals were used. It is also worth noting the significant modification to Phase I (defined in Chapter 3) of the deconvoluted force pulse (see Fig. 2.8a). By contrast, Phases II and III appear largely unaffected with only a noticeable increase in noise superimposed on the raw signal. Unlike the Cymat foams, the dynamic force pulses for the Duocel foams were all corrected using deconvolution in the present study.

2.6 Conclusion

The basic parameters which characterise the structure of the Cymat and Duocel foams are summarised in the form of a characterisation chart.

Limitations of each of the two common experimental techniques, viz. SHPB and direct-impact, are contrasted and the reasons for choosing the direct-impact method given. It has been shown that the compressive mechanical properties of the foams, before the onset of densification, are insensitive to a radial constraint. Finally, a review of the deconvolution technique used to correct the force pulses is presented and the reasons for not correcting the measured force pulses of the *large* cell Cymat specimens are given.

Chapter 3

Quasi-static and dynamic mechanical properties of Cymat and Duocel foams

3.1 Introduction

The compression problem is the more important one when designing with metal foams for impact energy absorption. Therefore, only the compressive mechanical properties of the Cymat and Duocel foams are explored in the present thesis. In this chapter, the results of an extensive experimental investigation into the uniaxial compressive characteristics of open (Duocel) and closed-cell (Cymat) aluminium-based alloy foams under quasi-static and dynamic loading conditions are presented. Their dynamic mechanical response were investigated using a direct-impact technique (previously described in Section 2.3), over a range of impact velocities from $10ms^{-1}$ to $210ms^{-1}$.

The role and influence of instabilities in the deformation of constituent cells (this is termed microbuckling to distinguish it from instabilities in the whole specimen), the distinctive role of microinertia (a term commonly used to refer to the inertia of the individual cell walls) and 'shock' formation in the foams are explained. The effects of compression rates on the initiation, development and distribution of cell crushing are also examined. Tests were carried out to examine the effects of density gradient, cell orientation, cell size and specimen gauge length at different rates of compression and the results are discussed. The origin of the conflicting conclusions in the literature on the correlation between nominal strain rate $\dot{\varepsilon}$ (defined as the ratio of the impact velocity V_i to the initial gauge length l_o of the test specimen) and the dynamic strength of metal foams is identified and explained. Both the open and closed-cell foams share similar mechanisms of deformation and compressive strength characteristics. Therefore, only their differences are highlighted; otherwise, it should

be assumed that they apply to both foams.

3.2 Quasi-static compression

To illustrate the range of phenomena involved when metal foam is compressed, the quasi-static response of the Cymat and Duocel foams to uniaxial compression is described first. This also provides a reference point for the subsequent discussion of their respective dynamic test data.

3.2.1 Nominal stress-strain curves

Figure 3.1 shows typical quasi-static compressive stress-strain curves for *small* and *large* cell Cymat specimens in the *y*- and the *z*- directions (see Fig. 2.1). Those of the *10T, 10L* and *40L* Duocel specimens are shown in Fig. 3.2. All stress and strain measures are based on engineering stress and nominal strain definitions. Like all cellular solids, they show linear elasticity at low stresses followed by a 'plateau' region and then a régime of densification in which the stress rises steeply (Gibson and Ashby, 1997). These common features of the curves and the respective mechanism of deformation associated with each regime in the curve are described first. *However, it should be noted here that, whilst their detailed stress-strain response is of intrinsic interest, it is the objective of the present thesis to provide a simplified description of the mechanical properties of the foams, according to the rigid-perfectly-plastic-locking (r-p-p-l) material idealisation in which the foam is characterised mainly by its plastic collapse stress σ_{cr}^{qs}, its plateau stress σ_{pl}^{qs} and its densification strain ε_D, as shown in Fig. 2.5.* The superscript *qs* denotes quasi-static loading conditions. This simplified description of the foams' properties is consistent with its use in energy absorption where the peak force (or acceleration or deceleration) on the packaged object must be kept below a limit that will cause damage or injury (controlled by σ_{cr}^{qs}) and where a large controlled absorption of energy must occur at a nearly constant load (controlled by σ_{pl}^{qs} and ε_D). These three parameters are particularly useful in characterising the dynamic response of the

foams, the focus of this thesis. The material response in the densification regime is, by contrast, of lesser intrinsic interest when designing with foams for impact energy absorption but it has an effect the accuracy of the 'shock' model in Chapter 4.
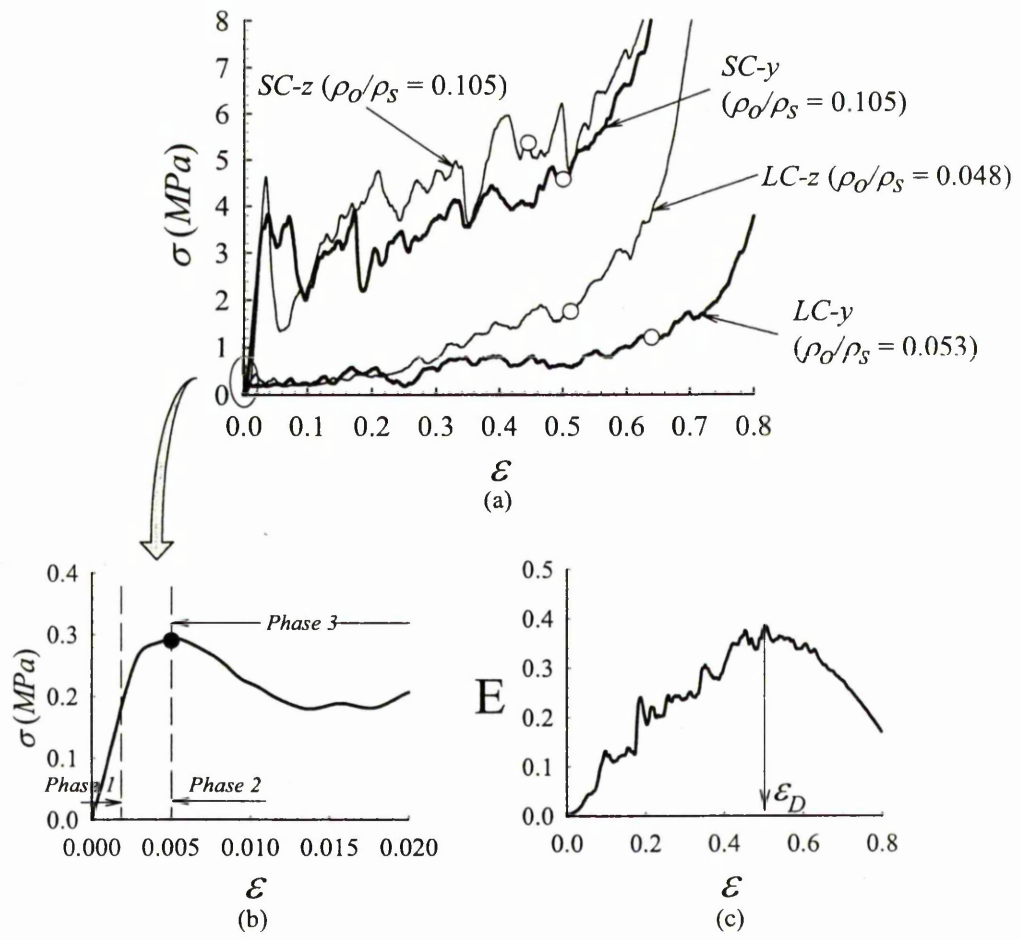
Figure 3.1 – (a) Typical nominal stress-strain curves of *small* cell (*SC*) and *large* cell (*LC*) Cymat specimens compressed along their *y* (thick line) and *z* (thin line) axes. The open circle marks the point of densification.

(b) The three phases of early deformation response in a *large* cell, *y*-axis (*LC-y*) Cymat foam. The solid circle marks the plastic collapse stress.

(c) Efficiency-strain curve for the *SC* Cymat foam compressed along the *y*-axis (*SC-y*).
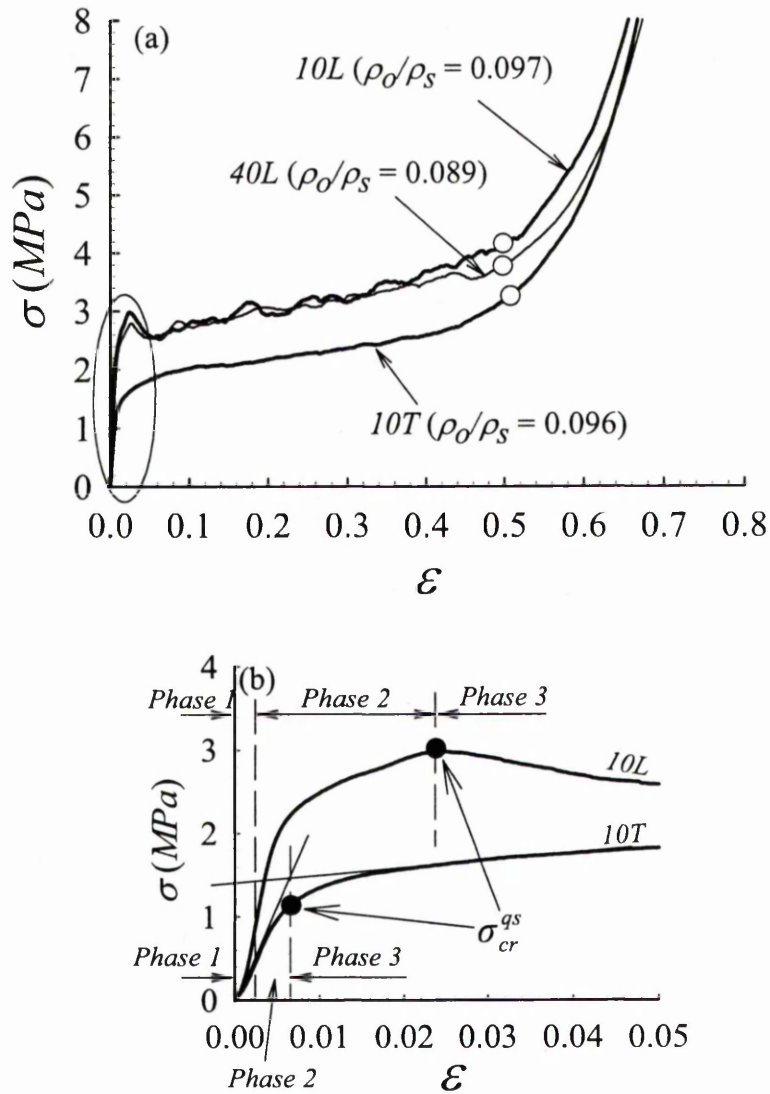
Figure 3.2 – (a) Typical nominal stress-strain curve for *10T*, *10L* and *40L* Duocel
specimens. The open circle marks the point of densification.

(b) Early deformation response of the *10L* and *10T* Duocel specimens
enclosed within the bubble region in (a). The solid circle marks
the plastic collapse stress.

The early compressive response of both foams is divided into three phases – as
shown in Figs. 3.1b and 3.2b. Phase 1 corresponds to linear, elastic straining of the
specimen through cell wall bending and cell face stretching (Gibson and Ashby,

1997), the latter applies to the closed-cell Cymat foams only. This occurs at small nominal strains. Further straining now causes the localised plastic deformation that has developed around small domains of spatially correlated defects to spread and, eventually, coalesce to form bands (or layers) of deforming cells that advance across the specimen. Its cumulative effect is reflected in the non-linear, 'concave-upwards' response of the stress-strain loading path (denoted as Phase 2).

For the Cymat specimens, a stress collapse (or load drop) caused by geometric softening in the plastically deforming cells *always* accompanies the initiation of plastic collapse in the weakest band of cells, at σ_{cr}^{qs}, which marks the beginning of Phase 3. This is analogous to the response of a Type II struct to quasi-static compression (see Calladine and English, 1984). Data for their shape anisotropy ratios (given in Table 2.1) suggest that the load drop which marks the beginning of Phase 3 should be greater for compression in the y- than in the z- direction. But this is not consistently reflected in the curves shown in Fig. 3.1 because of variable geometry of the cell structure. It may, therefore, be assumed that the constituent cells of the Cymat specimens are randomly orientated.

By contrast, stress-collapse does not always occur for the Duocel specimens; it depends on the orientation of constituent cells relative to the axis of compression. If the largest principal dimension of their constituent cells is parallel to the axis of compression, such as in the *10L and 40L* specimens, the early response exhibits analogous Type II structural characteristics; if the loading is parallel to the smallest principal cell dimension (*10T* specimens), they exhibit analogous Type I structural characteristics. Compare, for instance, the early response of typical *10L* and *10T* specimens shown in Fig. 3.2b. The discernible differences in the Phase 3 response of the Duocel foams are due to their highly regular matrix of cells and ligaments. It is interesting to note that similar stages of early deformation response are also observed in wood (a natural cellular material) and in unidirectional fibre-composites (man-made) subjected to uniaxial compression along the grain and along the direction of fibre-reinforcement, respectively. In the former, the differences between the early deformation response of 0° (along grain) and 90° (across grain) wood specimens

41

are reminiscent of those in the *10L* and *10T* specimens, respectively (Reid and Peng, 1997). However, the deformation mechanisms differ in each material and they are discussed in greater detail by Bastawros et al. (2000), Poulsen et al. (1997) and Moran et al. (1995).

The mode of cell collapse *per se* in a 3D foam is too difficult to quantify, unlike for honeycombs subjected to in-plane compression. However, they always invariably involve some form of plastic bending in order to accommodate the large changes of shape of the constituent cells. Visual examination of partially crushed specimens during loading suggests that cell collapse in the Cymat, the *10L* and *40L* specimens is non-symmetric, in a 'shear-type' mode. Non-symmetric cell deformation leads to a decrease in stiffness that results in a maximum load followed by a subsequent plastic loading path with a negative slope as is evident in their respective stress-strain curves in Figs. 3.1 and 3.2 (Papka and Kyriakides, 1994). By contrast, the cells in the *10T* specimens deform in an approximate symmetric mode (c.f. quasi-static lateral compression of a ring) – consistent with the absence of a stress collapse in Phase 3.

When opposing walls of the cells in a collapsing band touch each other, the cells stiffen locally and this triggers the plastic collapse of a non-contiguous band of cells. Localisation of deformation is one of the most distinctive features of cellular materials. Each band appears to develop a spacing of 3-4 mean cell diameters from each other – consistent with the results of surface deformation analysis by Bastawros et al. (2000). For shorter Cymat specimens with a *45mm* gauge length, the crush bands eventually intersect each other and are inclined at angles of approximately 25° to the loading axis. The process of discrete crush band multiplication is repeated, causing stress oscillations in the long 'plateau', though this exhibits gradual overall strain hardening. This region of the stress-strain curves continues until bands of collapsed cells consume the entire specimen; thereafter, the cell wall material itself is compressed. In general, shortening of the specimen in the densification regime occurs in a spatially uniform manner. These observations are broadly similar to the ones made by Bastawros et al. (2000).

The effects of density gradient were examined by comparing the compressive response of the *small* cell Cymat specimens in the *y*- and the *z*- directions (see Fig. 3.1a). First consider the effect of loading direction. The point of densification in each curve is marked with an open circle. As expected, the *z*-axis Cymat specimen densifies at a smaller nominal strain. In this direction, band multiplication is confined, at least in the early phases of compression, to the lower density zone where the density is close to that of a *y*-axis specimen (see Fig. 2.3). Intuitively, this is hardly surprising since the thicker cell edges and cell faces in the higher density band have greater bending stiffness and stretch resistances, respectively. This is also reflected in their stress-strain curves: the plateau stresses in both directions agree within the limits of experimental error (they are seen in both the *small* and the *large* cell Cymat specimens). The *small* cell Cymat specimens are nearly twice as stiff and strong compared to the *large* cell ones because size effects affect the latter. This is explained in a later section.

3.2.2 Quasi-static mechanical properties

The set of moduli that characterises the linear-elastic response of the foams is given by Gibson and Ashby (1997) and, therefore, not repeated here. The literature suffers from a lack of consistency in extracting key material parameters, such as the plateau stress σ_{pl}^{qs} and the densification strain ε_D, from a nominal stress-strain curve. Consequently, the experimental data presented by different researchers are often not suitable for direct comparison because of the different ad-hoc criteria and definitions used. The present development avoids such a problem. The plastic collapse stress σ_{cr}^{qs} is reached when a band of cells start to collapse. This is the first peak stress that separates Phases 2 and 3 in the early deformation response (see Figs. 3.1b and 3.2b). Its corresponding strain is denoted by ε_{cr}. In cases where a load drop does not occur, notably in all the *10T* specimens, the plastic collapse stress is found using a simple graphical construction as illustrated in Fig. 3.2b. If a foam is compressed up to a nominal strain of ε_a, the energy absorbed per unit volume is given by (Gibson and Ashby, 1997)

$$W = \int_0^{\varepsilon_a} \sigma_c(\varepsilon) d\varepsilon . \qquad (3.1)$$

The efficiency E of the foam in absorbing energy is defined as the energy absorbed up to a given nominal strain, ε_a, divided by the corresponding stress value, i.e.

$$E(\varepsilon_a) = \frac{W}{\sigma_c(\varepsilon)]_{\varepsilon=\varepsilon_a}} , \qquad 0 < \varepsilon_a \leq 1 . \qquad (3.2)$$

Finite element (FE) simulations on the in-plane compression of honeycombs have shown that opposing walls of their cells make contact and crush together when the efficiency is a global maximum in the efficiency-strain curve (Tan et al, 2005[3]). This idea can be extended, following arguments consistent with Gibson and Ashby (1997), to the more complex geometry of three-dimensional (3D) foams so that their densification strain ε_D is also defined by (see Fig. 3.1c)

$$\frac{dE(\varepsilon)}{d\varepsilon}\Bigg]_{\varepsilon=\varepsilon_D} = 0 . \qquad (3.3)$$

There are cases where it is necessary to smooth the efficiency-strain curve before locating its stationary point. Since the densification strain is sensitive to spatial variations of density, only the data obtained from the compression of y-axis Cymat specimens were fitted to this definition for densification strain to give (the form of the empirical scaling relation was proposed by Ashby et al., 2000)

$$\varepsilon_D = 0.76[1 - 3.17(\rho_o/\rho_s) + 2.17(\rho_o/\rho_s)^3] . \qquad (3.4)$$

By the same procedure, the densification strain for the Duocel foams is found to be

---

[3] This is the subject of an on-going investigation by the author (see listing in Section 1.4).

44

$$\varepsilon_D = 0.70[1 - 1.50(\rho_o/\rho_s) - 143.14(\rho_o/\rho_s)^3].$$ (3.5)

To define the plateau stress (especially in the light of its application to dynamic loading) the concept of the time average value $\langle f \rangle$ of a smooth and continuous function $f(t)$ is proposed. The strain axis of the stress-strain curve is converted into time by using

$$t = \varepsilon \cdot l_o / \dot{\delta},$$ (3.6)

where the quasi-static compression rate $\dot{\delta} = 45 \mu ms^{-1}$. The plateau stress σ_{pl}^{qs} is
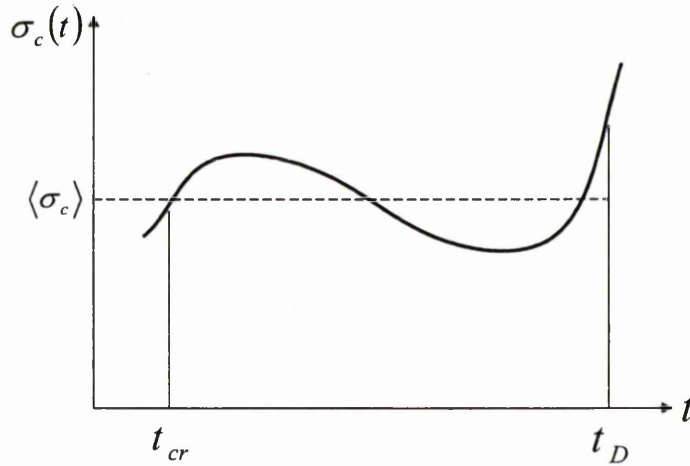
Figure 3.3 – Definition of plateau stress for the function $\sigma_c(t)$.

defined as the time average value of the function $\sigma_c(t)$ so, as illustrated in Fig. 3.3, the rectangular area $(t_D - t_{cr})\langle \sigma_c \rangle$ is equal to the actual area under the curve in the interval $t_{cr} \leq t \leq t_D$, namely

$$\sigma_{pl}^{qs} = \langle \sigma_c \rangle \equiv \frac{1}{(t_D - t_{cr})} \int_{t_{cr}}^{t_D} \sigma_c(t) dt$$ (3.7)

where t_{cr} and t_D is related to ε_{cr} and ε_D, respectively, through Eqn. (3.6). If plastic collapse of the foam results in a perfectly plastic stress-strain response then Eqn. (3.7) gives $\sigma_{pl}^{qs} = \sigma_{cr}^{qs}$, as expected.

The theoretical plastic collapse strength of the closed-cell Cymat foams (ignoring the gas pressure contribution for now) is (Gibson and Ashby, 1997)

$$\sigma_{cr}^{qs}/\sigma_{ys} \approx \underbrace{0.3(\phi\rho_o/\rho_s)^{3/2}}_{\text{plastic bending of cell edges}} + \underbrace{(1-\phi)\rho_o/\rho_s}_{\text{plastic stretching of cell faces}} \tag{3.8}$$

where ϕ is the fraction of solid in the cell edges; the remaining fraction $(1-\phi)$ of solid is contained in the cell faces. Experimental data for the plastic collapse strength of the Cymat foam specimens and the predictions by Eqn. (3.8) (for different values of ϕ) are plotted in Fig. 3.4. The large scatter in the data reflects the sensitivity of the plastic collapse stress to local heterogeneities, such as density variations and cell morphological defects, within the collapsing band of cells. All the data lie close to $\phi \approx 1$: this suggests that they deform primarily by bending of their cell edges – in essence they behave like open-cell foams. Two reasons for this are that the cell faces may have been ruptured before plastic collapse and the contribution from plastic stretching of the cell faces, though still present, is comparatively small and negligible (Gibson and Ashby, 1997). The data for the *large* cell Cymat specimens lies beyond the limiting value of $\phi = 1$. This is because they are affected by cell-size effects, since $d_o/\overline{d} < 5$ for the *large* cell Cymat specimens, which occur in specimens when the reduced constraint of the cell walls at the free surface is coupled with an increased area fraction of stress-free cell walls (see Onck et al., 2001). Due to reasons stated above, the data for the *large* cell specimens, unlike its *small* cell counterpart, cannot be treated as representative of the Cymat foam properties. Rather, their inclusion is to elucidate how cell size affects the static and dynamic strength properties. This is discussed later.

46
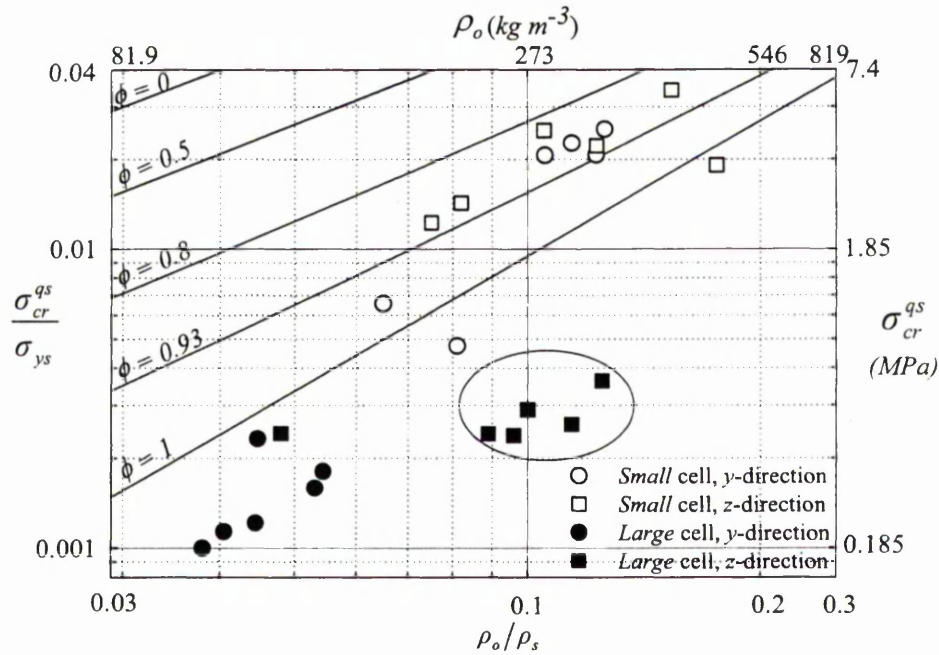
Figure 3.4 – Data for the plastic collapse stress plotted against relative density. The bubble indicates the region of super-imposed density dependence between the *small* and the *large* cell Cymat specimens.

The scaling relation in Eqn. (3.8) requires a unique and single-valued correspondence between the domain of definition (relative density) and the strength property. As pointed out earlier, the z-axis Cymat specimens have strength properties that are lower than their relative density would, normally, predict. This is particularly evident for the *large* cell Cymat specimens (the anomaly is enclosed within the bubble-region in Fig. 3.4). Because of the super-imposed density dependence, separate characteristic curves were used to fit the data for the different average cell sizes. Although the response of the Cymat foam is not perfectly-plastic, the same scaling law was used to fit the data for the plateau strength also. As shown in Fig. 3.4, the dependence of all the strength data on ρ_o/ρ_s are adequately described by Eqn. (3.8) with $\phi = 1$ and there appears to be little evidence of the influence of membrane stress. The percentage scatters in the strength data for the *small* and *large*
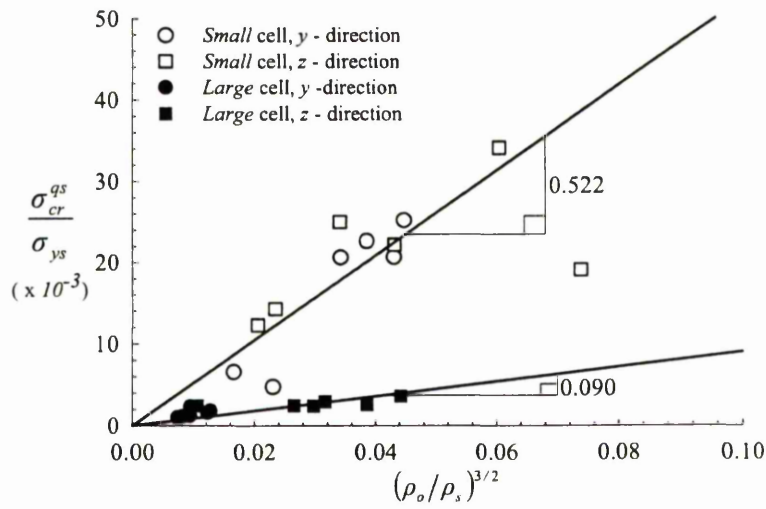
(a)
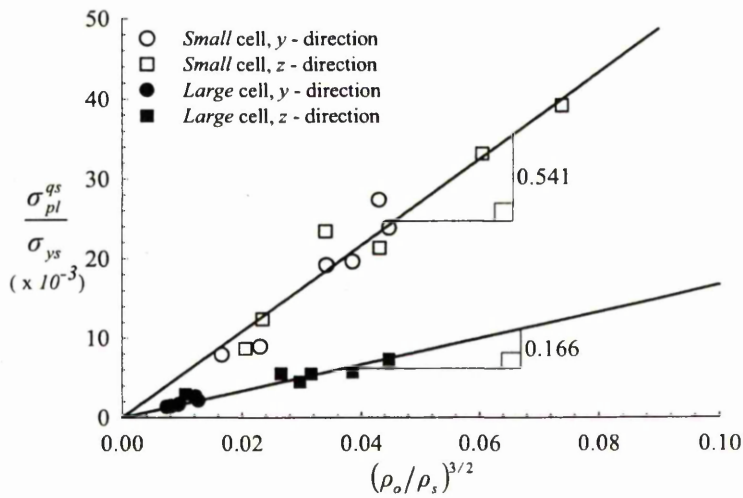
(b)

Figure 3.5 – Data for the quasi-static (a) plastic collapse and (b) plateau stresses (normalised by the yield strength of the cell wall material) of the Cymat foams plotted against relative density $(\rho_o/\rho_s)^{1.5}$. The solid lines represent the scaling relation given by Eqn. (3.8) with $\phi = 1$.

cell Cymat specimens is $\pm 20\%$ and $\pm 40\%$ respectively. By setting $\phi = 1$, the experimental data is fitted to the scaling relation in Eqn. (3.8) to give (see Fig. 3.5)

For *small* cell Cymat foams:

$$\sigma_{cr}^{qs}/\sigma_{ys} = C_1(\rho_o/\rho_s)^{3/2} = 0.522(\rho_o/\rho_s)^{3/2}, \tag{3.9}$$

$$\sigma_{pl}^{qs}/\sigma_{ys} = C_2(\rho_o/\rho_s)^{3/2} = 0.541(\rho_o/\rho_s)^{3/2}, \tag{3.10}$$

and for *large* cell Cymat foams:

$$\sigma_{cr}^{qs}/\sigma_{ys} = C_3(\rho_o/\rho_s)^{3/2} = 0.090(\rho_o/\rho_s)^{3/2}, \tag{3.11}$$

$$\sigma_{pl}^{qs}/\sigma_{ys} = C_4(\rho_o/\rho_s)^{3/2} = 0.166(\rho_o/\rho_s)^{3/2}. \tag{3.12}$$

Unlike the Cymat foams, the quasi-static strength properties of the Duocel foams are sensitive to cell orientation but insensitive to cell size (see Fig. 3.7). In general, significantly higher plastic collapse and plateau stresses were measured along the largest principal dimension of its constituent cells (i.e. in the *10L* and *40L* specimens), as opposed to along its smallest principal dimension (*10T* specimens). This is best explained by an analogy of simpler two-dimensional (2D) honeycomb with principal directions X_1 and X_2 as shown in Fig. 3.6. Assuming deformations are sufficiently small so that changes in geometry are negligible, the plastic collapse stress in the X_1 and X_2 directions is given by (Gibson and Ashby, 1997)

$$\sigma_{cr}^{qs}/\sigma_{ys} = (t/l)^2 \left[1/2(h/l + \sin\theta)\sin\theta\right] \text{ and} \tag{3.13}$$

$$\sigma_{cr}^{qs}/\sigma_{ys} = (t/l)^2 \left[1/2\cos^2\theta\right], \tag{3.14}$$

respectively. For a regular hexagonal honeycomb, i.e. $\theta = 30°$ and $h = l$, Eqns (3.13) and (3.14) predict identical plastic collapse stress in both directions. Suppose the cells are elongated in the X_2 direction with h unchanged from the case where $\theta = 30°$, it is easily verified that $\sigma_{cr}^{qs}/\sigma_{ys}$ is always greater in the X_2 than the X_1 direction, i.e.

$$1/2\cos^2\theta - 1/2(h/l + \sin\theta)\sin\theta > 0 \qquad \text{for } 30° < \theta << 90° \tag{3.15}$$

where $l = h\sqrt{3}/2\cos\theta$. In the 3D Duocel foam, four cell edges meet symmetrically
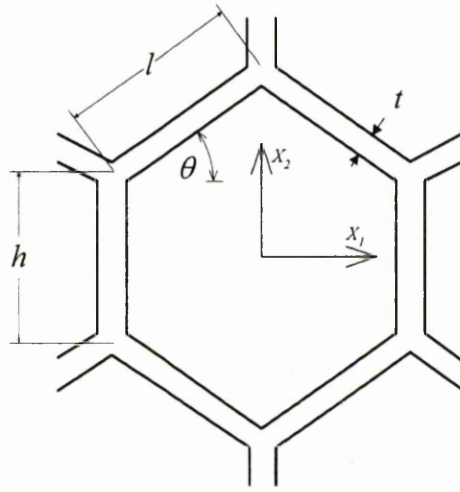
Figure 3.6 – A typical cell of an undeformed honeycomb

at each vertex in a tetrahedral arrangement. Under compressive loading the intricate 3D network of cell edges distorts in ways which are hard to quantify. Nonetheless, the dependence of the plastic collapse stress on cell orientation can be explained by analogy with a simpler 2D honeycomb shown above. The percentage scatter in the data for the plastic collapse and plateau strength of the Duocel foams is approximately $\pm 5\%$ and $\pm 10\%$ respectively. Again, the scaling relation of Eqn. (3.8) can be used to fit reasonably well the experimental data for the Duocel cell foams, by setting $\phi = 1$, to give (Fig. 3.7)

Along largest principal cell dimension (*10L* & *40L* specimens):

$$\sigma_{cr}^{qs}/\sigma_{ys} = C_5(\rho_o/\rho_s)^{3/2} = 0.606(\rho_o/\rho_s)^{3/2}, \tag{3.16}$$

$$\sigma_{pl}^{qs}/\sigma_{ys} = C_6(\rho_o/\rho_s)^{3/2} = 0.708(\rho_o/\rho_s)^{3/2}, \tag{3.17}$$

and along smallest principal cell dimension (*10T* specimens):

$$\sigma_{cr}^{qs}/\sigma_{ys} = C_7(\rho_o/\rho_s)^{3/2} = 0.323(\rho_o/\rho_s)^{3/2}, \tag{3.18}$$

$$\sigma_{pl}^{qs}/\sigma_{ys} = C_8(\rho_o/\rho_s)^{3/2} = 0.481(\rho_o/\rho_s)^{3/2}. \tag{3.19}$$

50
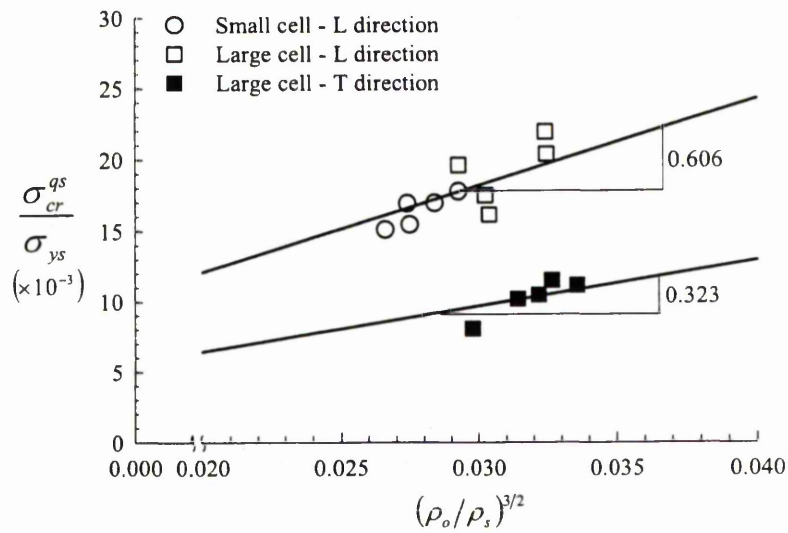
(a)
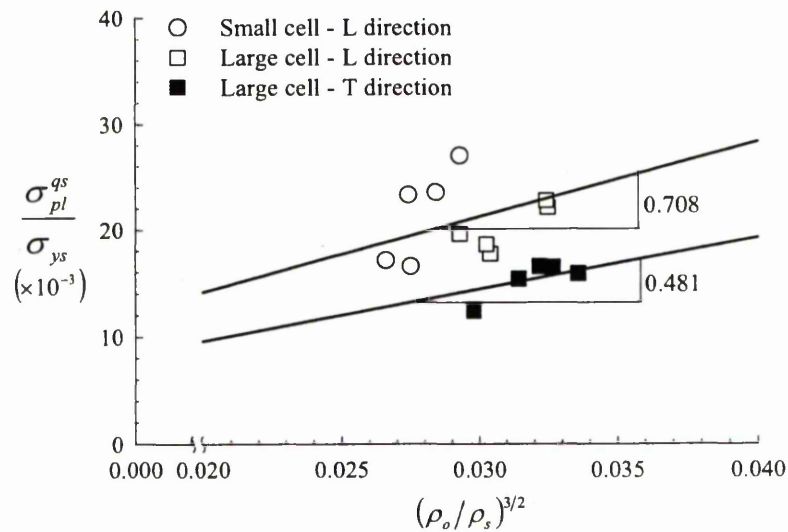
(b)

Figure 3.7 – Data for the quasi-static (a) plastic collapse and (b) plateau stresses (normalised by the yield strength of the cell wall material) of the Duocel foams plotted against relative density $\left(\rho_o/\rho_s\right)^{1.5}$. The solid lines represent the scaling relation given by Eqn. (3.8) with $\phi = 1$.

3.2.3 Gas contributions to the strength properties of Cymat foams

When closed-cell Cymat foam undergoes plastic collapse the fluid in the cells is compressed too. Hence, the gas pressure contribution must be added to Eqn. (3.8). A first order estimate of this can be made by assuming that the ideal gas in the cells undergoes isothermal compression to give a strength elevation of (Gibson and Ashby, 1997)

$$\Delta\sigma = \frac{P_o\varepsilon_D\left(1-2v_f\right)}{\left[1-\varepsilon_D\left(1-2v_f\right)-P_o/\rho_s\right]}$$

(3.20)

where P_o (= 0.1MPa) is the atmospheric pressure. A similar calculation, assuming adiabatic compression, gives (Gibson and Ashby, 1997)

$$\Delta\sigma = P_o\left[\left(\frac{1-\rho_o/\rho_s}{1-\varepsilon_D\left(1-2v_f\right)-\rho_o/\rho_s}\right)^\gamma -1\right]$$

(3.21)

where γ (=1.4 for air) is the ratio of specific heat capacities. For a typical *small* cell specimen ($\rho_o = 350kg\cdot m^{-3}, v_f \approx 0.32, \varepsilon_D = 0.445$), the predicted strength elevation by Eqns. (3.20) and (3.21) is approximately $0.02MPa$ and $0.03MPa$, respectively. Similarly, gas pressure contribution in a typical *large* cell specimen ($\rho_o = 135kg\cdot m^{-3}, v_f \approx 0.32, \varepsilon_D = 0.641$) is approximately $0.03MPa$ and $0.05MPa$, respectively. In each case, the strength elevations are less than their respective limits of experimental error; therefore, following Deshpande and Fleck (2000), it is concluded that the contribution of gas pressure to the measured strength properties of the Cymat foams is so small as to be negligible.

3.3 Dynamic compression

Circular cylindrical foam specimens were compressed dynamically under

uniaxial strain conditions at velocities of up to $210ms^{-1}$. Under impact loading conditions their cells, too, deform by cell edge bending and cell face stretching – depending on whether they are open or closed. However the inertia of the cell walls modifies the local quasi-static collapse mechanism, leading to less compliant modes, which generally require higher loads to cause cell crushing. The response of metal foams with spatially uniform density such as the y-axis Cymat and Duocel specimens is described first.

3.3.1 Dynamic behaviour of foams with uniform densities

3.3.1.1 Force pulses and deformation patterns

Typical force pulses measured at different impact velocities are shown in Figs. 3.8 (for Cymat foams) and 3.9 (for Duocel foams). If the specimens are compressed at a constant rate, then their time and nominal strain axes are linearly related according to Eqn. (3.6) (replacing $\dot{\delta}$ with the impact velocity V_i). In reality, this is only achieved with a sufficiently high mass ratio of $M_r > 100$ (see Chapter 4). If the period of the force pulse (total time required for the specimen to reach densification) is greater than the pressure bar transit time of

$$t = 2l_b \sqrt{\rho_b / E_b} \tag{3.22}$$

where l_b is the distance between strain gauge station 1 and the distal end of the bar, ρ_b is the bar density and E_b is Young's modulus of the bar, then the pulse is truncated by wave reflection, see, for example, (a) and (d) in Figs. 3.8 and 3.9. Deformation of the Cymat and Duocel specimens occurred in three distinct phases: an initial phase leading to peak deceleration (I); a crushing phase (II); and, a densification phase (III) –see Figs. 3.8c and 3.9c. They are analogous to the elastic, plateau and densification regimes of their quasi-static response (see Section 3.2.1).
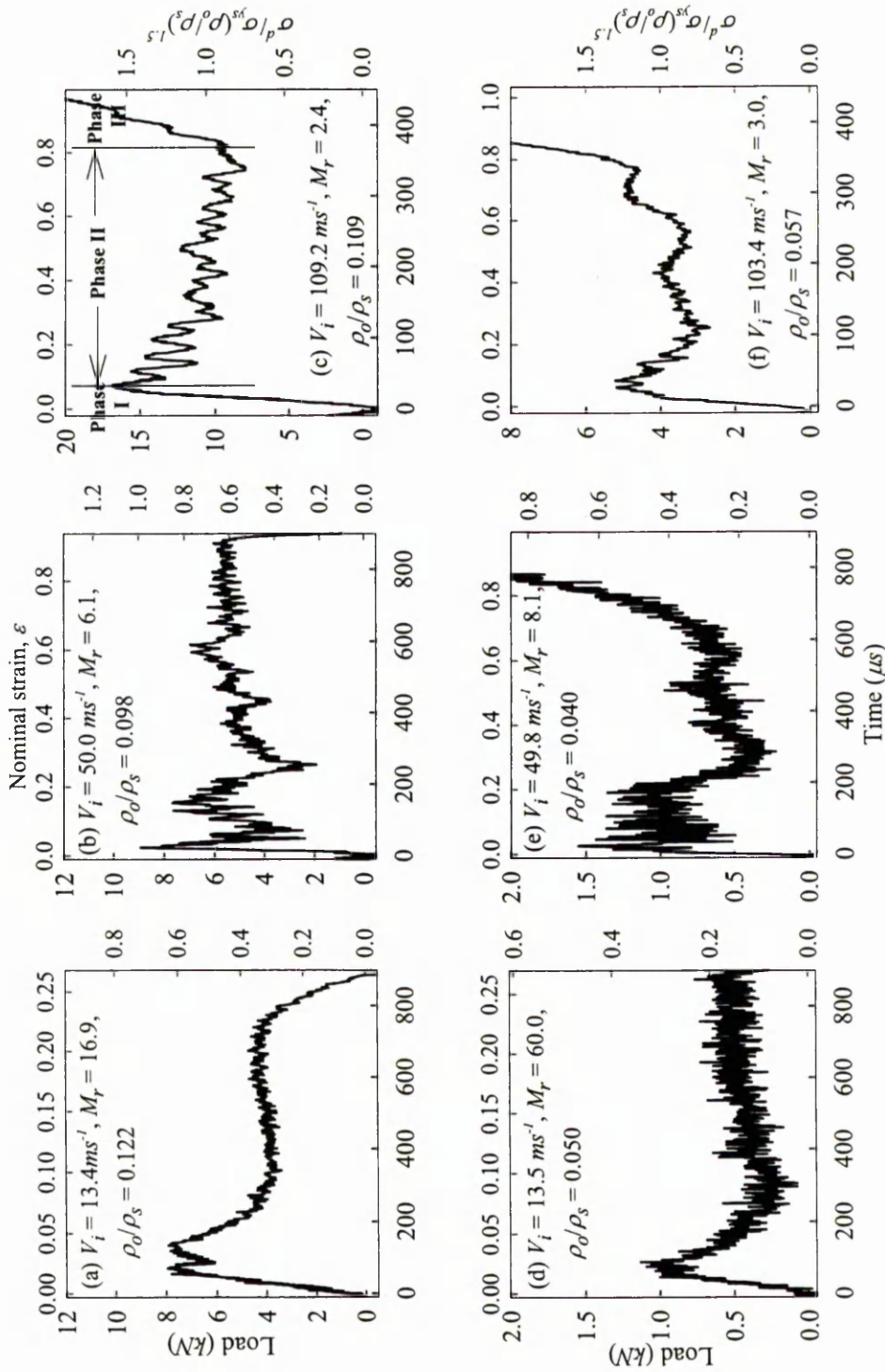
Figure 3.8 – Typical dynamic force pulses for *small* (a-c) and *large* (d-f) cell *y*-axis Cymat specimens measured by direct impact.
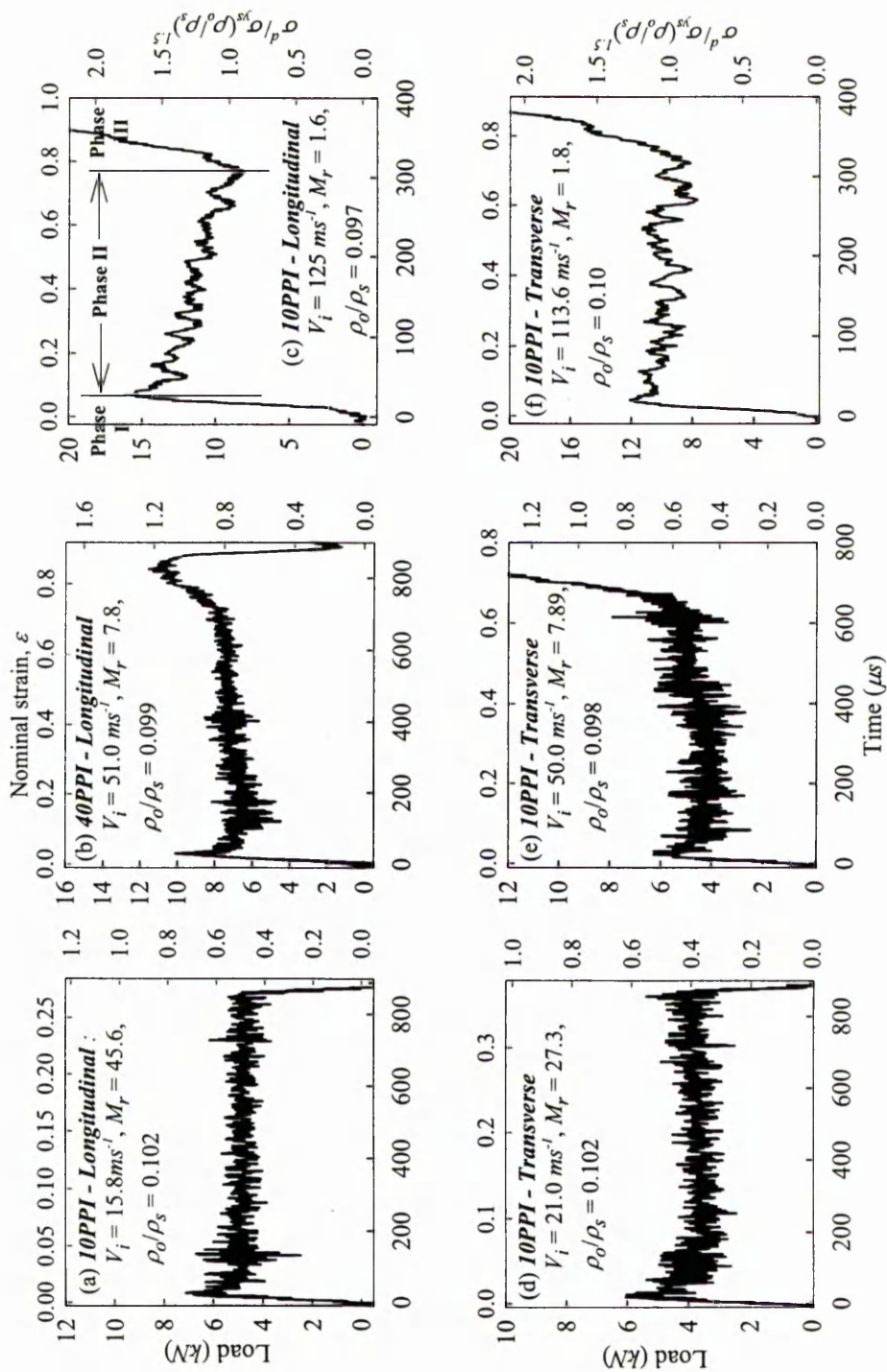
Figure 3.9 – Typical dynamic force pulses for Duocel foams measured along the largest (a-c) and smallest (d-f) principal dimension of their constituent cells.

Phase I deformation corresponds to the initiation of elastic cell deformation by a precursor elastic wave. At cell level, the disturbance propagates as flexural waves in the cell edges and faces; the latter applies to the closed-cell Cymat foams only. Phase II deformation begins when plastic collapse first occurs in a band of cells at the weakest section of the specimen and this is *always* accompanied by a drop in the load. By contrast, this feature is notably absent in the *10T* specimens under quasi-static loading conditions where the load is strictly monotonic increasing – see Fig. 3.2a. This phenomenon is relevant to the accuracy of the 'shock' theory predictions in the next chapter.

Two contrasting distributions of cell deformation and their corresponding force pulses are shown in Figs 3.10 and 3.11. The development and distribution of cell deformation in the foam specimens depends to a large extent on the impact velocity. Two types of deformation pattern develop as follows:

1. *Sub-critical* velocity compression. The first set of foams shows partially crushed *small* cell Cymat (Fig. 3.10a) and *10L* Duocel (Fig. 3.10b) specimens compressed at a sub-critical velocity. Both had insufficient energy to achieve full crushing. Their deformation pattern is similar to those observed under quasi-static loading conditions where crush bands form at random non-adjacent sites leading to non-uniform straining of the specimens. Plastic collapse initiates at the weakest band of cells, almost always in the interior of the specimen. The layer of cells at the impact surface is reinforced by friction through their contact with the anvil and this makes geometric softening in them much more difficult (Papka and Kyriakides, 1994). For this reason, plastic collapse of the cells at the impact surface usually occurs in the latter stages of Phase II deformation. There are, however, exceptions depending on the distribution, the severity and the types of cell defects present. In summary, overall shortening in specimens during sub-critical velocity compression is always by the accumulation of discrete, non- contiguous bands of crushed cells. This leads to a somewhat diffused deformation pattern wherein layers of crushed cells are separated by materials which survive without crushing if the
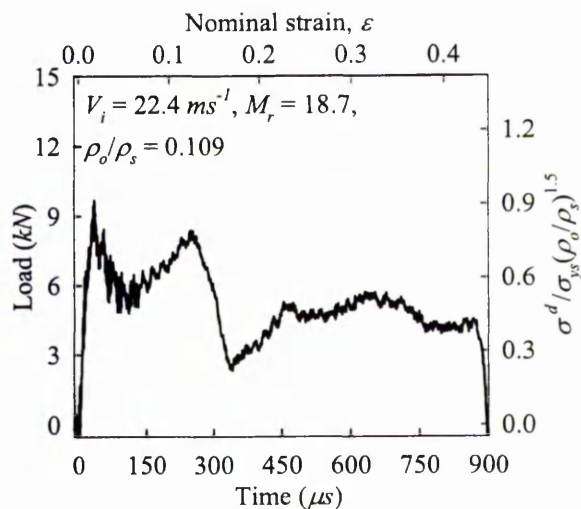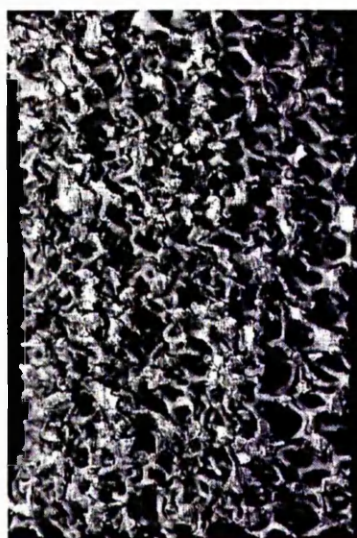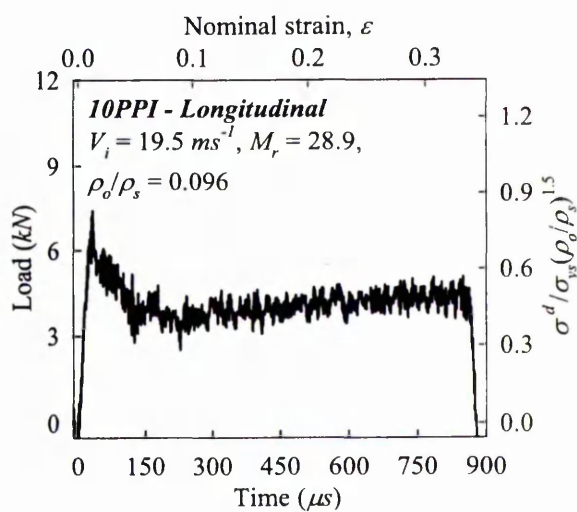
Figure 3.10 – Typical distributions of cell deformation and their corresponding force pulse for (a) *small*-cell *y*-axis Cymat and (b) *10L* Duocel specimens crushed at sub-critical velocities. The discrete crush bands are clearly visible in each specimen. The arrow head denotes the impact end.
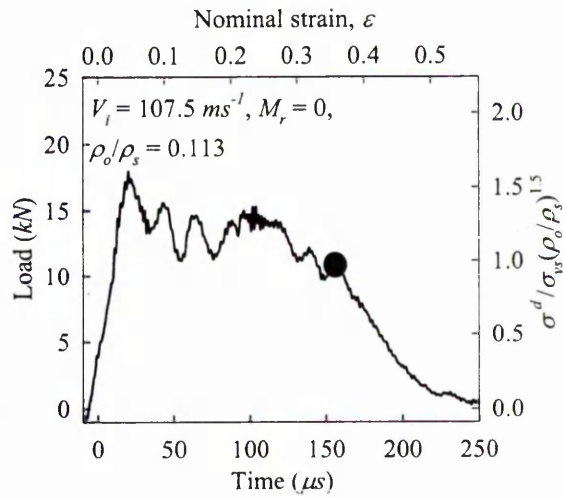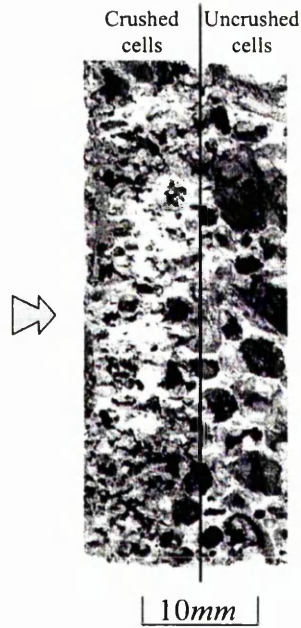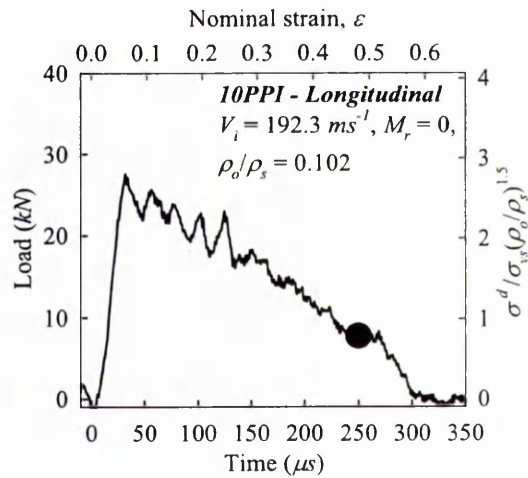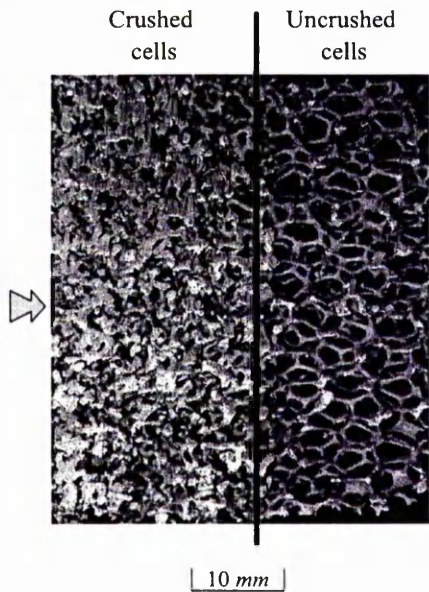
Figure 3.11 – Typical distributions of cell deformation and their corresponding force
pulse for (a) a *small*-cell *y*-axis Cymat and (b) a *10L* Duocel
(specimen gauge length of 100 *mm*) specimen crushed at super-critical
velocities. A planar cross sectional surface separates the crushed and
uncrushed cells. The arrow head denotes the impact end.

specimen is unloaded before Phase III.

2. *Super-critical* velocity compression. Both specimens shown in Fig. 3.11 had no backing mass ($M_r = 0$), similar to a Taylor bullet test. The continuous transit of an elastic wave in the rear portion of each specimen reflected between the crush front and the rear (distal) stress free end eventually brings the specimen to rest after many traversals in the rear part of the specimen. At a super-critical velocity, the impulse generated by impact is so severe that the cells at the impact surface undergo rapid plastic collapse and densify. The residual momentum is then transferred to an adjacent layer of cells, in a 'domino-type' effect, so that cell crushing (or compaction) occurs sequentially, in a planar manner, along the axis of the specimen from the impact-end. This is irrespective of whether the cell deformation mechanism is stable or unstable. With reference to the initial un-deformed configuration of each specimen, a planar cross-sectional surface, separating the crushed and the uncrushed cells, of approximately one cell-width (hereinafter, called the crush front), can be seen to propagate along the axis of the specimen with time. Such a phenomenon is captured by high-speed photography by Radford et al. (2005), and in finite-element simulations of 2D Voronoi honeycombs to be presented in Chapter 4. Because unloading from partially compacted states involves only a small volume recovery, the interface remains visible in the fully unloaded specimen as shown in Fig. 3.11. Since the particle velocity and the deformation gradient (strain) in the specimen suffer rapid, finite changes across a propagating, narrow surface, it is called a 'steady-shock' wave here, idealised as a first-order singular surface (Eringen and Şuhubi, 1974). Under super-critical impact loading, a 'shock' forms immediately in the foam specimens, across which the Rankine-Hugoniot relations are assumed to hold. The typical force pulses measured exhibited successive decreasing peaks with time (more examples of force pulses for specimens compressed at a super-critical velocity are given in Figs. 3.8c, 3.9c and f): they are reminiscent of the results of simulations using a heuristic spring-mass model by Shim et al. (1990). The decreasing peak forces are due to the decreasing momentum flux at the crushing wave front with time. If all the cells in the

specimen have collapsed and the energy of impact is not yet completely dissipated, compression of the cell wall material will occur if $M_r > 0$ and this is reflected in the rapidly stiffening régime of Phase III. Otherwise, Phase III will be absent from the force pulse measured (Fig. 3.11). The time at which the foam specimen starts to unload is estimated using simple momentum considerations and this is marked by the solid circle in Fig. 3.11. It is interesting to note that similar 'shock' type response is, too, observed in the high-velocity crushing of wood, of cellular structures (Reid et al., 1993; Reid and Peng, 1997), and of honeycombs (Reid et al., 1993; Ruan et al., 2003).

The critical velocity corresponding to a transition in the deformation pattern is to be estimated later.

3.3.1.2 Strength properties

The procedure to extract the key material parameters from a dynamic force pulse paralleled that for the quasi-static nominal stress-strain curve closely and is not repeated here. For the same reason given in Section 3.2.2, it must be noted here that only the dynamic data for the *small* cell specimens are representative of the Cymat foam properties. Those of the *large* cell Cymat specimen are used to explain how size effects affect their dynamic strength properties.

(i) Plastic collapse strength

The variation of the plastic collapse stress, σ_{cr}^d, with impact velocity is plotted in Fig. 3.12 for the Cymat foams and in Fig. 3.13 for the Duocel foams. The data is normalised by $(\rho_o/\rho_s)^{3/2}$ to compensate for the effect on the results of variable density between specimens (Ashby et al., 2000). The stress ratio Π ($\equiv \sigma_{cr}^d/\sigma_{cr}^{qs}$) is defined as the ratio of the dynamic to the quasi-static plastic collapse stress. Following the criterion proposed by Deshpande and Fleck (2000), the dynamic stress is said to be enhanced if, and only if, it exceeds the upper limit of the scatter in its

60
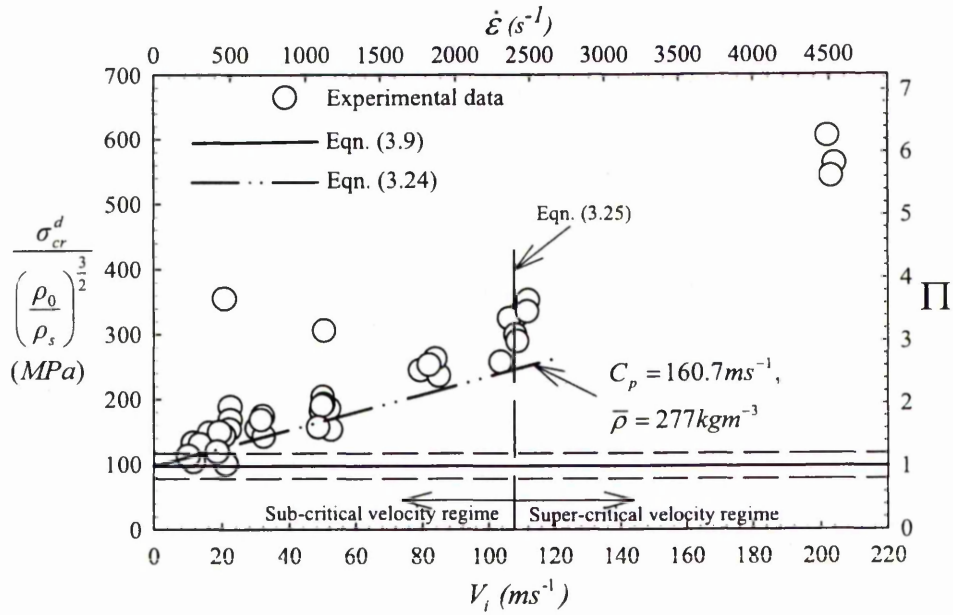
(a)
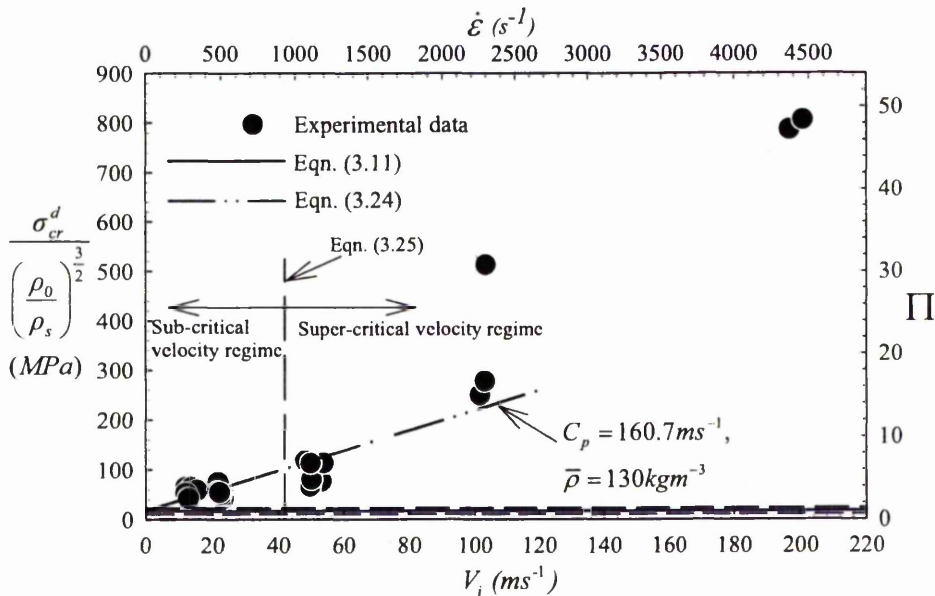
(b)

Figure 3.12 – Variation of the normalised plastic collapse stress $\sigma_{cr}^{d} / \left(\rho_{o} / \rho_{s} \right)^{1.5}$ with impact velocity V_{i} for (a) *small* and (b) *large* cell y-axis Cymat specimens. The dashed lines indicate corresponding quasi-static scatter in loads and $\dot{\varepsilon}$ is the nominal engineering strain rate.
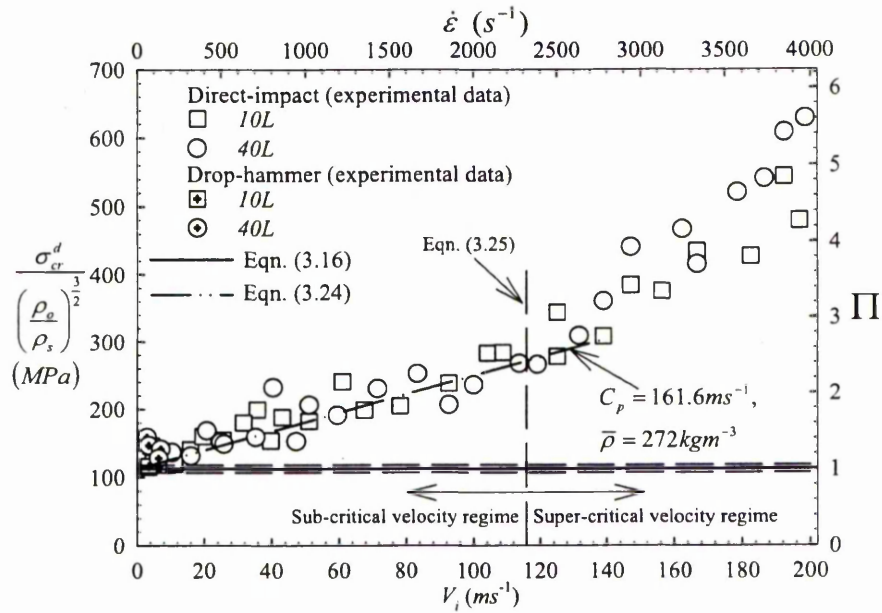
(a)
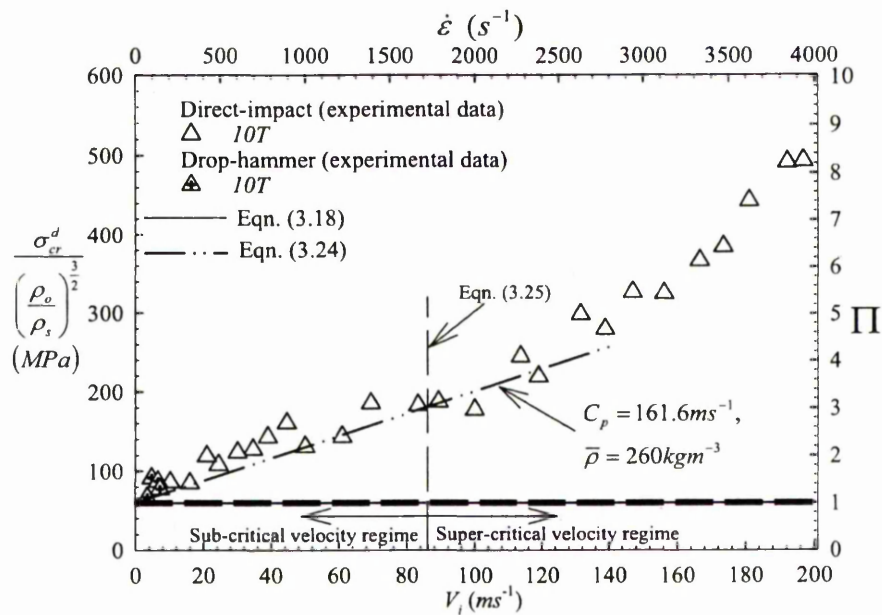
(b)

Figure 3.13 – Variation of the normalised plastic collapse stress $\sigma_{cr}^d/(\rho_o/\rho_s)^{1.5}$ with impact velocity V_i for Duocel foams along the (a) largest and (b) smallest dimension of their constituent cells. Dashed lines indicate corresponding quasi-static scatter in loads and $\dot{\varepsilon}$ is the nominal engineering strain rate.

corresponding quasi-static data. For example, the dynamic plastic collapse stress of a *small* cell Cymat foams is said to be enhanced if $\sigma_{cr}^{d} > 1.2\sigma_{cr}^{qs}$. The percentage scatters in the quasi-static data of both foams are given in Section 3.2.2. Figure 3.12 shows significant enhancement of the plastic collapse strength for both the *small* and *large* cell Cymat specimens over the full range of velocity; likewise, for the Duocel foams along both principal directions of its constituent cells (in Fig. 3.13). Note the enhancement of plastic collapse stress in the *large* cell Cymat specimens (Fig. 3.12b) even though the data were not corrected by deconvolution, i.e. directly from force pulses $F_{m}(t)$ measured by the strain gauges.

Based on calculations in Section 3.2.3, the contribution to the Phase I enhancement by the compression of trapped gas in the Cymat foams is estimated to be small enough to be negligible. Deshpande and Fleck (2000) also found that the nominal strain rate in the cell edges of an open cell foam is approximately an order of magnitude lower than its nominal compression rate $\dot{\varepsilon}$. Since the nominal compression rate was less than $5000s^{-1}$ in all our tests, it is concluded here that material strain rate sensitivity of the aluminium cell walls is also negligible. Herein, the main contention is that inertial/velocity sensitivity is the most dominant effect in the Cymat and Duocel specimens studied.

Microinertia of the cell walls in the foam specimens causes a delay in triggering a buckling collapse mode and/or from the generation of an alternative less complaint cell collapse mechanism than that occurring in quasi-static compression (Reid et al., 1993). Its effect is the analogue of the lateral inertia forces that develop in the arms of a typical Type II strut by introducing an initial phase of deformation where axial plastic compression in the strut dominates (Calladine and English, 1984; Su et al., 1995; Karagiozova and Jones, 1995). A considerable amount of the kinetic energy of the striker mass is absorbed during this initial phase before a bending mechanism predominates. Finite element simulations on the in-plane compression of honeycombs have established that the translational and rotational inertia of the cell edges, as opposed to the lateral inertia forces in a Type II struct, are responsible for such effects. The former was found to play a greater role in the enhancement of the

63

mechanical properties than the latter (Hönig and Stronge, 2002a,b). In the case of 3D foams, such as Duocel, where four cell edges meet at each vertex in a tetrahedral arrangement, the rotational inertia is caused by the three remaining restraining edges as one begins to buckle and rotate; likewise, for the translational inertia. In general, the cell edges in 3D metal foams distort in such complicated ways which are to describe. Because of this, a detailed micromechanical analysis to estimate the additional energy absorbed that can be attributed to microinertia effects may appear futile to do. Nonetheless, a theory capable of providing reasonable estimates of this, especially at the higher impact velocities, will be presented in the next chapter.

The experimental data in Figs. 3.12 (Cymat) and 3.13 (Duocel) shows an approximately linear variation of the plastic collapse stress at the lower impact velocities, in sub-critical velocity régime. This suggests the influence of Type II microinertia effects which is consistent with the stress level being controlled by axial plastic compressive wave propagation in the cell walls in the initial phase of deformation before bending deformation predominates. Suppose the aluminium cell wall has a 'bi-linear' stress-strain relation, then the velocity of this plastic wave is given by

$$C_p \equiv \sqrt{E_p / \rho_s} \qquad\qquad (3.23)$$

where E_p is the plastic modulus. Since $E_p \approx 70.5 MPa$ for Al 6106-T6, the plastic wave speed C_p is approximately $160.7 ms^{-1}$ for the Cymat foams and $161.6 ms^{-1}$ for the Duocel foams. One-dimensional plastic wave theory predicts a linear variation of the dynamic plastic collapse stress with impact velocity according to

$$\sigma_{cr}^d = \sigma_{cr}^{qs} + \overline{\rho} C_p V_i , \qquad\qquad (3.24)$$

where $\overline{\rho} = \sum_N (\rho_o)_N / N$ is the average density of specimens tested. Equation (3.24) appears to fit the experimental data reasonably well at the lower velocities. Calladine

and English (1984) correctly described this phenomenon as a 'velocity' rather than a (nominal) strain-rate effect. The data in Figs. 3.13a and 3.13b also appears to have a similar trend with those of wood studied by Reid and Peng (1997). The stress ratio is greater along the largest compared to the smallest principal dimension of the constituent cells at the same velocity; this is similar to those of 90° and 0° wood specimens. Another similar feature is the load drop in 90° wood specimens after the initiation of crushing; a feature which is missing under quasi-static loading conditions. This, too, is observed here for the *10T* and *10L* Duocel specimens. At higher impact velocities, in the super-critical velocity régime, the linear trend disappears and the plastic collapse strength now has a quadratic dependence on impact velocity (see Figs. 3.12 and 3.13) which suggests that a different inertia phenomenon, associated with the dynamic localization of crushing, is active. It will be shown in Chapter 4 that this is consistent with 'shock' wave propagation.

Foams	Experiment (ms^{-1})	Theory - Eqn.(3.25) (ms^{-1})	Value of relative density in Eqn. (3.25)
Small cell Cymat	~100	108	0.101
Large cell Cymat	~50	42	0.048
10L & 40L Duocel	~110	116	0.100
10T Duocel	~90	85	0.096

Table 3.1 – Comparison between the experimental and predicted critical initial velocity.

As noted in section 3.3.1(i), a switch in the deformation pattern, from discrete crush band multiplication in Fig. 3.10 to progressive cell crushing in Fig. 3.11, occurs when the impact velocity exceeds a critical value of $V_{i-critical}$. It will be shown in Chapter 4 using thermodynamics arguments that, for a *r-p-p-l* material, the critical velocity is given by

$$V_{i-critical} = \left(2C_n \sigma_{ys}/\rho_s\right)^{1/2} \left(\rho_o/\rho_s\right)^{1/4} \varepsilon_D^{1/2} \qquad (3.25)$$

where the subscript $n = 1$ (*small* cell), 3 (*large* cell), 5 (*10L & 40L*) or 7 (*10T*). Table 3.1 compares the experimental and the predicted critical velocity. A good agreement between theory and experiment is observed. The predictions by Eqn. (3.25) separate the data in Figs. 3.12 and 3.13 into two regimes; one where there is an approximate linear dependence with velocity and, the other, a quadratic dependence. This is particularly evident in Fig. 3.13.

(ii) Plateau strength

The plateau stress in Phase II, a time averaged value of the force pulse divided by the cross-sectional area of an undeformed specimen A_o, is associated with the accumulation of bands of crushed cells. Data for the normalised plateau stress ($\sigma_{pl}^d/(\rho_o/\rho_s)^{3/2}$) and the stress ratio ($\Pi \equiv \sigma_{pl}^d/\sigma_{pl}^{qs}$) of the Cymat and Duocel foams obtained at different impact velocities are plotted in Figs. 3.14 and 3.15 respectively. Unlike their plastic collapse strength, they exhibit an approximately quadratic dependence with the impact velocity. The difference between the plastic collapse and the plateau stress of each specimen increases with impact velocity (compare Figs. 3.12 and 3.14 for the Cymat foams and Figs. 3.13 and 3.15 for the Duocel foams), the former being the higher of the two values. At the lower impact velocities the plateau stress measured is lower than its corresponding quasi-static value probably because of the effect of internal elastic wave reflections; however, the reasons for this remain unclear. If the dynamic plateau stress is said to be enhanced only if it exceeds the upper strength limit of their corresponding quasi-static scatter (Deshpande and Fleck, 2000), then Fig. 3.14 shows that the dynamic plateau stresses are insensitive to impact velocity below the values of $\sim 50ms^{-1}$ and $\sim 80ms^{-1}$ for the *large* and *small* cell Cymat specimens, respectively. Likewise, Fig. 3.15 gives $\sim 100ms^{-1}$ and $\sim 60ms^{-1}$ along the largest and smallest principal cell dimension of the Ducoel foams, respectively. To a first approximation, it is reasonable to conclude that the plateau strength of both foams is insensitive to impact velocity in the sub-critical velocity régime. Enhancement of the plateau strength occurs in the super-critical velocity régime where 'shock' propagation effects are important.
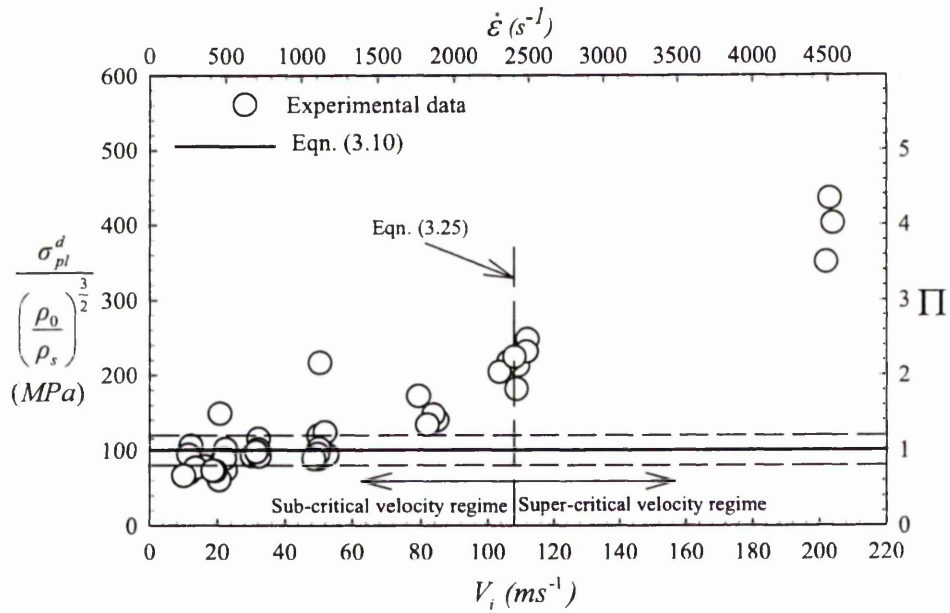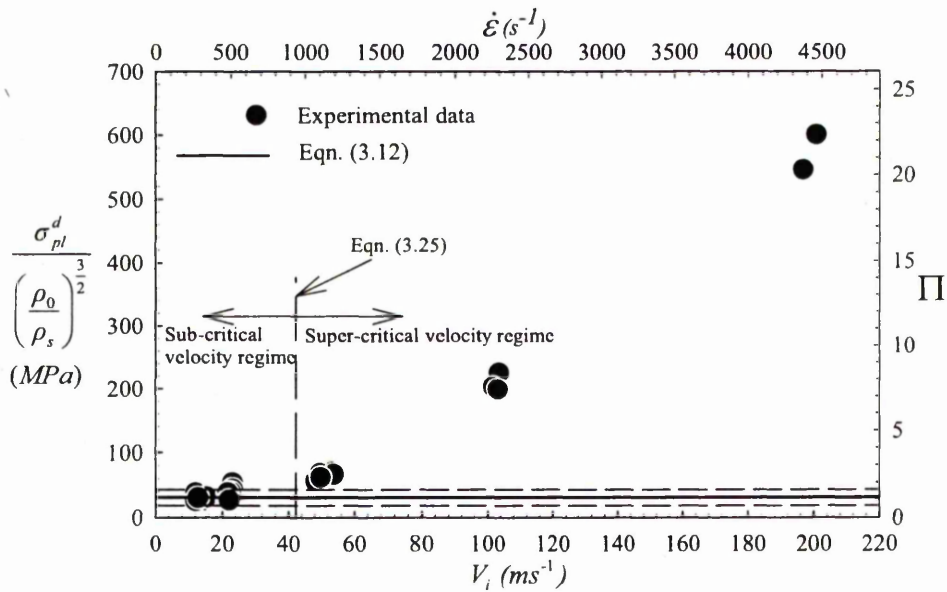
Figure 3.14 – Variation of the normalised plateau stress $\sigma_{pl}^d / (\rho_o/\rho_s)^{1.5}$ with impact velocity V_i for (a) *small* cell and (b) *large* cell y-axis Cymat specimens. The dashed lines indicate corresponding quasi-static scatter in loads and $\dot{\varepsilon}$ is the nominal engineering strain rate.
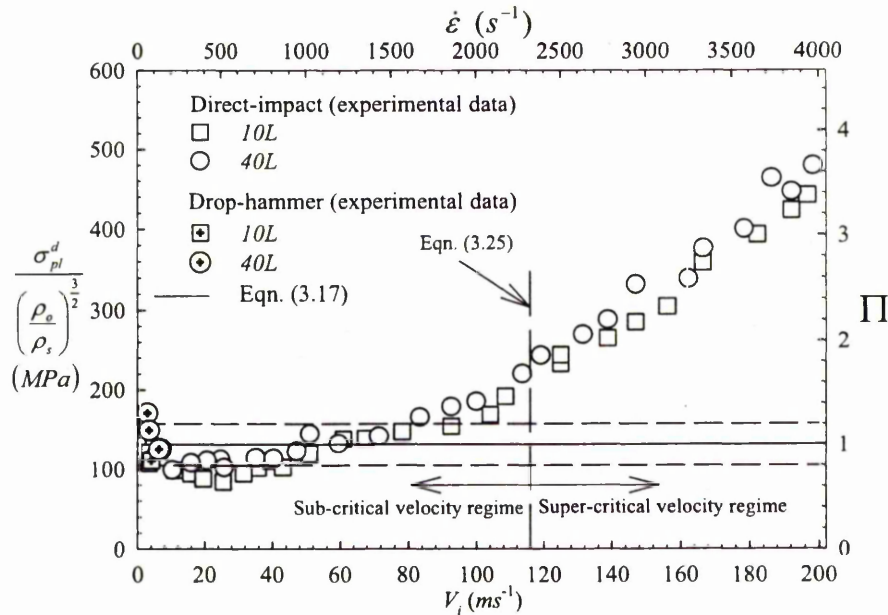
(a)
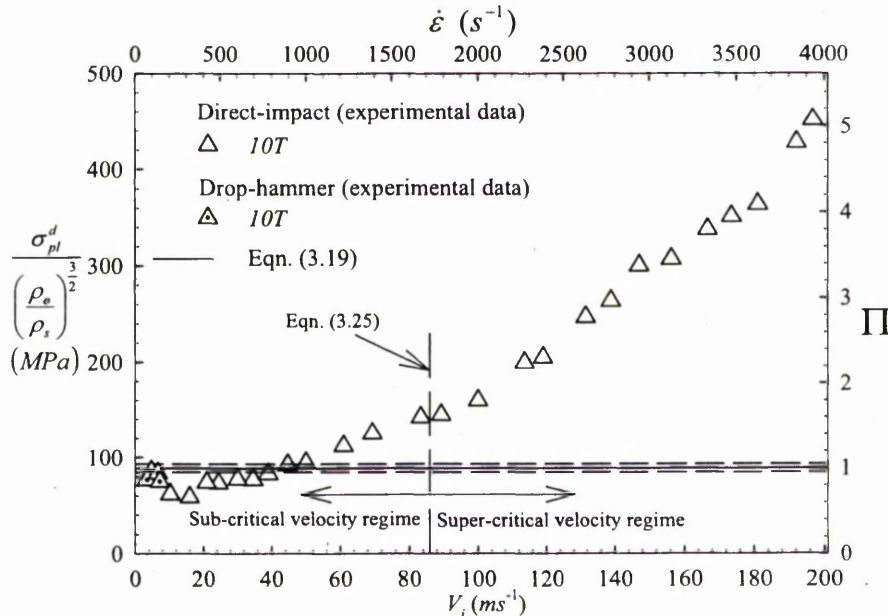
(b)

Figure 3.15 – Variation of the normalised plateau stress $\sigma_{pl}^d / (\rho_o/\rho_s)^{1.5}$ of Duocel specimens with impact velocity V_i along the (a) largest and (b) smallest dimension of their constituent cells. The dashed lines indicate corresponding quasi-static scatter in loads and $\dot{\varepsilon}$ is the nominal engineering strain rate.
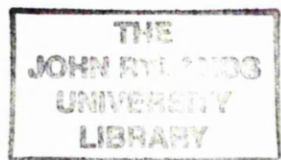
At sub-critical velocities, i.e. approximately $V_i < 108ms^{-1}$, the normalised plastic collapse and plateau stresses of *small* cell Cymat specimens are greater than their corresponding *large* cell ones (compare Figs 3.12 and 3.14). This suggests that specimen cell-size effects and strength degradation due to morphological imperfections remain active during sub-critical velocity compression. At super-critical velocities of $V_i > 108ms^{-1}$, the strength data are no longer affected by these, the strength for the *large* cell specimens being greater than the *small* cell specimens at each velocity. This implies, in particular, that further local enhancements in strength are now dominated by a different inertial phenomenon associated with the dynamic localisation of crushing, i.e. the deformation response begins to exhibit 'shock-like' characteristics (Reid and Peng, 1997).
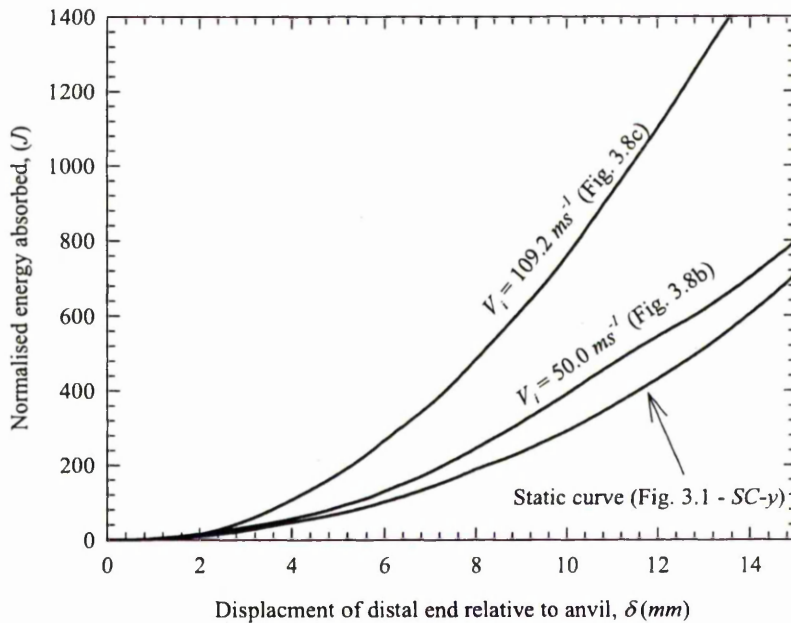
Figure 3.16 – Static and dynamic normalised energy versus displacement curves for the Cymat foam specimens.

If the time axis of the force pulses in Figs. 3.8b-c is converted into displacement of the distal end to produce nominal stress-strain curves (assuming a uniform rate of compression so that $\delta = V_i \cdot t$), the greater amount of energy (normalised by

69

$\left(\rho_o / \rho_s\right)^{3/2}$) absorbed at higher impact velocities with similar displacements is clearly evident in the normalised energy versus displacement plots in Fig. 3.16. The same is also true for the Duocel foams. The theoretical explanation for this is given in the next chapter.

3.3.2 Dynamic response of foams with a density gradient

Since the z-axis Cymat specimens have spatial variations (step-distributions) of density, tests were carried out to measure the impact forces generated by impact on either the high (HD) or the low (LD) density end of each specimen. Figure 3.17 shows two partially crushed *small* cell specimens (compressed at a velocity of approximately $23 ms^{-1}$) and their corresponding normalised stress pulses. The specimen with a higher mass ratio is compressed further by virtue of its higher kinetic energy. An unusually high level for the plastic collapse stress was recorded if the HD end of the specimen impacts the output bar (Fig. 3.17a). This was seen in both the *small* and *large* cell specimens over the entire range of velocity. It suggests that cell deformation may have occurred in the HD zone of the specimen where a higher load is needed to overcome the inertia of the thicker cell walls. Its photograph shows limited cell crushing, see Fig. 3.17a, in the HD zone. If impact occurs at the LD end of the specimen, the HD zone behaves like a rigid material so that cell crushing is confined, at least during the early period of Phase II, to the LD zone (Fig. 3.17b). Figure 3.17 shows that Phase II deformation is dominated by the multiplication of bands of crushed cells in the LD zone, regardless of which end of the specimen strikes the transmitter bar (see photographs in Fig. 3.17). This is also reflected in their plateau strength, which agrees with one another within the limits of experimental error. In general, the dynamic strength properties, the initiation, development and distribution of cell deformation and the densification strain of a specimen are all affected by spatial variations of density. Their implications must be considered when, for example, a foam panel is used for impact energy absorption purposes.
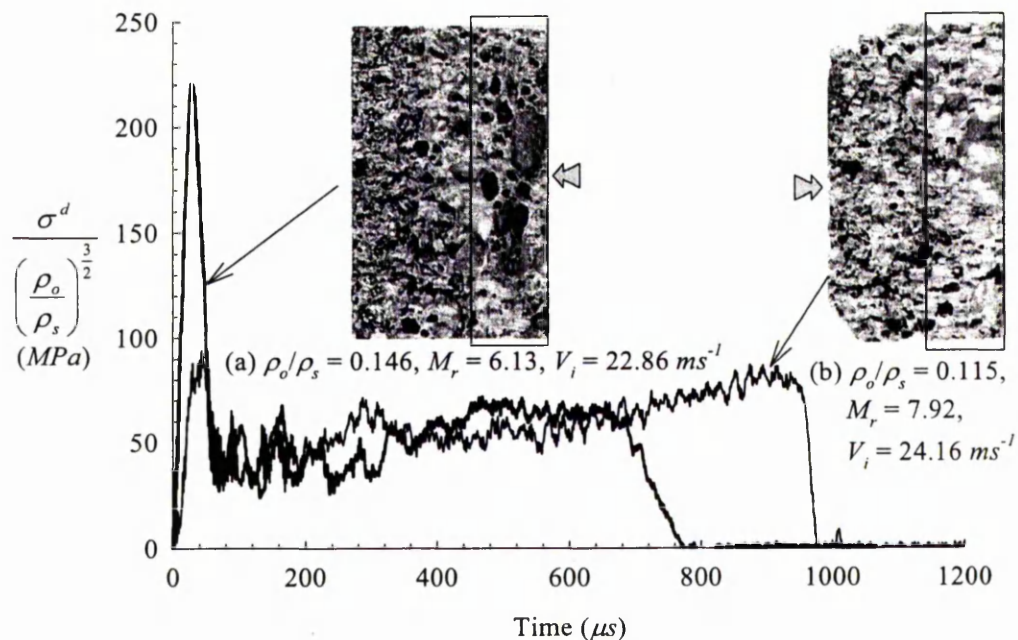
Figure 3.17 – Two *small* cell, *z*-axis specimens and their corresponding normalised stress pulses measured from the (a) HD and the (b) LD end of each specimen. The arrowhead indicates the impact end and the HD zone of each specimen are boxed.

3.3.3 Effects of specimen gauge length

To investigate the effects of specimen gauge length, tests (quasi-static and dynamic) were carried out using only *small* cell, *y*-axis Cymat specimens, of $45mm$ diameter, with gauge lengths ranging from $5mm \leq l_o \leq 65mm$. Hence, they were not affected by the size effect described in Section 3.2.2. The smallest gauge length used was $5mm$ because of difficulties with machining shorter specimens. Test specimens of different gauge length were first compressed at a constant velocity (the largest backing mass that will not cause the pressure bar to yield was used). This was then repeated for different impact velocities (up to $100ms^{-1}$) to build up a family of curves. The objective was to separate the rate sensitive response due to an increase in the impact velocity (V_i) from the length effects caused by changes in the gauge

length (l_o) of the specimen. Note that the latter is another type of 'size' effect different from the one discussed in Section 3.2.2.

Data for the normalised plateau stress ($\sigma_{pl}/[\sigma_{ys}(\rho_o/\rho_s)^{1.5}]$) of specimens with different gauge length are plotted in Fig. 3.18. The solid lines are predictions of a one-dimensional 'steady-shock' model by Reid and Peng (1997):

$$\sigma_{pl}^d = \sigma_{pl}^{qs} + \overline{\rho}V_i^2/\varepsilon_D \qquad (3.26)$$

where $\overline{\rho}$ is the average density of the specimens tested at each velocity. The dashed lines are curves of constant nominal, engineering strain rate. The resulting diagram allows some important features of specimen length scale to be illustrated. First, the shorter specimens have a stronger and stiffer response under quasi-static compression. Mukai et al. (1999a,b) also reported a similar observation with closed cell Alporas foams. This length effect persists to a value of approximately 5 average cell diameter, beyond which fluctuations in the strength property are within ±20% of its mean value predicted by Eqn. (3.10). This unusual response is probably due to end-effects in the shorter specimens where geometric softening in the two end rows of cells is made more difficult, or suppressed entirely, through its contact with the rigid platen. The data presented agree with the surface deformation analysis by Bastawros et al. (2000) who also reported that the localised bands in Alporas foam exhibit a 'long-range' correlation of approximately 3-5 cells. Second, a similar length effect is also detected in specimens under dynamic loading. Their plastic collapse stresses decrease with increasing gauge length, but at increasingly higher stresses as the impact velocity was increased. The number of cells to which this length effect persists reduces from ~5 at $10ms^{-1}$ to ~2 cells at $80ms^{-1}$. However the effects of specimen gauge length became less significant, compared to the velocity sensitive response of the foams, at increasingly higher velocities. Figure 3.18 shows that there is a characteristic length associated with an accommodation domain which sets a limit to the minimum material volume required for a valid continuum approximation.
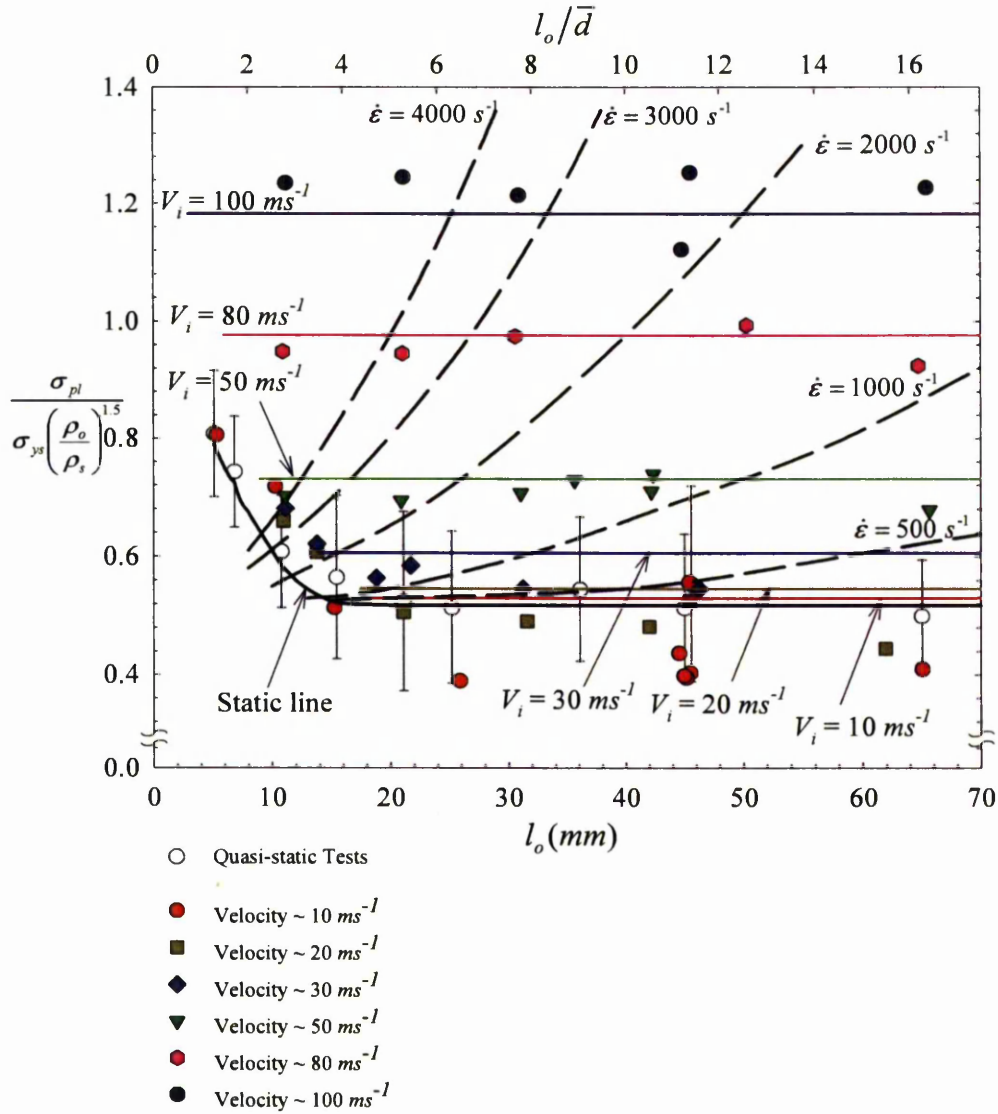
Figure 3.18 – Normalised plateau stresses of *small* cell, *y*-axis Cymat specimens with different gauge length and impact velocity. Solids lines are predictions by Eqn. 3.26 (dynamic test) and Eqn. 3.10 (quasi-static test). Dashed lines are family of constant nominal engineering strain rates.

The minimum specimen gauge length required to achieve the bulk strength of Cymat/Hydro foams is, at least, 5 average cell diameters. Lastly, the figure shows that *there is no correlation between the dynamic strength properties and the nominal engineering strain rate*. It is anticipated that the open-cell Duocel foams also exhibit similar specimen gauge length effects. The velocity dependence of the strength properties and the irrelevance of nominal engineering strain rate are clearly illustrated in Fig. 3.18. This is the one of the main reasons for the conflicting conclusions on the correlation between loading rate and dynamic strength of foams to be found in the literature.

3.4 Conclusion

The strength properties of Cymat and Duocel foams were measured and their response to dynamic loadings described. A consistent framework has been proposed to extract key material parameters (the plastic collapse and the plateau stress, and the strain at which densification occurs) from nominal stress-strain curves and dynamic force pulses. Phase II deformation is always accompanied by a load drop for both foams but this feature is notably missing in the *10T* specimens under quasi-static loading conditions.

The density gradient in z-axis Cymat specimens is responsible for the unusually high plastic collapse load measured under impact loading conditions.

It was estimated by Eqn. (3.25) that the transition to a 'shock-type' deformation response occurs at an impact velocity of approximately $108ms^{-1}$ and $42ms^{-1}$ for the *small* and *large* cell Cymat foams, respectively; and of approximately $116ms^{-1}$ and $85ms^{-1}$ along the largest (*10L & 40L*) and smallest (*10T*) principal cell dimension of the Duocel foams. Both sets of predictions compare well with the experimental data. Inertia effects associated with the dynamic localisation of crushing, i.e. 'shock' propagation, are responsible for the enhancement of the dynamic strength properties measured at super-critical impact velocities where specimen size effects (in the Cymat foams) and cell morphological defects are insignificant. In the sub-critical

velocity régime, both the specimen cell-size effects (in the Cymat foams) and cell morphological defects affect the dynamic strength properties measured. Micro-inertial effects are responsible for the enhancement of the dynamic plastic collapse stress at the sub-critical velocities. Post-impact examination of partially crushed specimens showed that deformation is through the cumulative multiplication of discrete crush bands for static loading and for dynamic loading at sub-critical impact velocities. At super-critical impact velocities, specimens deform by progressive cell crushing from the impact surface.

Chapter 4

One-dimensional 'steady-shock' models and comparison with experimental data and numerical models

4.1 Introduction

The results of an extensive experimental investigation into the dynamic uniaxial compressive response of Cymat and Duocel foams to impact loadings were presented in the previous chapter. The typical deformation pattern observed in both specimens under sub-critical velocity compression is the accumulation of discrete, non-contiguous bands of crushed cells. However, beyond a critical impact velocity of approximately $108ms^{-1}$ (*small* cell Cymat), $42ms^{-1}$ (*large* cell Cymat), $116ms^{-1}$ (along largest principal cell dimension of Duocel) and $85ms^{-1}$ (along smallest principal cell dimension of Duocel), cell crushing occurs sequentially, in a planar manner, along the axis of each specimen from the impact end towards the distal end, and the crushing wave front exhibits 'shock-type' characteristics, i.e. the particle velocity and the deformation gradient (strain) suffer finite jumps across the crush front. In this chapter, one-dimensional (1D) 'steady-shock' models are formulated and its predictions used to explain some of features of the formation and the propagation of 'steady-shock' or compaction/consolidation waves in aluminium alloy foam specimens subjected to super-critical velocity compression. The mathematical techniques used are not original, being familiar to fluid mechanicists and shock physicists, but their application to metal foams provides some new insights.

Structural 'shock' waves are known to provide a useful model for the high velocity progressive crushing behaviour of cellular structures such as those

composed of rings/tubes and man-made honeycombs (Reid et al, 1983, 1993; Reid and Bell, 1984; Reddy et al., 1991). Similarly, a 'shock' model based on a rigid, perfectly-plastic, locking (r-p-p-l) idealisation of the quasi-static stress-strain curves of cellular materials may also be used to account, via a continuum approximation, for the dominant inertial effects operating at the scale of their cell structure. These studies have been summarised in several publications by Harrigan et al. (1998a, b; 1999; 2005). Use of this simplified constitutive equation has focused on those dynamic effects that are generally produced in a material/structure with Type-I structural characteristics (Calladine and English, 1984), i.e. arising from 'shock' wave generation generally attributed to constitutive laws with a concave upwards plastic stress-strain loading path (Reid et al., 1993). In testing various materials and structures, there is also evidence, to a greater or lesser extent, that there are some Type-II structural characteristics (Harrigan et al., 1998a, 1999; 2005). This is associated with the *initiation* of deformation in an impact (non-zero initial velocity) process and is evident in Figs. 3.12 and 3.13 where the plastic collapse stress varies linearly (approximately) with the impact velocity; particularly at the lower velocities. In all of these previous studies, the formulation of the kinematics and kinetics of the problem were based only on jump conditions associated with the conservation of mass and momentum across the 'shock' front. In the present thesis, a detailed analysis is presented incorporating energy arguments as well. These draw attention to certain issues that are usually treated somewhat superficially, if not ambiguously, in previous work on cellular materials, specifically with regard to the energy absorbed at the 'shock' front.

The method of characteristics is first used to analyse the propagation of plane irrotational compressive-stress waves in a 1D foam 'rod' having a general stress-strain relation with linear elastic and concave-upwards plastic loading path (Hanssen, 2000; Hanssen et al., 2002) in Section 4.2. The emphasis is on explaining the possible occurrence and the conditions leading to the formation of shock waves. In Section 4.3 the basic jump conditions for the dependent variables across a 'shock' front are derived. To obtain closed-form solution, an r-p-p-l idealisation of the stress-strain curve for the 1D foam rod is then adopted and the equation of motion for a

plane surface of strong stress discontinuity (or 'shock' wave) propagating in the rod is formulated. Two different impact scenarios are considered: in the first, a foam rod strikes a rigid stationary target and, in the other, a rigid mass strikes a stationary foam rod supported by a rigid surface. Both impact scenarios corresponds to the two possible test configurations for the direct-impact testing technique described in Chapter 2 and relate to the two principal modes of the application of metal foams to impact energy absorption. The kinematic existence condition for continuing/propagating 'shock' compaction in the aluminium foams is also established. Comparisons are then made between the results of the 'shock' model, the experimental data and the results of finite element simulations of two-dimensional (2D) Voronoi honeycombs. Finally, the limitations of the 'steady-shock' model generally are discussed.

4.2 Assumptions and Basic equations

Consider a circular cylindrical foam 'rod' of unit cross sectional area with generators in the X-direction bounded by the surfaces of particles which in their undeformed position lie in the planes $X = 0$ and $X = l_o$ (see Fig. 4.1). The rod is
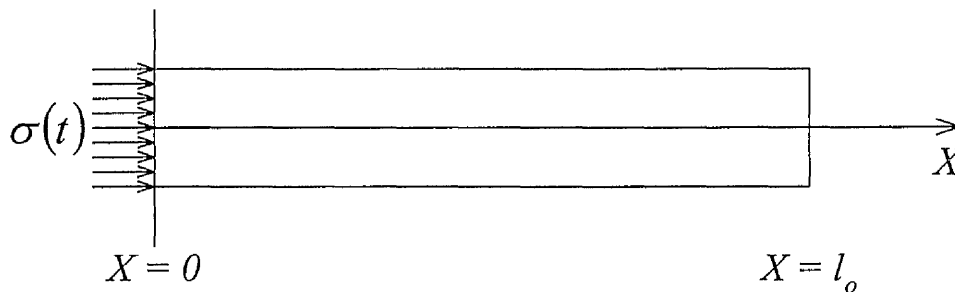
Figure 4.1 – Co-ordinate system.

assumed to be initially uniform and homogeneous in all those properties associated with the principal y-direction of a typical Cymat foam panel or any Duocel foam specimens. In common with other studies on 'steady-shock' propagation in cellular

solids (see Reid and Peng, 1997 and Ashby et al., 2000), the usual notion of a continuum is assumed to hold throughout. Suppose a system of compressive stress waves is generated by normal forces applied to the plane boundary ($X = 0$) at $t = 0$ as depicted in Fig. 4.1. The governing equations are expressed in terms of Lagrangian co-ordinates and engineering stress and strain definitions are adopted. The independent variables are X and t; and the dependent variables are axial displacement u, velocity v, uniaxial compressive strain ε and nominal compressive stress σ, all functions of X and t. Here, and in the rest of the thesis, all stresses and strains are treated as positive in compression.

The single material co-ordinate $X \in [0, l_o]$ describes the 1D foam rod so that the position of a typical particle is given by

$$x = x(X, t) \qquad \text{for } t > 0 \qquad (4.1)$$

where x is the position of the particle at time t which was at position X in the undeformed configuration. The consistency condition of $x = X$ at $t = 0$ is assumed to hold. Displacement of a particle is given by

$$u(X, t) = x(X, t) - X \qquad (4.2)$$

and the compressive engineering strain and particle velocity is defined as

$$\varepsilon = -u,_X \quad \text{and} \qquad (4.3)$$

$$v = x,_t = u,_t \qquad (4.4)$$

where the subscripts $,X$ and $,t$ indicate partial differentiation with respect to X and t whilst holding t and X fixed, respectively. To ensure that v and ε are derivable from u, they need to satisfy the kinematic compatibility relation given by

$$\varepsilon_{,t} + v_{,X} = 0 .$$ (4.5)

In order that mass be conserved locally, the density at the material point originally residing at X must be related to the initial density of the body so that

$$\rho(1 - \varepsilon) = \rho_o .$$ (4.6)

The balance of linear momentum between any two material points in the sub-interval $[a, b]$, satisfying $0 \le a < b \le l_o$ at all times, gives

$$\frac{d}{dt} \int_a^b \rho_o v \, dX = \int_a^b f \, dX - \sigma(X, t)\Big|_{X=a}^{X=b}$$ (4.7)

where ρ and ρ_o are the current and initial densities, respectively and f is the body force per unit volume. If $v_{,t}$ and $\sigma_{,X}$ exist and a and b were arbitrary, the local form of Eqn. (4.7) can be written as (see *Case 1* in Appendix B)

$$\rho_o v_{,t} = f - \sigma_{,X} .$$ (4.8)

As discussed in Chapter 3, there are three possible contributions to the 'rate-sensitive' material response of metal foams, viz. compression of the trapped gas (this applies only to the closed-cell Cymat foams); strain rate sensitivity of the material of the cell wall which is dependent on thermal activation or dislocation drag processes; and, inertial sensitivity due to the inertia of the individual cell walls. It was previously established that contributions from the compression of trapped gas are negligibly small. Likewise, the aluminium cell wall material was also shown to be strain-rate insensitive. Hence, a time-independent, constitutive equation of the form

$$\sigma = g(\varepsilon)$$ (4.9)

suffices in describing the uniaxial compressive stress state in the foam rod. For consistency with the strain-hardening model for aluminium foams developed by Hanssen et al. (2002) for uniaxial and hydrostatic loading conditions, the function g is assumed to possess the following properties:

(i) $\dfrac{dg}{d\varepsilon} > 0$ for every ε in $(\varepsilon_{cr},1)$, and $\hspace{4cm}$ (4.10)

(ii) $\dfrac{d^2 g}{d\varepsilon^2} > 0$ over the same interval. $\hspace{4cm}$ (4.11)

Hence, the function g is strictly monotonic increasing in $[\varepsilon_{cr},1]$ and concave upwards as depicted in Fig. 4.2.
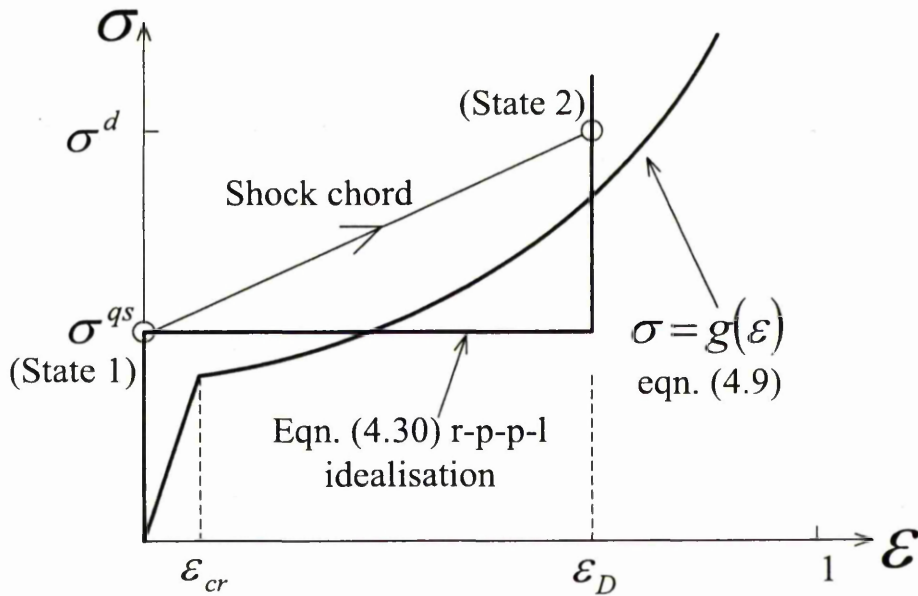
Figure 4.2 – Nominal stress-strain curve and its idealisation.

Combining Eqns. (4.8) and (4.9), and ignoring body forces, gives

$$v_{,t} = -c^2(\varepsilon)\,\varepsilon_{,x} \hspace{4cm} (4.12)$$

where $c^2(\varepsilon) = (d\sigma/d\varepsilon)/\rho_o$. Equation (4.12) has positive and negative characteristics given by

$$dX/dt = \pm c(\varepsilon).$$

<div align="right">(4.13)</div>

The invariant along $dX/dt = +c(\varepsilon)$ (a positive $C+$ characteristic) and $dX/dt = -c(\varepsilon)$ (a negative $C-$ characteristic) are constants and given, respectively, by

$$R_1 = u_{,t} + \int_0^\varepsilon c(\varepsilon)d\varepsilon = v + \int_0^\varepsilon c(\varepsilon)d\varepsilon$$

<div align="right">(4.14)</div>

and

$$R_2 = u_{,t} - \int_0^\varepsilon c(\varepsilon)d\varepsilon = v - \int_0^\varepsilon c(\varepsilon)d\varepsilon$$

<div align="right">(4.15)</div>

where R_1 and R_2 are also known as the Riemann invariants. Each of the $C-$ characteristic passes through a section of the (X,t) plane, corresponding to a uniform region in which the flow variables v and ε are constant. Therefore, the invariant $R_2 = R$ is identical for all negative characteristics. Hence, each positive characteristics is intersected at every point by some negative characteristics,

$$\left. \begin{array}{l} v + \int_0^\varepsilon c(\varepsilon)d\varepsilon = R_1 \\ v - \int_0^\varepsilon c(\varepsilon)d\varepsilon = R \end{array} \right\}.$$

<div align="right">(4.16)</div>

By addition and subtraction of Eqn. (4.16), it follows that

$$v = u_{,t} = \int_0^\varepsilon c(\varepsilon)d\varepsilon.$$

<div align="right">(4.17)</div>

Because the wave velocity is an increasing function of strain, i.e. $dc/d\varepsilon > 0$, this

means that stress increment ($\Delta\sigma > 0$) from a plastic stress level $\sigma(0, t_1)$ will eventually be overtaken by a second stress increment from a higher stress level $\sigma(0, t_1 + \Delta t_1)$ at the point (Morland, 1959; Hopkins, 1968)

$$X = c_1^2 / (dc_1/dt_1), \qquad t = t_1 + c_1 / (dc_1/dt_1) \tag{4.18}$$

in the X-t plane where $c_1 = c(\varepsilon_1)$. This is shown in Fig. 4.3.
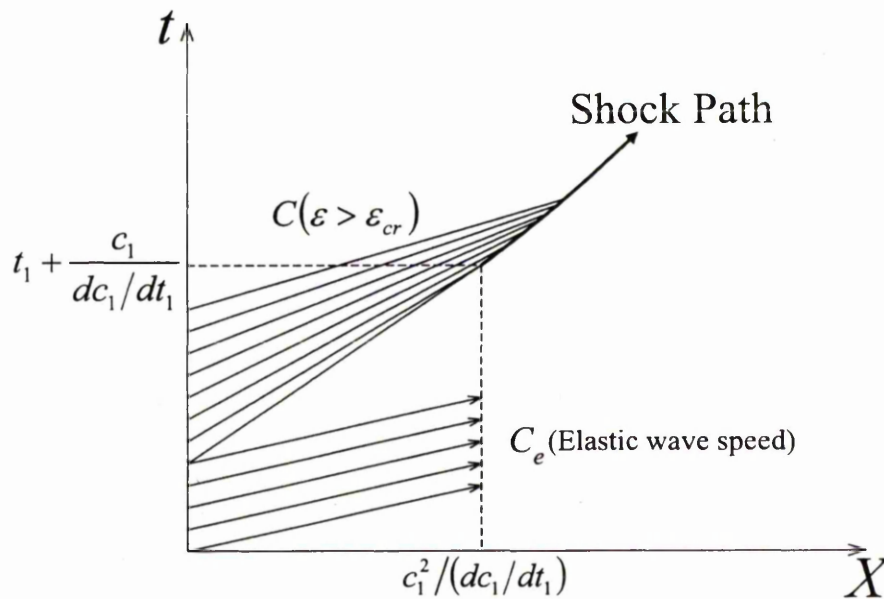
Figure 4.3 – Characteristic diagram of a simple wave system generated by a smooth and continuous force pulse.

Thereafter, the continuous wave solution breaks down and the analysis must proceed with the propagation of a discontinuity. Note that important issues such as the reflection of stress waves from the free or fixed end of the finite rod, which involves complicated interactions between the loading and unloading, elastic and plastic waves (see, for example, Morland, 1959), have not been addressed here. Finally, it should be noted that if an instantaneous velocity V_i is imposed on the plane boundary ($X = 0$) at $t = 0$, instead of the normal forces prescribed above, the $C+$

characteristics from the plane boundary ($X = 0$) is expected to intersect immediately with those of the foam rod, leading to the immediate formation of a 'shock' moving with a velocity V_s ($<V_i$).

4.3 One-dimensional (1D) 'steady-shock' models

It is assumed that the particle velocity in a foam rod is a function of the stress state only and a steady compaction (or crush) front can develop and propagate unchanged in its form. This allows the sequential cell crushing process observed during super-critical velocity compression to be analysed in terms of the Rankine-Hugoniot theory of shock propagation. The issue of whether a 'steady-shock' wave can develop in the presence of dispersive effects and the tendency of a propagating wave to evolve towards a shock is to be discussed later. The propagation of a plane surface of strong stress discontinuity in a 1D foam rod is now considered. First, the basic jump conditions, or the dynamical conditions of compatibility, across a 'shock' front are stated.

4.3.1 Basic jump conditions and 'shock' interactions

Let the 'surface' of strong stress discontinuity (or a 'shock' front) be currently at the material point $X_s = X_s(t)$ and moving at a Lagrangian wave speed of

$$V_s = dX_s/dt .$$
(4.19)

For a first-order singular surface, the motion of the surface is continuous whilst the deformation gradient and the particle velocity may suffer finite discontinuity. Displacement continuity across the 'shock' front is expressed, by Hadamard's Lemma (Eqn. C1 in Appendix C), as

$$d[u]/dt = [u_{,t}] + V_s[u_{,X}] = [v] - V_s[\varepsilon] = 0 .$$
(4.20)

The symbol $[h] \equiv h^- - h^+$ denotes a jump in the dependent variable, say h, across the 'shock' front where superscripts $-$ and $+$ denote the region immediately behind and just ahead of the 'shock', respectively. If $u_{,t}$ is continuous everywhere except at X_s, Eqn. (4.7) becomes (*Case 2* in Appendix B)

$$[\sigma] - \rho_o V_s [v] = 0 . \qquad (4.21)$$

For a thermodynamic system, the first law asserts that (Ericksen, 1991; Eringen and Şuhubi, 1974)

$$\frac{d}{dt}(E_k + E_U) = (H - Q) + \mathrm{P}_{ext} \Leftrightarrow$$

$$\frac{d}{dt}\left(\int_a^b \rho_o \left(\frac{1}{2} v^2 + U \right) dX \right) = \left(\int_a^b \rho_o r \, dX + q \, \Big|_{X=a}^{X=b} \right) + \left(\int_a^b f v \, dX - \sigma v \, \Big|_{X=a}^{X=b} \right)$$

$$(4.22)$$

where $d(E_k + E_U)/dt$ is the rate of increase of kinetic plus internal energies (per unit reference area), respectively; U is internal energy per unit mass; q is the X-component of the heat flux vector; and r is the heat source per unit mass of specimen. If $u_{,t}$ and $U_{,t}$ are continuous everywhere except at X_s, assuming no heat is generated within the specimen so that $\int_a^b \rho \, r \, dX = 0$ and ignoring body force, Eqn. (4.22) becomes (Bland, 1988)

$$\rho_o V_s [v^2/2 + U] - [\sigma v + q] = 0 . \qquad (4.23)$$

The jump conditions in Eqns. (4.20), (4.21) and (4.23) express the fact that the flux of mass, momentum and energy, respectively, must remain continuous across the 'shock' front, whilst the stress, density and internal energy need not be. Likewise, the Clausius-Duhem inequality, applicable to cases where entropy is well-defined, is given by (Ericksen, 1991)

$$\frac{d}{dt} \int_a^b \rho_o \eta \, dX \geq \int_a^b \frac{r}{\theta} dX + \frac{q}{\theta}\bigg|_a^b \qquad (4.24)$$

and it can be expressed in a jump form (*Case 2* in Appendix B) as follows (Ericksen, 1991)

$$\rho_o V_s [\eta] \geq [q/\theta], \qquad (4.25)$$

where η is the specific entropy (or entropy per unit mass) and θ the absolute temperature.

Across the 'shock' front, the jump in the compressive stress is found by eliminating V_s between Eqns. (4.20) and (4.21) to be

$$[\sigma] = -\rho_o [u,_t]^2 / [u,_X] = \rho_o [v]^2 / [\varepsilon], \qquad (4.26)$$

and the 'shock' wave speed is found by eliminating $[v]$ to be

$$V_s = \sqrt{[\sigma] / \rho_o [\varepsilon]}. \qquad (4.27)$$

If $V_s \geq c_e$ (the elastic wave speed in a foam 'rod' is estimated in Section 2.3 of Chapter 2), a plastic 'shock' wave propagates into a region of material which is initially undeformed; otherwise, an elastic wave precedes the plastic 'shock' wave. Only the latter situation is considered here although $c_e \to \infty$ for a *r-p-p-l* material.

Suppose first that two uniform states of deformation and flow ('b' and 'c' in Fig. 4.4a) are separated by a shock front, travelling at a uniform velocity V_s, across which all dependent variables undergo discontinuous changes. All regions of deformation are supposed uniform and separated by uniformly moving wave fronts. Treating each stress-wave profile as a series of small continuous steps with a constant wave

velocity (see Morland, 1959), a plastic loading wavelet ('a' in Fig. 4.4a) will eventually catches up with the main 'shock' front since the plastic wavelet velocity exceeds the shock velocity. This plastic loading wavelet is generated by the compression of crushed cells beyond their densification strain ε_D (given by Eqns. 3.4 & 3.5) which, although having limited compressibility,

$$\text{(a)} \qquad\qquad\qquad\qquad \text{(b)}$$
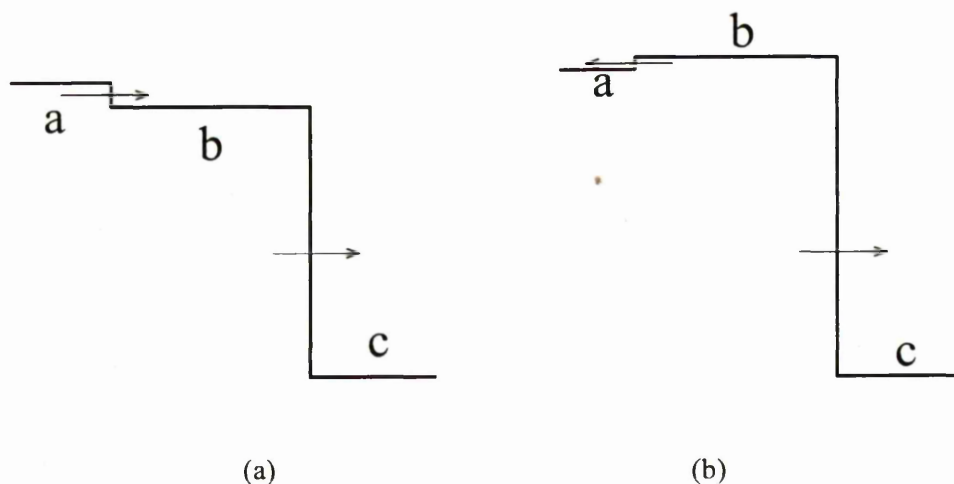
Figure 4.4: Situation before (a) and after (b) interaction between a plastic wavelet and the main 'shock' front.

still occurs behind the 'shock' front. It will now be shown that the interaction between this plastic loading wavelet and the main 'shock' front generates a weak reflected (elastic) shock wave travelling in an opposite direction to the main 'shock' front as shown in Fig. 4.4b. The increase in particle velocity across a 'shock' separating any two states, viz. '−' and '+', is given by Eqns. (4.6) and (4.26) to be

$$[v]_{-\to+} = \sqrt{\left(\sigma^- - \sigma^+\right)\left(1/\rho^+ - 1/\rho^-\right)}. \qquad (4.28)$$

Interaction between the plastic loading wavelet, moving from states 'a' to 'b', and the main 'shock' front, moving from states 'b' to 'c', is *not equivalent* to a single 'shock' transition from 'a' to 'c', as is evident from a mismatch in their particle velocity where (see Fig. 4.4)

$$[v]_{a \to c} < [v]_{b \to c} + [v]_{a \to b} . \tag{4.29}$$

The correct matching of particle velocity is only achieved by introducing an elastic *unloading* wave, moving from states 'b' to 'a' after interaction. This *unloading* wave is then reversed by the next oncoming plastic wavelet, and the entire interaction cycle is repeated (Morland, 1959). In simple qualitative terms, this means that the 'shock' wave gradually built-up from behind and with increasing strength its velocity increases. To circumvent the need to consider complicated 'shock' interactions, such as the one just described above, an *r-p-p-l* idealisation of the stress-strain curve for the foam rod will be proposed in Eqn. (4.30).

4.3.2 Impact of a foam rod against a rigid, stationary target

4.3.2.1 Equation of motion

Consider a foam rod of unit area travelling at a speed of V_i ($< c_e$) until it strikes squarely a stationary rigid wall at time $t = 0$ as depicted in Fig. 4.5. The frame of reference is fixed at the proximal (impact) end of the rod at $t = 0$. Let a 'steady-shock' form immediately at the plane boundary $X = 0$ on impact. At $t > 0$ 'shock' compaction of the material occurs at the point $x(X_s, t)$, with the portion of the rod l remaining rigid.

In common with the theme of designing with foams for impact energy absorption, and to obtain simple closed-form solution to the problem, a simple rate-independent *r-p-p-l* idealisation of the stress-strain curve for the foam rod (see Section 2.4 of Chapter 2), viz.

$$g(\varepsilon) = \begin{cases} \sigma^{qs} & 0 \leq \varepsilon < \varepsilon_D \\ +\infty & \varepsilon = \varepsilon_D \end{cases}, \tag{4.30}$$

is adopted here where the superscript *qs* denotes quasi-static values. The response of

the material in the densification régime, i.e. $\varepsilon > \varepsilon_D$ (densification strain), is of lesser intrinsic interest in energy absorption applications and, therefore, a locking material assumption at ε_D suffices. Although Eqn. (4.30) is not strictly monotonic increasing in $[0, \varepsilon_D)$, its concave-upwards characteristic makes possible the existence of 'shock' waves. The locking assumption does not permit wave reflections or 'shock' interactions. Its initial rigid response also requires an instantaneous jump in stress from 0 to σ^{qs} in the rod on compression. This implies that an elastic loading wave
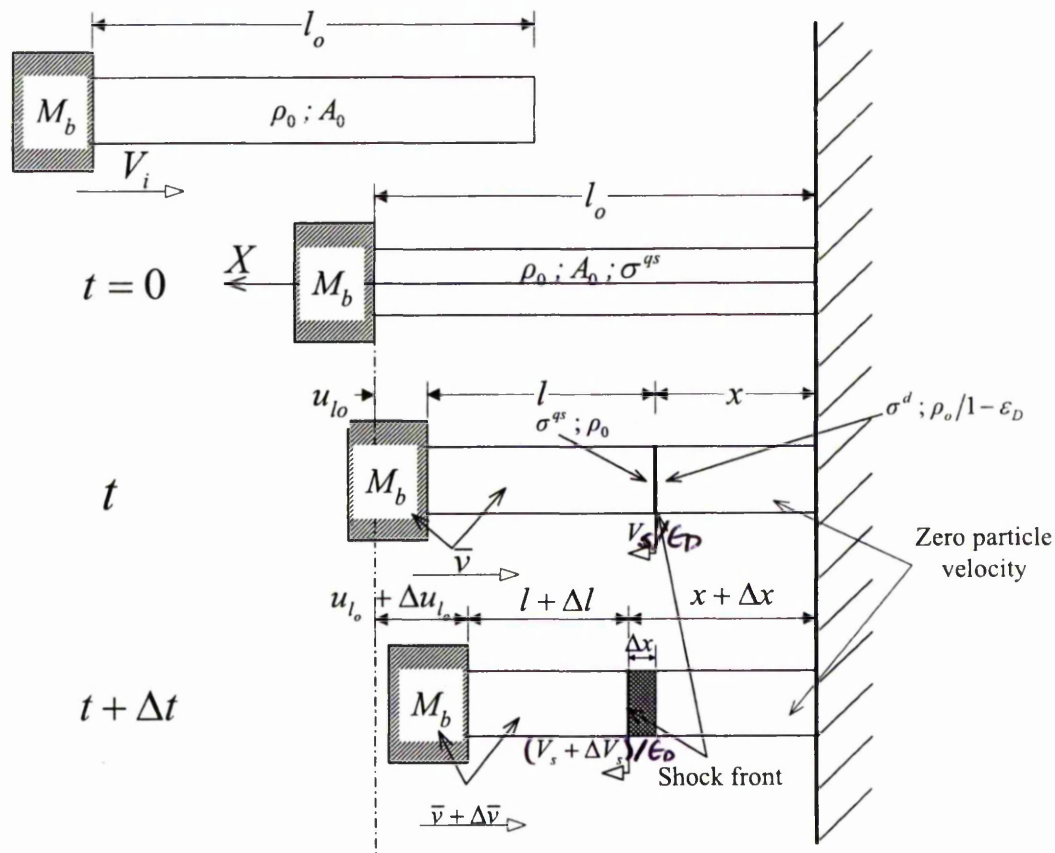
Figure 4.5 - Parameters defining the 'shock' model for the impact of a foam rod against a rigid stationary target.

travels the length of the rod at an infinite velocity which, given that the elastic wave speed C_e is at least an order of magnitude higher than the impact velocity V_i (see Section 2.3), is not physically unreasonable.

The conditions immediately behind and just ahead of the 'shock' are as follows:

Behind 'shock' front: $\quad v^- = 0$, $\varepsilon^- = \varepsilon_D$, $\sigma^- = \sigma^d$, $\rho^- = \rho_o/(1 - \varepsilon_D)$

$$(4.31)$$

Ahead of 'shock' front: $\quad v^+ = \overline{v}$, $\varepsilon^+ = 0$, $\sigma^+ = \sigma^{qs}$, $\rho^+ = \rho_o$.

$$(4.32)$$

Here, the superscript d denotes dynamic values. Substituting these conditions into Eqn. (4.26) gives the 'shock' relation

$$\sigma^d = \sigma^{qs} + \rho_o \overline{v}^2 / \varepsilon_D \,, \qquad (4.33)$$

which must be satisfied at all times. Equation (4.33) ensures mass and momentum conservation across the 'shock front. Let u_{l_o} ($\equiv |u(l_o,t)|$) be the displacement of the distal end of the foam rod at time t and from geometry

$$l = l_o - u_{l_o} - x \,, \qquad (4.34)$$

and so

$$\dot{l} = dl/dt = -\left(\dot{x} + \dot{u}_{l_o}\right) = -\dot{u}_{l_o}/\varepsilon_D = -\overline{v}/\varepsilon_D \qquad (4.35)$$

where $\varepsilon_D = u_{l_o}/\left(u_{l_o} + x\right)$. From Eqns. (4.20) and (4.21), one obtains

$$[\sigma \cdot v] = \frac{\sigma^- + \sigma^+}{2}\left(v^- - v^+\right) + \frac{\sigma^- - \sigma^+}{2}\left(v^- + v^+\right)$$

$$= \frac{\sigma^- + \sigma^+}{2}[v] + \frac{\rho_o V_s}{2}\left(v^- - v^+\right)\left(v^- + v^+\right) \qquad (4.36)$$

$$= (\sigma^- + \sigma^+)V_s[\varepsilon]/2 + \rho_o V_s[v^2]/2$$

The dynamic compaction process occurs so quickly that the foam rod can be assumed to be non-heat conducting wherein q is identically zero. Substituting Eqn. (4.36) into (4.23), and setting $[q] = 0$, gives

$$[\rho_o U] - (\sigma^- + \sigma^+)[\varepsilon]/2 = 0, \qquad (4.37)$$

the familiar Rankine-Hugoniot equation. If the straight line (or Rayleigh line) joining the states in front of, and behind, the 'shock' front, in the stress-strain plane, is defined as the 'shock' chord, then Eqn. (4.37) implies that the change in internal energy per unit reference volume is given by the area under the 'shock' chord in the closed interval $[\varepsilon^+, \varepsilon^-]$. Thus, the increase in internal energy when an element of length Δl is compacted to a length of $\Delta x = \Delta l(1 - \varepsilon_D)$ at the 'shock' front in the time interval t to $t + \Delta t$ is given by

$$\Delta E_U = E_U(t + \Delta t) - E_U(t) = \frac{1}{2}(\sigma^d + \sigma^{qs})\varepsilon_D \Delta l. \qquad (4.38)$$

Over the same time interval, the change in kinetic energy of the undeformed rod, ahead of the 'shock', as it changes velocity from $\bar{v}$ to $\bar{v} + \Delta \bar{v}$ is

$$\Delta E_k = E_k(t + \Delta t) - E_k(t) = \frac{1}{2}\left\{2\bar{v}(M_b + \rho_o l)\Delta \bar{v} + \rho_o \bar{v}^2 \Delta l\right\} + O\left(\Delta \bar{v}^2, \Delta l \Delta \bar{v}, \Delta l \Delta \bar{v}^2\right)$$

$$(4.39)$$

If the 'shock' compaction process leaves State 1 at time t and arrives at State 2 at time $t + \Delta t$, then integrating Eqn. (4.2), assuming an isolated system

wherein $\delta Q = \delta P_{ext} = 0$, gives

$$(E_k + E_U)_2 - (E_k + E_U)_1 = 0 \tag{4.40}$$

From Eqns. (4.35), (4.38) and (4.39) and ignoring all higher order quantities of small terms, dividing by Δt and taking the limit $\Delta t \to 0$, Eqn. (4.40) gives the equation of motion of the distal end of the foam rod as

$$\left\{(1 + M_r) - u_{l_o}/\varepsilon_D l_o\right\} d\bar{v}/dt = -\sigma^{qs}/\rho_o l_o \tag{4.41}$$

where the mass ratio $M_r \equiv M_b/\rho_o l_o$. An equivalent kinematic approach in which considerations are given only to the purely mechanical conditions across the 'shock' front, viz. Eqns. (4.7), (4.26), (4.27), (4.34) and (4.35), was previously used by Reid and Peng (1997) to derive Eqn. (4.41). This last equation is easily integrated with the initial condition $\bar{v}(u_{l_o} = 0) = V_i$ to give

$$\bar{v} = du_{l_o}/dt = \left\{V_i^2 + 2\sigma^{qs}\varepsilon_D \ln\left(1 - u_{l_o}/(1 + M_r)\varepsilon_D l_o\right)/\rho_o\right\}^{1/2} \tag{4.42}$$

where V_i is the initial impact velocity. Note that as $M_r \to \infty$, $\bar{v} \to V_i$ $\forall u_{l_o} \in [0, \varepsilon_D l_o]$, which implies that constant velocity compression of the rod is only achieved with a sufficiently large backing mass. A straight-forward order of magnitude argument suggests that $\bar{v} \approx V_i$ when $M_r \geq 100$. Substituting for $\bar{v}$ in Eqn. (4.33) gives the dynamic stress immediately behind the 'shock' wave front as

$$\sigma^d = \sigma^{qs}\left\{1 + 2\ln\left(1 - u_{l_o}/(1 + M_r)\varepsilon_D l_o\right)\right\} + \rho_o V_i^2/\varepsilon_D . \tag{4.43}$$

A fourth-order Runge-Kutta numerical scheme is used to solve Eqn. (4.42) for the displacement of the distal end of the foam rod with time, $u_{l_o}(t)$. Together with Eqn. (4.43) the variation of the dynamic stress σ^d with time t can be found. Since the

compacted material behind the 'shock' is rigid and at rest (a consequence of the locking material idealisation), the dynamic stress measured is also given by Eqn. (4.43). In the limit as $u_{l_o} \to 0$, $\sigma^{qs} = \sigma^{qs}_{cr}$ (the quasi-static plastic collapse stress), the 'shock-enhanced' plastic collapse stress is given by

$$\sigma^d_{cr} = \sigma^{qs}_{cr} + \rho_o V_i^2 / \varepsilon_D .$$
(4.44)

Eqn. (4.44) has also been shown to have relevance for wood (Reid and Peng, 1997) and for aluminium honeycombs (Harrigan et al. 1999) under direct-impact loading conditions.

The initial impact velocity v_{lock} required to achieve full locking of the foam rod is found by setting $\bar{v} = 0$, $V_i = v_{lock}$ and $u_{l_o} = \varepsilon_D l_o$ in Eqn. (4.42) to be

$$v_{lock} = \sqrt{2\sigma^{qs}_{pl} \varepsilon_D \ln\left(1 + 1/M_r\right)/\rho_o} .$$
(4.45)

Hence the ratio of the kinetic energy absorbed under dynamic loading conditions at an initial impact velocity of v_{lock} to that absorbed up to full locking under quasi-static conditions is given by

$$\Pi = \left(1 + M_r\right)\ln\left(1 + 1/M_r\right).$$
(4.46)

Note that Π converges to unity as $M_r \to \infty$. Equation (4.46) shows a greater benefit of the dynamic enhancement of the crushing strength in absorbing the kinetic energy of the foam projectile occurs for small values of the mass ratio M_r. $\Pi > 1$ because of the influence of inertia effects in producing higher stress levels than σ^{qs} whilst the material reaches ε_D.

4.3.2.2 Kinematic existence condition for 'shock' compaction

It is convenient to introduce the specific free energy (or the Helmholtz free energy) ψ at the common absolute temperature of $\theta^- = \theta^+ = \theta$ defined by (Ericksen, 1991)

$$\psi = U - \theta\eta \tag{4.47}$$

where U is the internal energy per unit mass and η the specific entropy. Eliminate U in Eqn. (4.23) by using (4.36) and (4.47) gives (Ericksen, 1991)

$$[\psi] - \left(\sigma^- + \sigma^+\right)[\varepsilon]/2 = \theta\left([q]/\theta - V_s[\eta]\right)/V_s . \tag{4.48}$$

Since θ and V_s are both positive constants, it follows from Eqns. (4.25) and (4.48) that

$$- [\psi] \leq \left(\sigma^- + \sigma^+\right)[\varepsilon]/2 . \tag{4.49}$$

The inequality is a neat expression of the property of the isothermal stress-strain plane illustrated in Figure 4.2. The term $\left(\sigma^- + \sigma^+\right)[\varepsilon]/2$ is the area under the 'shock' chord between 0 and ε_D, whilst $[\psi]$ is the corresponding area under the stress-strain curve which gives the energy absorbed per unit reference volume of material under quasi-static compression. *Consequently, a greater amount of energy will be expended in the adiabatic 'shock' compaction of a foam rod than in quasi-static compression.* Since $[q/\theta] = 0$, it follows from Eqn. (4.25) that

$$\eta^- \geq \eta^+ . \tag{4.50}$$

This implies that an increase in the specific entropy always accompanies the passage

94

of a 'shock'.

Let an element of length Δl be compacted to $\Delta l(1 - \varepsilon_D)$ at the 'shock' front. The jumps in the kinetic and internal energies per unit mass on a shock front advancing into a stationary, stress-free material are equal for a non-heat conducting foam rod (for which q is identically zero) in an isolated thermodynamic system (Chadwick, 1976). Therefore, Eqn. (4.40) gives

$$(E_U)_2 - (E_U)_1 = (\sigma^- + \sigma^+)\varepsilon_D \Delta l/2 = \rho_o \bar{v}^2 \Delta l/2 . \tag{4.51}$$

Writing $[\psi] = \sigma^{qs}\varepsilon_D$ and multiply Eqn. (4.49) with Δl, substitute for $(E_U)_2 - (E_U)_1$ with Eqn. (4.51), gives

$$\bar{v} \geq (2\sigma^{qs}\varepsilon_D/\rho_o)^{1/2} . \tag{4.52}$$

This is the kinematic existence condition for continuing 'steady-shock' wave propagation in the foam rod. Substituting $\sigma^{qs} = \sigma_{cr}^{qs} = C_n \sigma_{ys}(\rho_o/\rho_s)^{3/2}$ (see Section 3.2.2) into Eqn. (4.52) gives the critical velocity beyond which progressive cell crushing occurs, i.e. exhibiting 'shock'-type characteristics, viz.

$$V_{i-critical} = (2C_n\sigma_{ys}/\rho_s)^{1/2}(\rho_o/\rho_s)^{1/4}\varepsilon_D^{1/2} \tag{4.53}$$

where subscript $n = 1$ (*small* cell), 3 (*large* cell), 5 (*10L* & *40L*) or 7 (*10T*). This derivation confirms the result produced by more simplistic qualitative arguments on the role of the 'energy barriers' by Reid and Peng (1997).

The predicted critical velocity using Eqn. (4.53) is $108ms^{-1}$, $42ms^{-1}$, $116ms^{-1}$ and $85ms^{-1}$ for the *small* cell (using $\rho_o/\rho_s = 0.101$), *large* cell (using $\rho_o/\rho_s = 0.048$) cell, *10L* & *40L* (using $\rho_o/\rho_s = 0.1$) and *10T* (using $\rho_o/\rho_s = 0.096$) specimens, respectively. As discussed in Chapter 3, the predictions agree well with

their respective experimental values of approximately $100ms^{-1}$, $50ms^{-1}$, $110ms^{-1}$ and $90ms^{-1}$.

4.3.2.3 Partitioning of energy absorbed

Since strain rate sensitivity of the cell wall material and the compression of trapped gas are negligible, then the difference between the areas under the 'shock' chord and the plastic stress-strain loading path in the interval $[0, \varepsilon_D]$ gives the additional energy absorbed associated with micro-inertial effects. Therefore, the increment of work done, due to micro-inertia, in compacting an increment of thickness δx for an *r-p-p-l* foam rod is

$$\delta W = \left(\sigma^d - \sigma^{qs}\right)A_o\varepsilon_D\delta x/2. \tag{4.54}$$

Replacing σ^d with Eqn. (4.43) and setting $u_{l_o} = x\varepsilon_D/(1 - \varepsilon_D)$ in Eqn. (4.54), and integrating from $x = 0$ to $x = l_o$, gives

$$\overline{W} \equiv W/A_o l_o = \rho_o V_i^2/2 + \sigma^{qs}\varepsilon_D\left\{[(1+M_r)\varepsilon_D - M_r]\ln\left[\frac{M_r - (1+M_r)\varepsilon_D}{(1+M_r)(1-\varepsilon_D)}\right] - 1\right\}. \tag{4.55}$$

The plastic strain energy density associated with quasi-static compression of the rod is $\sigma^{qs}\varepsilon_D$; whilst Eqn. (4.55) shows that the plastic strain energy per unit total volume associated with inertial effects has a quadratic dependence with the impact velocity for a 'shock-type' compaction process. For example, Eqn. (4.55) predicts the Duocel foams in Figs. 3.9 (c) and (f) absorb 41% and 33% more energy, respectively, compared to that absorbed by the same material under quasi-static compression up to ε_D.

4.3.3 Impact of a rigid mass against a stationary foam rod

For the sake of completeness, the reverse impact scenario of a rigid mass striking a stationary foam rod is now considered. Suppose a rigid mass M_b travels at a speed of V_i, along the X-axis, until it strikes squarely a foam rod of unit area that is supported at its distal end by the pressure bar, as depicted in Fig. 4.6. The conditions just ahead and immediately behind the 'shock' front are as follows:

$$\text{Behind 'shock' front:} \quad v^- = \bar{v}, \quad \varepsilon^- = \varepsilon_D, \quad \sigma^- = \sigma^d, \quad \rho^- = \rho_o/(1-\varepsilon_D)$$

$$(4.56)$$

$$\text{Ahead of 'shock' front:} \quad v^+ = 0, \quad \varepsilon^+ = 0, \quad \sigma^+ = \sigma^{qs}, \quad \rho^+ = \rho_o.$$

$$(4.57)$$

Note that the 'shock' relation given in Eqn. (4.33) must also be satisfied across the 'shock' front. For simplicity, define the scalar variables u_{l_o}, x and l as shown in Fig. 4.6. From geometry

$$dl/dt = -\bar{v}/\varepsilon_D \tag{4.58}$$

and

$$dx/dt = (1-\varepsilon_D)\bar{v}/\varepsilon_D . \tag{4.59}$$

By Eqn. (4.37), the increase in internal energy of an element Δl in the time interval t and $t + \Delta t$ is

$$\Delta E_U = E_U(t + \Delta t) - E_U(t) = (\sigma^d + \sigma^{qs})\varepsilon_D |\Delta l|/2 \tag{4.60}$$

and the change in kinetic energy of the agglomerated (crushed) material behind the
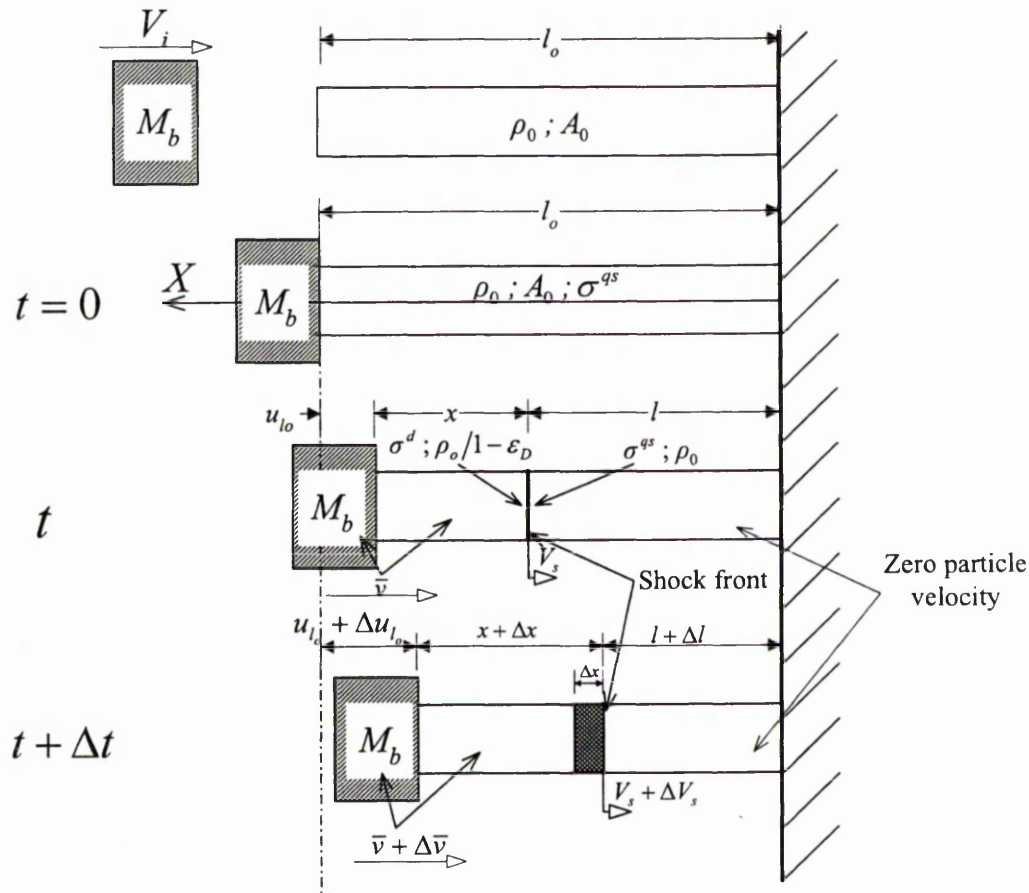
Figure 4.6: Parameters defining the 'shock' model for the impact of a rigid mass against a stationary foam rod.

'shock' front as it changes velocity from $\bar{v}$ to $\bar{v} + \Delta\bar{v}$ is

$$\Delta E_k = E_k(t + \Delta t) - E_k(t) = M_b \bar{v}\Delta\bar{v} + \frac{\rho_o x \bar{v}\Delta\bar{v}}{(1 - \varepsilon_D)} + \frac{\rho_o \bar{v}^2 \Delta x}{2(1 - \varepsilon_D)} + O(\Delta\bar{v}^2, \Delta\bar{v}\Delta x).$$

(4.61)

Using Eqns. (4.58) to (4.61) and neglecting all higher order quantities of small terms, then dividing by Δt and taking the limit $\Delta t \to 0$, Eqn. (4.40) gives

$$\left(M_r + u_{l_o}/\varepsilon_D l_o\right) d\bar{v}/dt = -\sigma_d/\rho_o l_o.$$

(4.62)

Equation (4.62) can now be integrated with the initial condition $\bar{v}\left(u_{l_o} = 0\right) = V_i$ to give the common velocity of the rigid mass and the agglomerated (compacted) material behind the 'shock' front to be

$$\bar{v} = \left\{\varepsilon_D \left(M_r^2 \left(\sigma^{qs} + \rho_o V_i^2 / \varepsilon_D\right) / \left(M_r + u_{l_o} / \varepsilon_D l_o\right)^2 - \sigma^{qs}\right) / \rho_o\right\}^{1/2}. \tag{4.63}$$

From Eqns. (4.33) and (4.63), the stress immediately behind the 'shock' front is given by

$$\sigma^d = M_r^2 \left(\sigma^{qs} + \rho_o V_i^2 / \varepsilon_D\right) / \left(M_r + u_{l_o} / \varepsilon_D l_o\right)^2. \tag{4.64}$$

The impact velocity v_{lock} required to achieve full locking of the foam rod is found by setting $\bar{v} = 0$, $V_i = V_{lock}$ and $u_{l_o} = \varepsilon_D l_o$ in Eqn. (4.63) to be

$$v_{lock} = \sqrt{\sigma^{qs} \varepsilon_D \left[\left(1 + 1/M_r\right)^2 - 1\right] / \rho_o}. \tag{4.65}$$

Hence, the ratio of the initial kinetic energy of the backing mass (which is fully absorbed by the foam rod) to that of the energy absorbed in static compression of the foam rod is given by

$$\Pi = 1 + \frac{1}{2M_r}. \tag{4.66}$$

Just like the previous case of the impact of a foam rod against a rigid target, $\Pi > 1$ for all $M_r > 0$ due to the influence of inertia effects.

4.4 Comparison with experimental data and numerical models

4.4.1. Comparison with the experimental data

Within the limits of the r-p-p-l material model, the predictions of the 'shock' theory compare well with the experimental force-time pulses which is evident in Figs. 4.7 (Cymat foams) and 4.8 (Duocel foams). Note that some of the force pulses (such as Figs. 4.7 & 4.8a,b and c) were truncated by reflected stress waves from the distal end of the output bar.

Although the 'shock' theory is not applicable in the sub-critical velocity regime, a reasonable agreement with the measured force pulses is still achieved. In general, the theory does not reliably predict the onset of densification because the actual foam material is not perfectly rigid at its densification strain ε_D. The extent to which the material behind the 'shock' front is compacted depends on the impact velocity and it is always to a higher nominal strain value than that predicted by using Eqns. (3.4) and (3.5). The increasing discrepancy between the prediction and the experimental force pulses, especially in the super-critical velocity régime such as in Figs. 4.8c & f, is a direct consequence of the locking material assumption. To support this argument, the actual densification strain value (indicated by a hollow circle in Figs. 4.8c and f) from the experimental force pulse is used, instead, in the theoretical calculations to predict the force pulses. An excellent agreement with the experiment is obtained, see Figs. 4.8c and f, which supports the argument above. A better agreement between theory and experiment can, in general, be achieved by relaxing the locking assumption at the densification strain and allowing the strain behind the 'shock' front to vary with the dynamic stress, such as in a recent study on wood by Harrigan et al. (2005).

Figure 4.9 shows a reasonably good agreement between the normalised energy absorbed by the Cymat foam rod and the predictions by the 'shock' model.
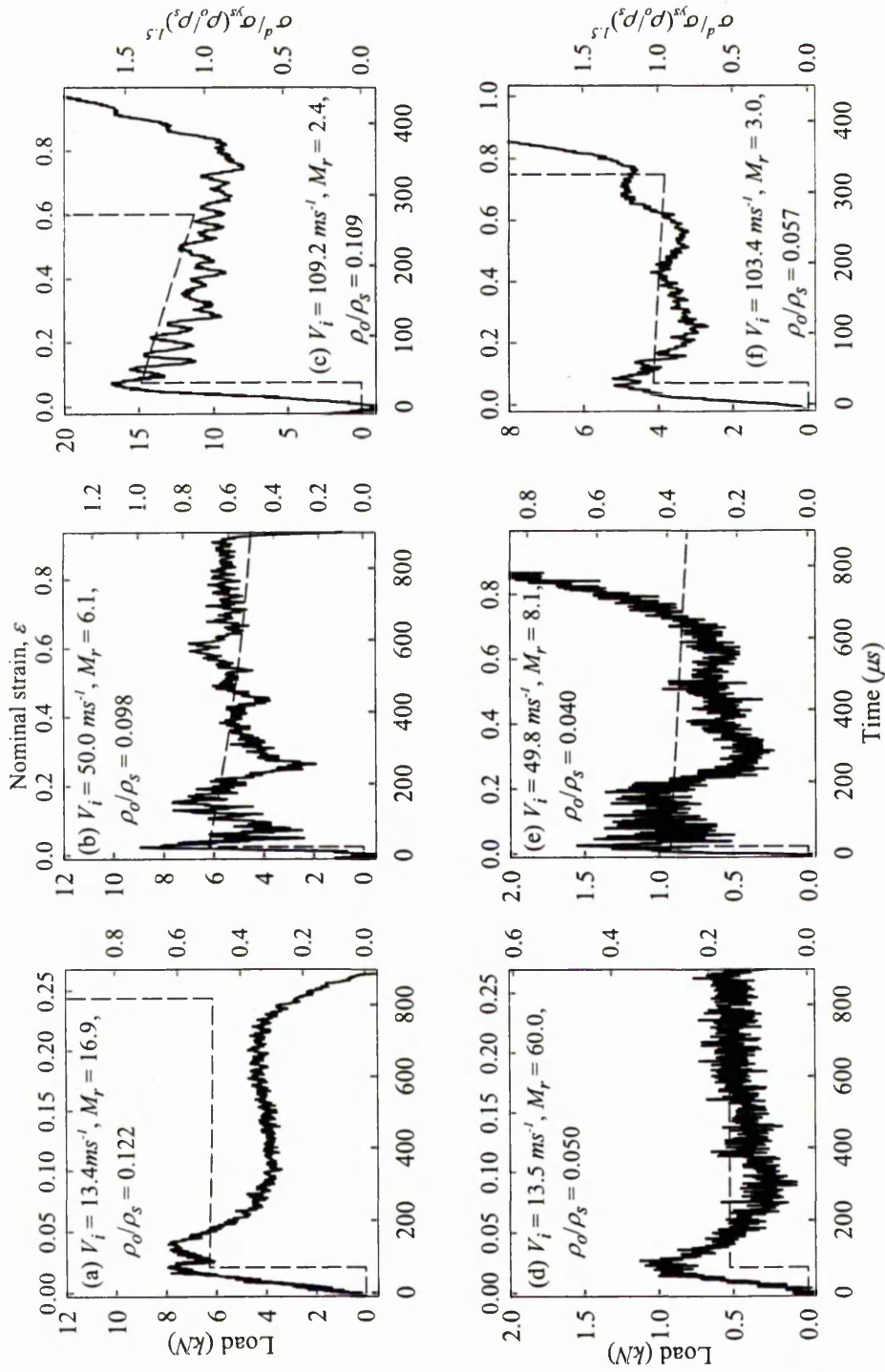
Figure 4.7 – Comparison between theory (dotted line) and experimental force pulses (solid lines) for *small* (a-c) and *large* (d-f) cell cylindrical *y*-axis specimens at different impact velocities V_i.
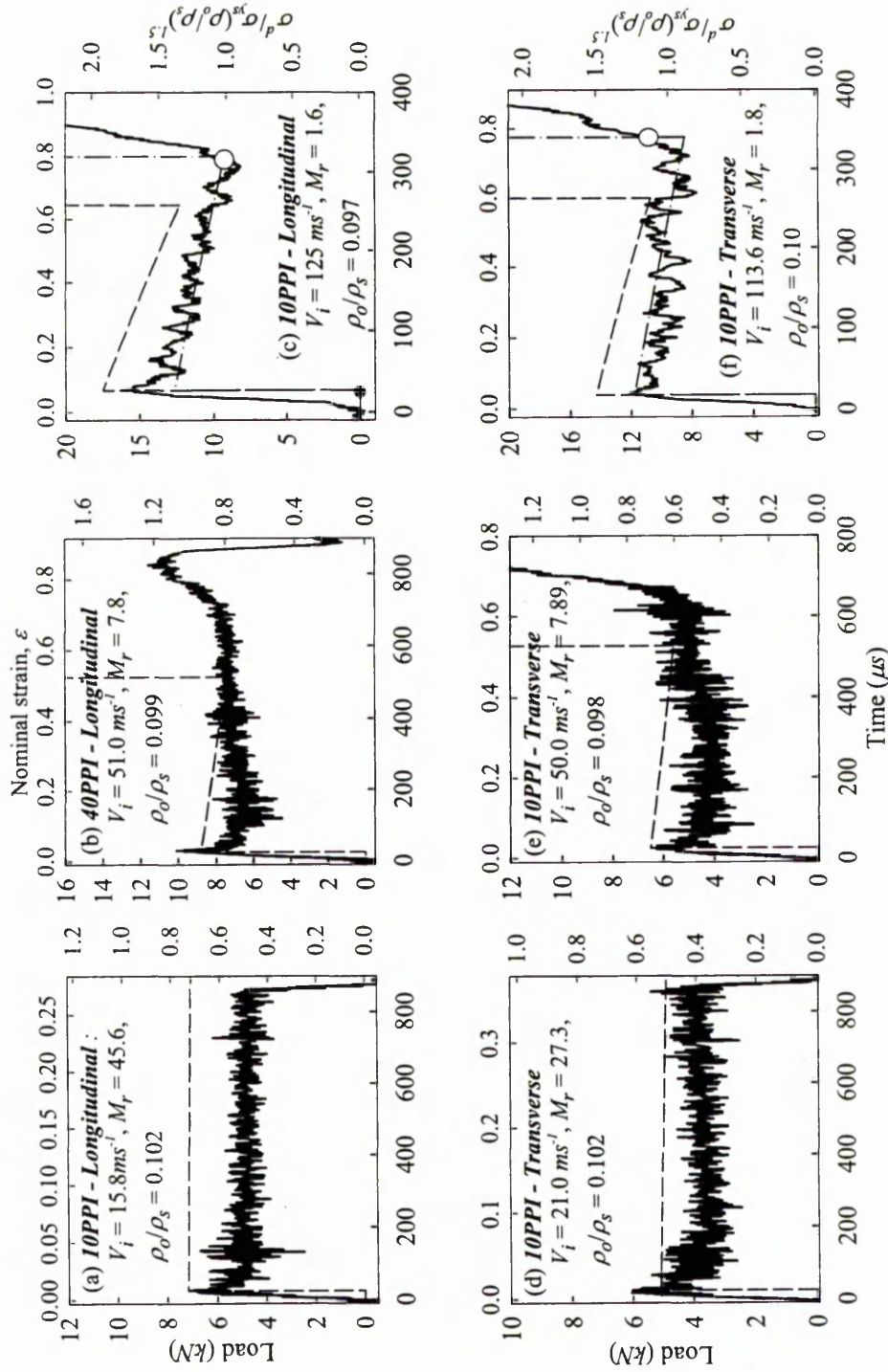
Figure 4.8 - Comparison between theory (dotted line) and experimental force pulses (solid lines) for Duocel foams along the largest (a-c) and smallest (d-f) principal dimension of their constituent cells. The dash-dot line in (c) and (f) are theoretical prediction by using the densification strain from the dynamic force pulse measured.
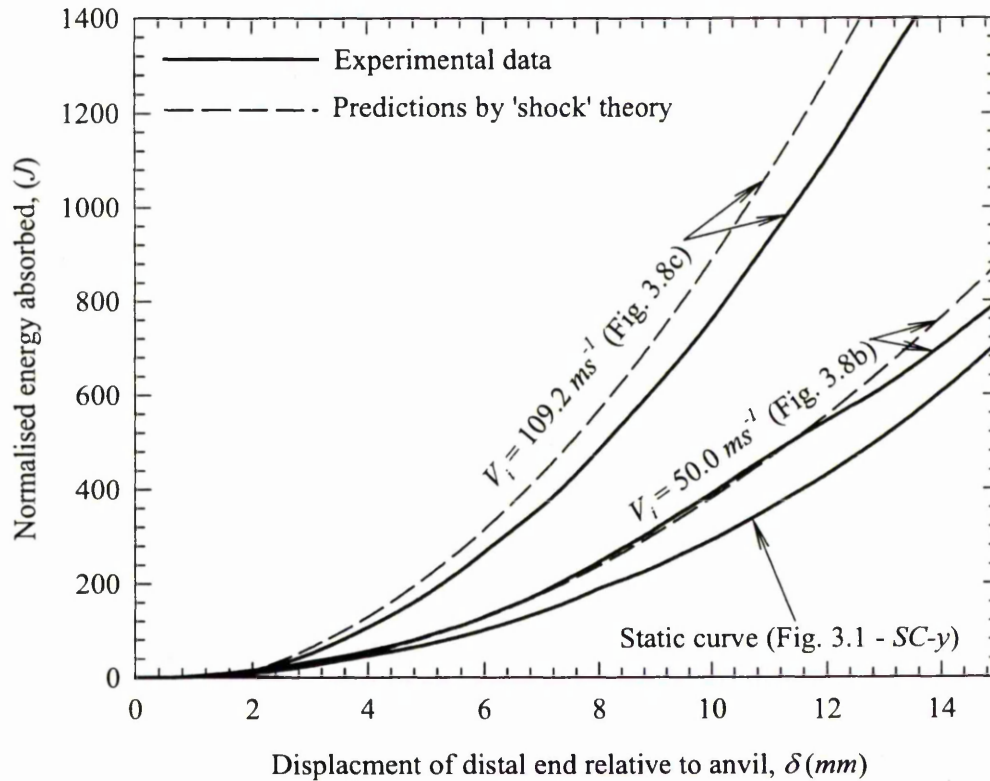
Figure 4.9 – Comparison between the experimental data for the energy absorbed (normalised by $(\rho_o/\rho_s)^{1.5}$) and the predictions by the 'shock' theory.

The theoretical dynamic plastic collapse stress is given by Eqn. (4.44) and the theoretical dynamic plateau stress is defined as the time average value of $\sigma^d(t)$, Eqn. (4.43), according to

$$\sigma_{pl}^d = \langle \sigma^d \rangle = \frac{1}{t_D} \int_0^{t_D} \sigma^d(t)\,dt \qquad (4.67)$$

where t_D corresponds to the time where rigid locking of the whole of the foam specimen has occurred. They are plotted with their corresponding experimental data in Figs. 4.10 and 4.11 for the Cymat foams and in Figs 4.12 and 4.13 for the Duocel foams.
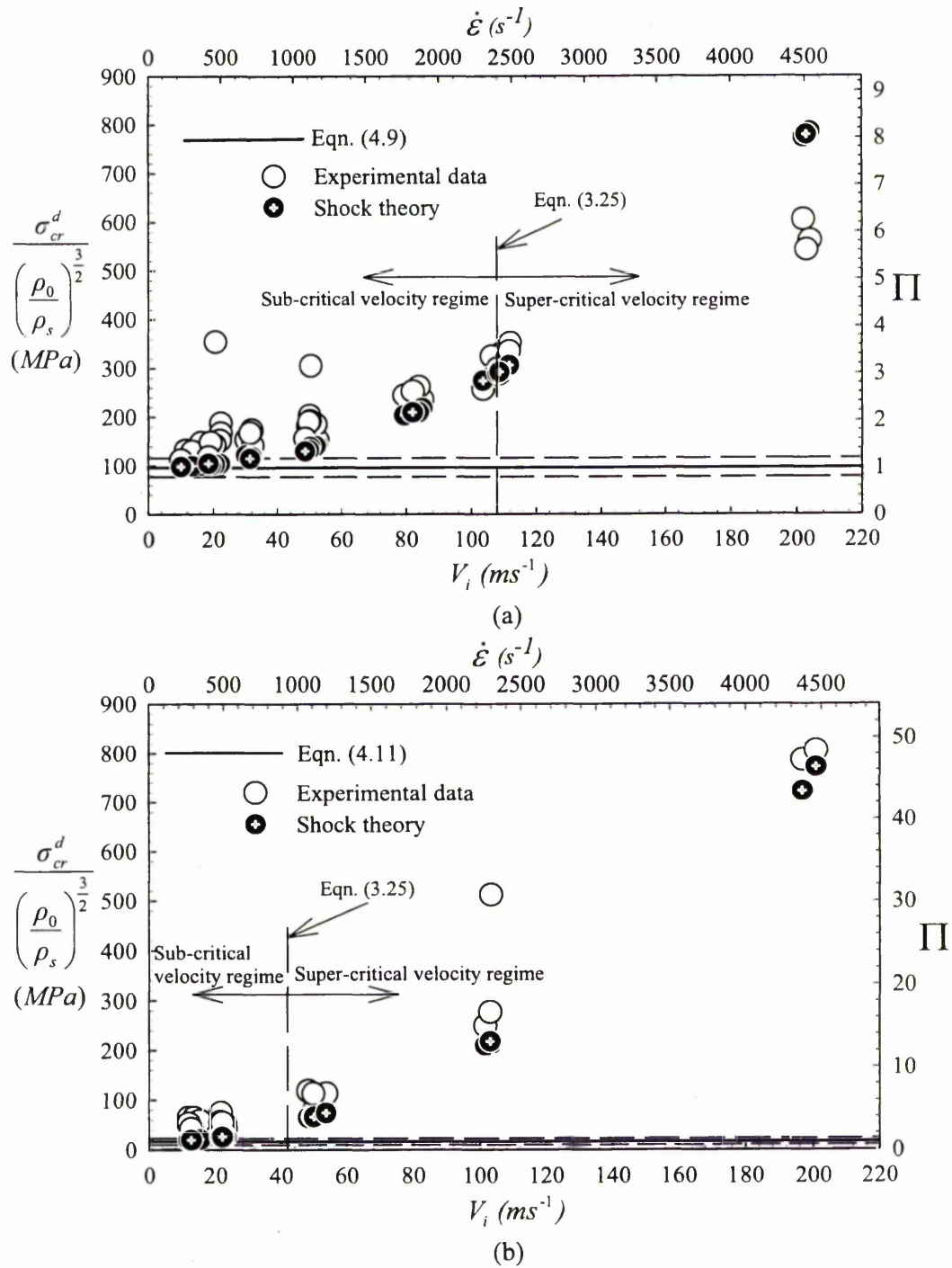
Figure 4.10 – Comparison between theory and experiment for the normalised plastic collapse stress of (a) *small* cell and (b) *large* cell *y*-axis specimens. The dashed lines indicate corresponding quasi-static scatter in loads and $\dot{\varepsilon}$ is the nominal engineering strain rate.
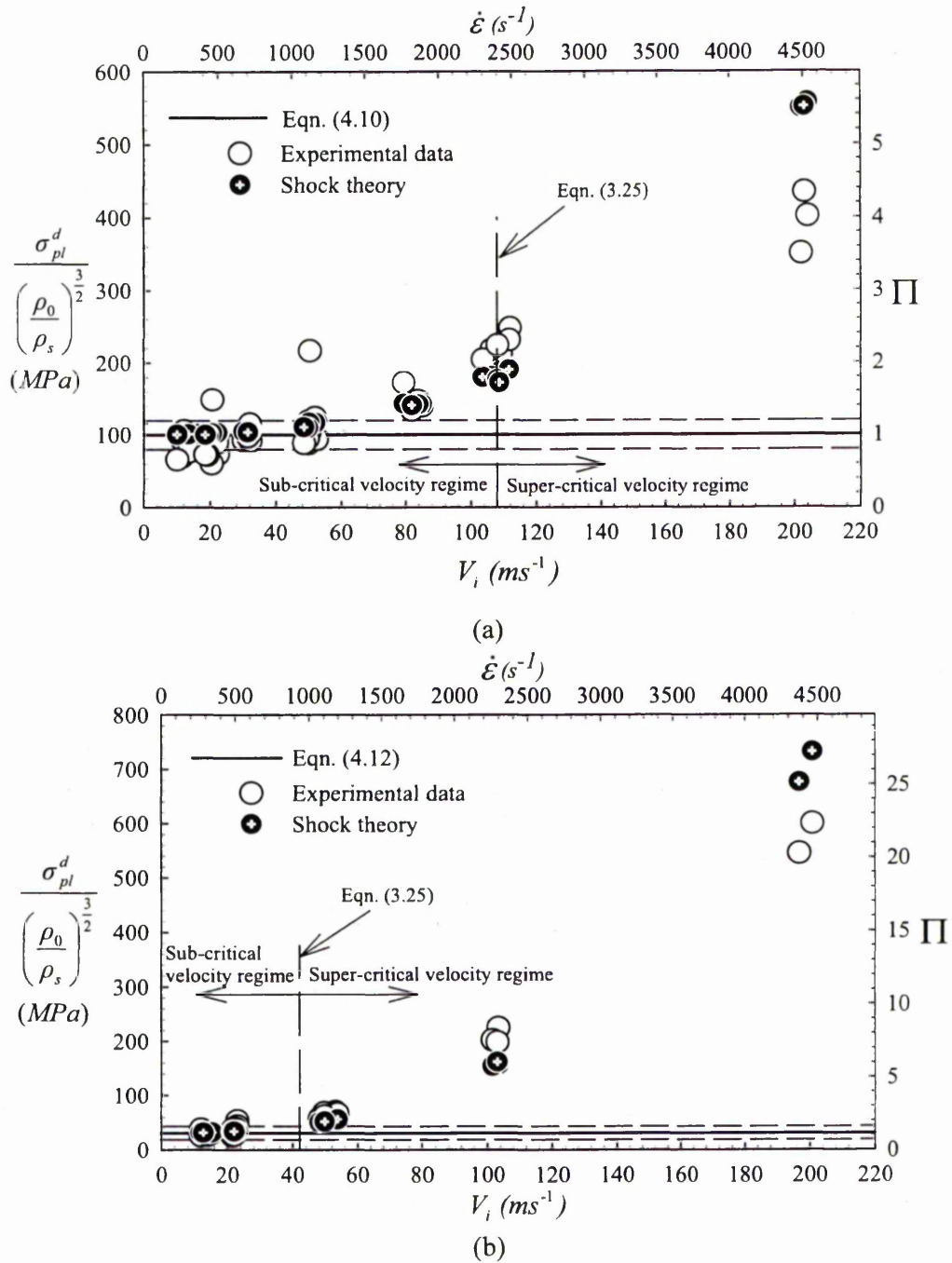
Figure 4.11 – Comparison between theory and experiment for the normalised plateau
stress of (a) *small* cell and (b) *large* cell *y*-axis specimens. The dashed
lines indicate corresponding quasi-static scatter in loads and $\dot{\varepsilon}$ is the
nominal engineering strain rate.
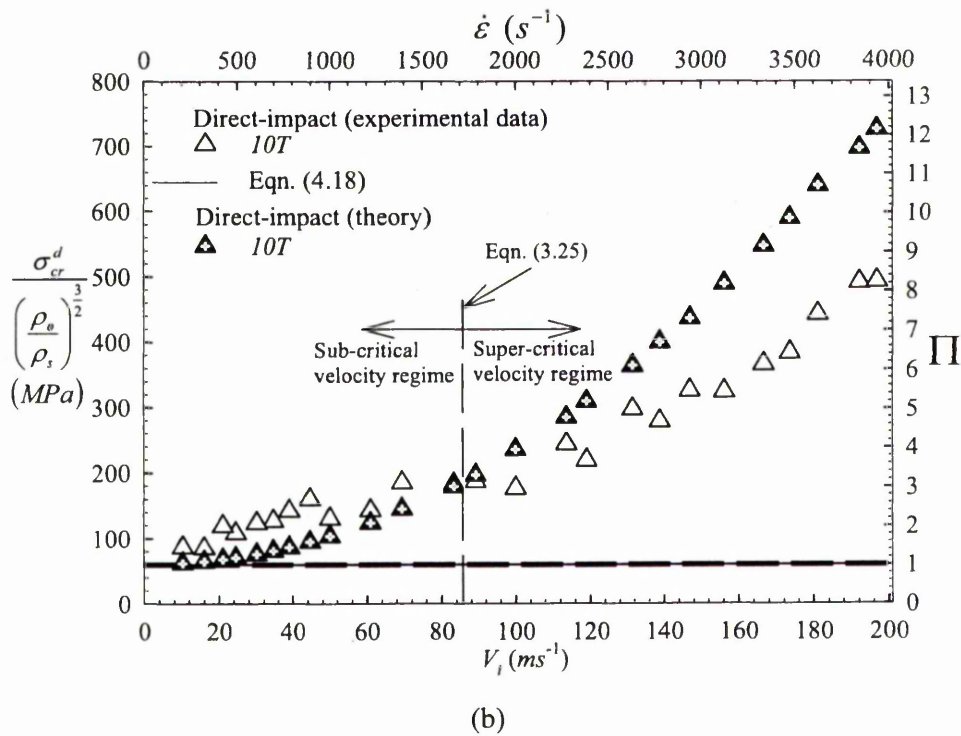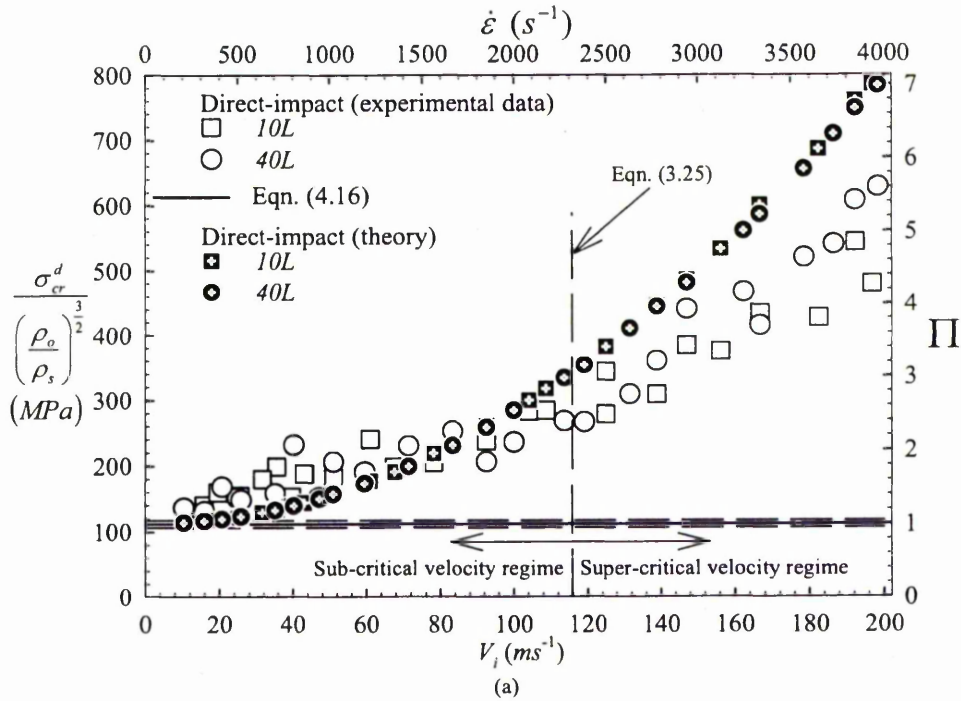
Figure 4.12 – Comparison between theory and experiment for the normalised plastic collapse stress for Duocel foams along the (a) largest and (b) smallest dimension of their constituent cells.
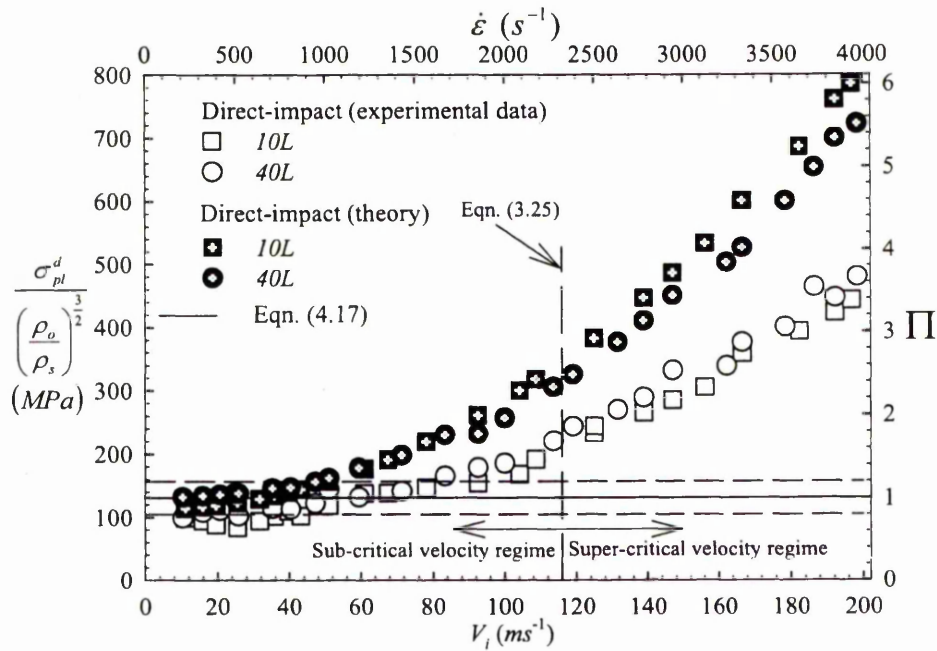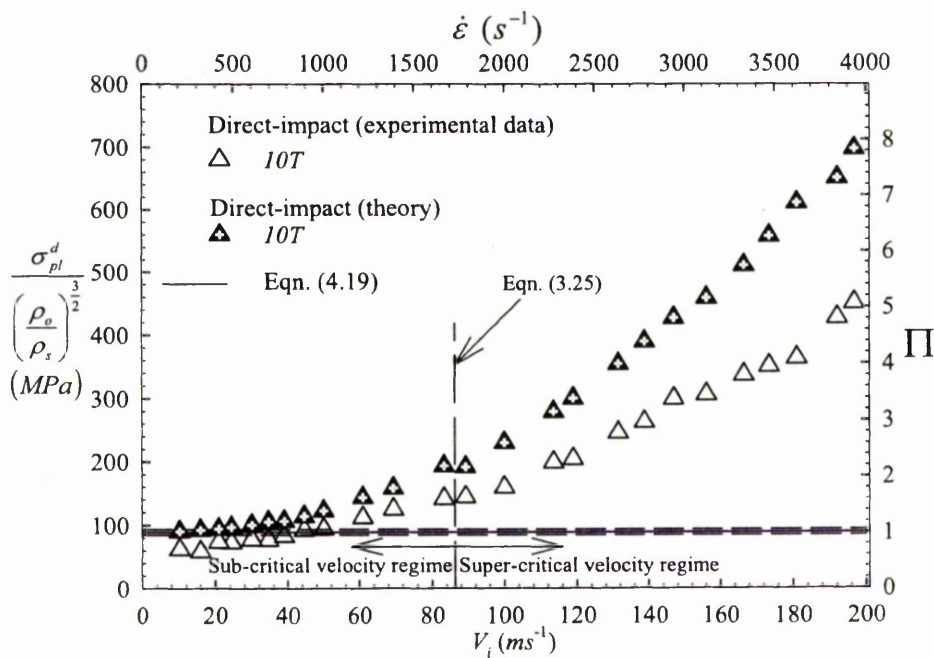
Figure 4.13 – Comparison between theory and experiment for the normalised plateau stress for Duocel foams along the (a) largest and (b) smallest dimension of their constituent cells.

The experimental data plotted in Figs. 4.10 and 4.11 shows that 'size effect' remain active in the *large* cell Cymat foams during sub-critical velocity compression. By contrast, the dynamic strength properties in the super-critical velocity regime are unaffected by 'size effect' and morphological defects; rather they are influenced primarily by the impact velocity. The predicted plastic collapse, σ_{cr}^d, and plateau, σ_{pl}^d, stresses of the Cymat foams agree reasonably well with their experimental data. In particular, the quadratic trend of the variation of the plastic collapse and plateau stresses in the super-critical velocity régime has been reproduced qualitatively. The theory provides a better prediction of the strength properties for the *large* cell foam because its nominal stress-strain curve is better approximated by a rigid response at the densification strain (locking). The discrepancy between theory and experiment for the *small* cell foam at the higher impact velocities is a result of the higher levels of strain achieved experimentally than are possible analytically when using the simplified material model given by Eqn. (4.30).

Figure 4.12 shows that the theory consistently under-predicts the plastic collapse strength of the Duocel foams in the sub-critical velocity regime but over-predicts in the super-critical velocity regime; this is irrespective of the orientation of their constituent cells. The reason for the over-prediction is the same for the Cymat foams given above. At sub-critical impact velocities, the 'shock' model consistently underestimates the plastic collapse stress due to microinertia effects and the plastic wave model should be used instead. This shows that the dynamic response of metal foams in an impact (non-zero initial velocity) process exhibits Type-II structural characteristics, irregardless of the form of their quasi-static force-displacement curve; see, for example, the *10T* specimens. By analogy with the previous work on 0° wood specimens (Reid and Peng, 1997), one can argue that the plastic collapse stress will increase more substantially than the 'shock' theory can predict. The consistent over-prediction of the plateau stresses by the model in Fig. 4.13 is probably due to the effects of internal wave reflection in the foam material which is not considered in the 'shock' model.

In general, it can be argued, based on an extension of the results from studies on

2D regular honeycombs (see Hönig and Stronge, 2002a,b), that dynamic localisation of crushing, or 'shock' propagation, is not responsible for the significant plastic collapse stress enhancement in the sub-critical velocity régime of the Cymat (Fig. 4.10) and Duocel (Fig. 4.12) foams. Rather, it is due to the translational and rotational inertia of their cell walls, which is analogous to the lateral inertia effects in Type II structures (Reid et al., 1983). In other words, dynamic strength enhancement is not always an indication of 'shock' propagation *per se*. This contrasts with the findings of Deshpande and Fleck (2000). In general, the 'shock' theory under-predicts the dynamic plastic collapse stresses of the foams in the sub-critical velocity regime because of the different enhancement mechanism. The simple one-dimensional plastic wave theory, given in Chapter 3, provides a better estimate of the plastic collapse stress in the sub-critical velocity régime.

Adiabatic 'shock' compaction of a non-heat-conducting foam rod was assumed to occur. In reality, 'shock' changes are not strictly adiabatic; rather, a finite amount of heat energy is generated within the specimen through plastic deformation in the cell walls. The precise nature of the stress-strain relation across the 'shock' is not known at high impact velocities and is most likely to differ somewhat from the adiabatic stress-strain relation used in Eqns. (4.9) and (4.30). However, Zaretsky and Ben-Dor (1995) have shown that the adiabatic relation provides a sufficiently good approximation of the 'shock' Hugoniot curve for flexible foams. The present study assumes that this is also the case for metal foams.

For quasi-static compression and dynamic compression in the sub-critical velocity regime there is a characteristic length scale associated with the collapse mechanisms that evolve. Any attempt to use the classical continuum wave theory to model the progression of deformation through aluminium foams in the sub-critical velocity appears futile because of the negative slope in their stress-strain curves, due to local softening associated with the individual cell collapse, and so therefore do not admit wave-type solutions. The difficulties are further complicated by the need to introduce multi-scale effects generated by the cellular geometry. Similarly, there is a characteristic wave thickness associated with the propagating 'shock' front at the

super-critical velocities. The thickness of the 'shock' front is the result of a balance struck between dissipative effects and the tendency of the propagating waves to evolve towards a 'shock' due to the rapidly decreasing compressibility of the material (Lighthill, 1956). The dissipative effects are a consequence of the finite time required for cell collapse due to inertial effects. The issue concerning the length scales associated with different deformation responses in the transition from a sub-critical velocity regime to a super-critical velocity regime becomes immediately apparent. The issue of whether a steady 'shock' can evolve and propagate in a foam material remains to be quantified. However, numerical simulations of 2D Voronoi honeycombs suggest that a travelling steady 'shock' solution may exists and this is examined next.

4.4.2. Comparison with results of numerical simulations of 2D Voronoi honeycombs[4]

In this section, the dynamic crushing of 2D Voronoi honeycombs is studied by finite elements (ABAQUS explicit) simulations. The technique used to generate 2D Voronoi honeycombs with varying degree of cell irregularity is first described. Let the minimum Euclidean distance d_s between any two neighbouring nuclei (or points), say p and q, in a plane be

$$d_s = dist(p,q) := \sqrt{(p_x - q_x)^2 + (p_y - q_y)^2} \, . \qquad (4.68)$$

If no restriction is placed on how the nuclei are to be 'seeded' in the plane, then the inequality $dist(a,b) \geq d_s$ must hold for any pair of nuclei *a and b*. If the nuclei are to be 'seeded' such that the Euclidean distance between any pair of neighbouring nuclei is always equal; then there exists a maximum value for d_s given by

$d_s^{max} = \left(2A/n\sqrt{3}\right)^{1/2}$, where n and A is the number of nuclei and the area of the plane,

---

[4] Parts of the work reported in this section were carried out in collaboration with Z. Zou, S.R. Reid, S. Li, and J.J. Harrigan (see paper no. 5 and 6 in Section 1.4).

respectively. To provide a measure of the extent of cell irregularity in 2D Voronoi honeycombs with identical number of nuclei within a plane of area A, Zhu et al. (2001) introduced the non-dimensional parameter Λ, defined by

$$\Lambda := d_s / d_s^{max} \quad \text{for } 0 < \Lambda \le 1. \tag{4.69}$$



(a)   (b)
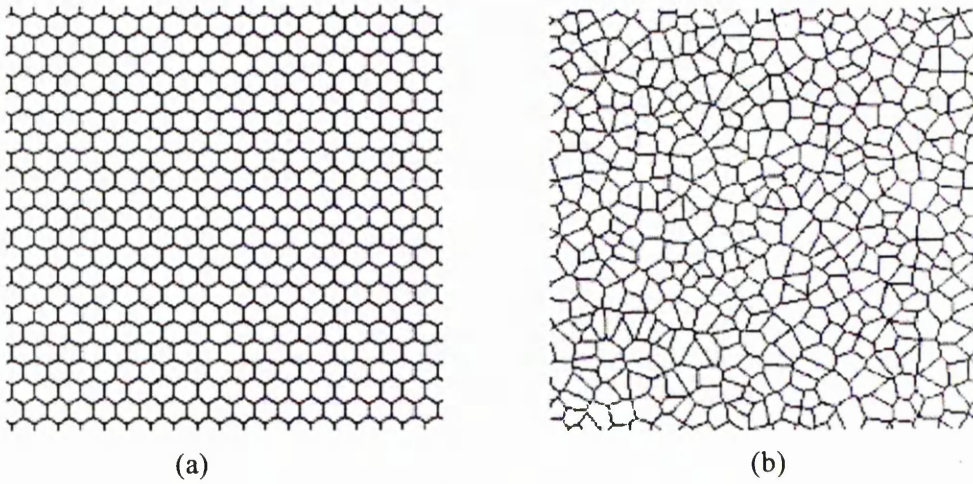
Figure 4.14 – Two-dimensional Voronoi honeycombs where (a) $\Lambda = 1$ and (b) $\Lambda = 0.5$.
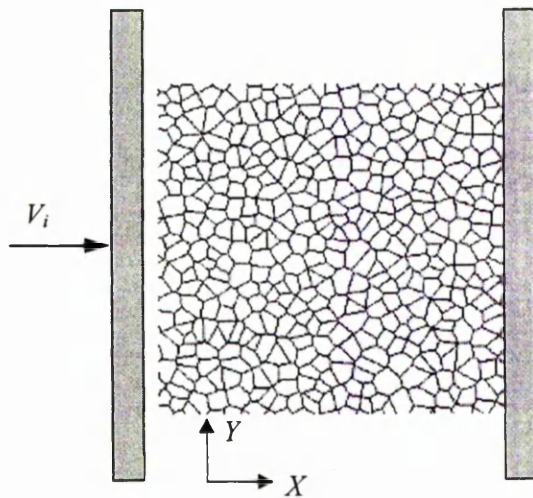

Figure 4.15 – Loading conditions for the Voronoi honeycomb

Once the nuclei are seeded, a 2D Voronoi honeycomb is easily generated by using the same technique described by Silva et al. (1995). Figures 4.14a and b show Voronoi honeycombs for $\Lambda = 1$ (19 x 22 regular cells of 4mm edge length and 0.34mm wall thickness) and $\Lambda = 0.5$ (~ 400 cells and 0.32mm wall thickness) respectively. Both have a relative density of 0.1. Their aluminium cell walls are prescribed with rate-independent, elastic, perfectly-plastic properties identical to those used by Chen et al. (1999). Each cell wall is modelled using 1 to 15 general-purpose shell elements (S4R) and self-contact simulations are incorporated in the model. The foams are compressed at constant velocities of $10ms^{-1}$, $50ms^{-1}$ (sub-critical) and $100ms^{-1}$ (super-critical) from the left, whilst their right-end remains fixed as shown in Fig. 4.15.

The distribution of crushed cells in the 2D Voronoi honeycombs (Figs. 4.16 and 4.17) is consistent with those seen in 3D Cymat/Hydro foams at the different velocity regimes. Bands of non-contiguous crushed cells develop at a sub-critical impact velocity giving a somewhat diffused deformation pattern. By contrast, sequential cell crushing (or 'shock' wave propagation) occurs at a super-critical impact velocity. Figure 4.18 shows the variation of the internal energy density (using the identifier 'ALLIE' in ABAQUS) in the Voronoi honeycombs compressed at three super-critical velocities. Since all forms of non-mechanical energies, and the energy dissipated by viscous effects and by time-dependent deformation are not considered in the FE model, the only contributions to the internal energy are the recoverable elastic strain energy and the energy dissipated by plasticity (ABAQUS, 2002). Note that the former is negligibly small. The upturn at the end of each curve indicates an increased in the energy absorbed by the 2D honeycombs at full locking with impact velocity. It is evident from Fig. 4.18 that the two key parameters controlling the energy absorption capacity of these honeycombs are the relative density and the impact velocity. By contrast, cell micro-structural irregularities (Λ) had little effect. Zou et al. (2005) have shown that the energy dissipated through rate-independent plastic deformation in the cell edges occurs mainly in the vicinity of the collapsing cells, or crush front, and they account for more than 95% of the internal energy
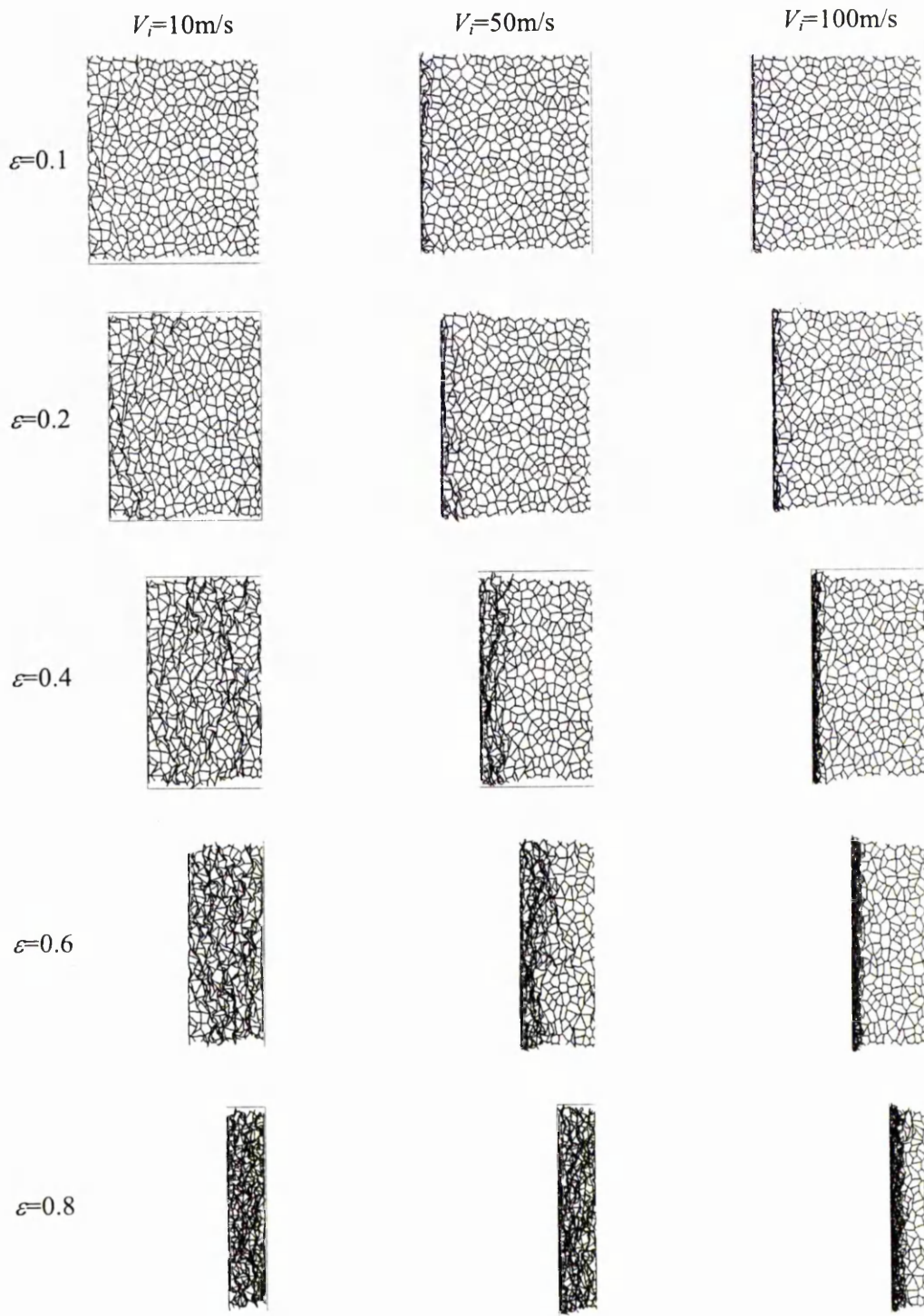
Figure 4.16 – Deformation of 2D Voronoi honeycombs ($\Lambda = 0.5$) under in-plane compression at different impact velocities.
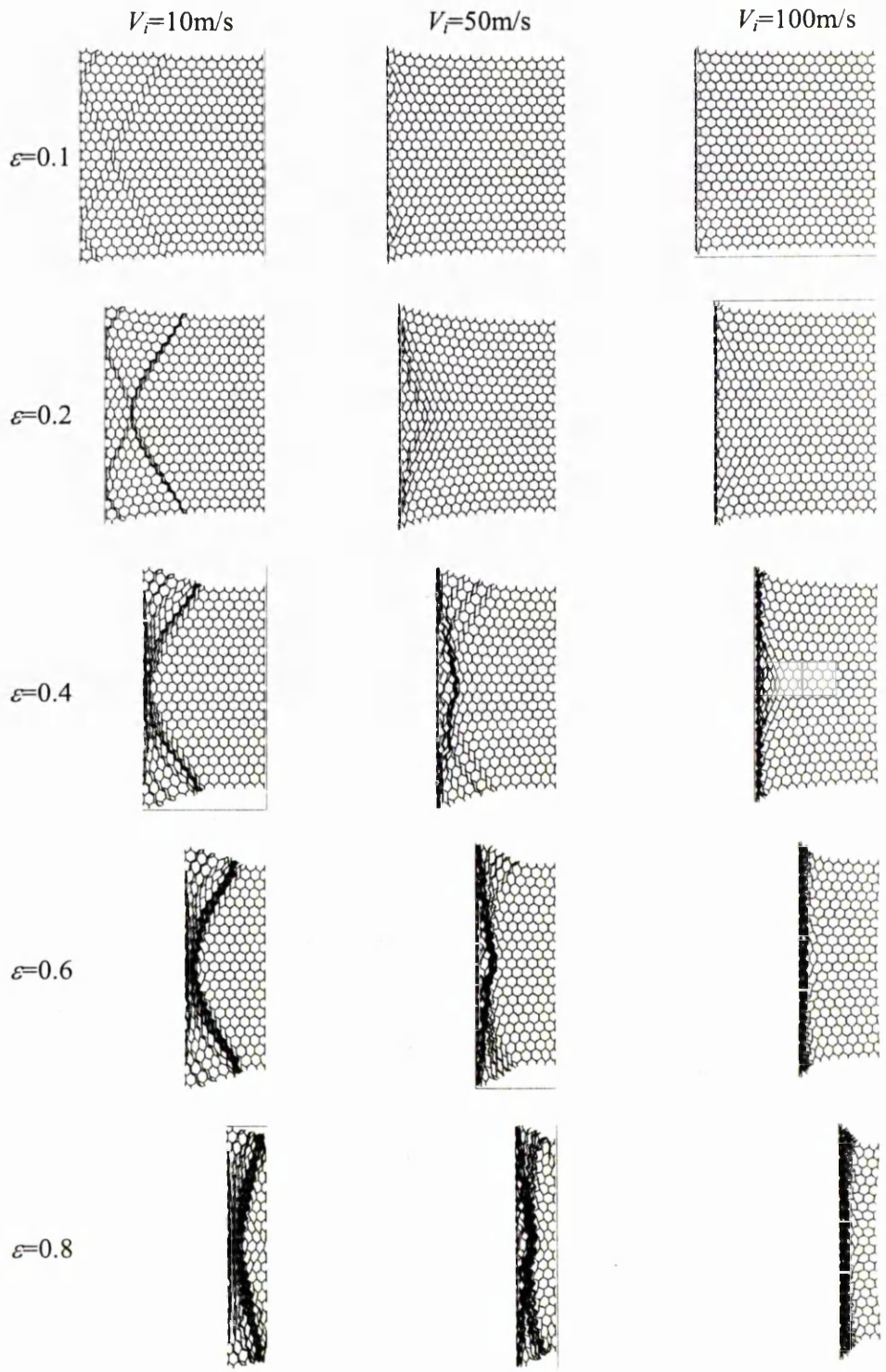
Figure 4.17 – Deformation of 2D Voronoi honeycombs ($\Lambda = 1$) under in-plane compression at different impact velocities.
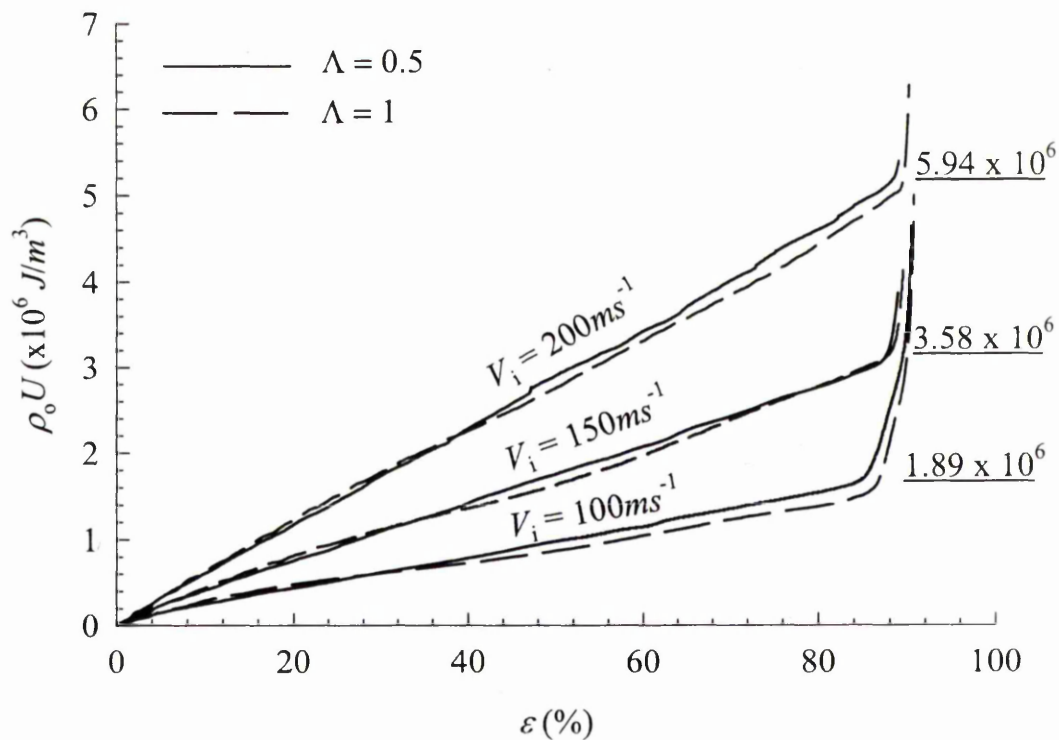
Figure 4.18 – Internal energy density of 2D Voronoi honeycombs ($\Lambda = 1$ and $\Lambda = 0.5$) versus the percentage nominal strain at three velocity levels. The overall energy absorbed at full locking predicted by Eqn. (4.70) for each velocity is given by the underscored values.

density plotted. From Eqns. (4.26) and (4.37), it is easily shown that

$$[\rho_o U] = \sigma^+[\varepsilon] + \rho_o[v]^2/2 . \tag{4.70}$$

The predictions by Eqn. (4.70) of the overall energy absorbed at full locking (identified by the upturn in each curve) are given by the under-scored values in Fig. 4.18. They agree well with the results of the numerical simulations. The parameters used in their calculations were $[\varepsilon] = \varepsilon_D = 0.9$, $\sigma^+ = 0.9 MPa$ and $[v] = V_i$. The stress ahead of the 'shock' (σ^+) is assumed to be that measured at the fixed-end. It was found to be nearly constant throughout the compression process and varies little with

the impact velocity.

The above numerical example shows that the increased energy absorbed by the 2D Voronoi honeycombs (without trapped gas) can be attributed directly to rate-independent plastic deformation in their cell edges as a result of the dynamic localisation of crushing, or 'shock' wave propagation. This is an inertial phenomenon wherein the dynamic localisation of crushing is responsible for the increased energy absorbed by the Voronoi honeycomb. Although a full analysis of 3D foams is not yet available, it is expected that the same explanations given above could also be extended to 3D foams under super-critical velocity compression.
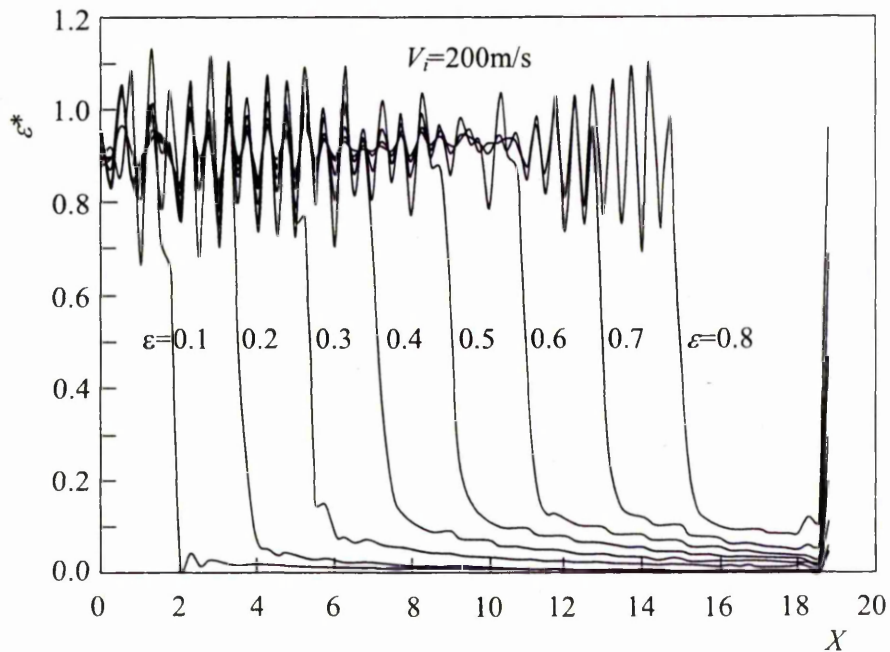
Figure 4.19 – Distribution of local compressive nominal strain along the X-axis of a Voronoi honeycomb ($\Lambda = 1$) subjected to an impact velocity of $200ms^{-1}$

Figure 4.19 shows the distribution of the local compressive nominal strain along the X-axis of a Voronoi honeycomb ($\Lambda = 1$) subjected to a constant velocity compression of $200ms^{-1}$. It shows an abrupt drop in the compressive strain across

the shock front over a single cell width and the compressive waveform propagates approximately unchanged in form along the X-axis. The simulation suggests that a travelling steady 'shock' solution may exist but its detailed investigation is left for future work.

4.5. Conclusions

It has been shown that a continuous process of elastic-plastic stress wave propagation into a uniform region in which the mechanical behaviour is represented by a single concave upwards stress-strain relation cannot be maintained indefinitely in a strain-hardening foam rod (Hanssen et al., 2002) and ultimately the plastic wave must show discontinuities, leading to the formation of a 'shock'.

The general quadratic trend of the variation of the dynamic plastic collapse and plateau stresses with impact velocity, evident in the experimental data, is captured well by the simple r-p-p-l one-dimensional 'shock' theory. The kinematic existence condition for 'shock' compaction of the foam rod has been established by thermodynamics arguments and it predicts the impact velocity for transition to a 'shock'-type deformation response of approximately $108ms^{-1}$ (*small* cell foam) , $42ms^{-1}$ (*large* cell foam), $116ms^{-1}$ (*10L & 40L*) and $85ms^{-1}$ (*10T*) which compares well with the experimental data.

Dynamic localisation of crushing is not always responsible for the significant plastic collapse stress enhancement in the sub-critical velocity regime. Rather, this can be due to Type-II micro-inertial effects. Dynamic strength enhancement is not always accompanied by 'shock' propagation *per se*. Inertial effects associated with the dynamic localisation of crushing are responsible for the enhancement of the dynamic strength properties in the super-critical velocity regime. The predictions of the 'shock' theory compare well with the experiment data in this velocity regime where size effects and morphological defects are insignificant. In the sub-critical velocity regime, both effects influence the dynamic strength properties.

Chapter 5

Comments on the applications of the Rankine-Hugoniot relations and the 'steady-shock' theory in recent literature

5.1 Introduction

The last few years have seen rise in the use of the one-dimensional 'steady-shock' theory, such as the one presented in Chapter 4, to formulate simple predictive models, in particular for the dynamic compressive response of metal foams (Lee et al., 2005) and for other micro-architectured core materials in blast-resistant sandwich beams (Fleck and Deshpande, 2004; Deshpande and Fleck, 2005). Section 5.2 revisits the one-dimensional model on the interaction between a shock, generated by explosions in air and underwater, and the front-face of a sandwich beam structure by Fleck and Deshpande (2004). Three important and related issues on the estimation of the peak overpressure acting on the front face of the sandwich beam following the reflection of the shock are discussed. In Section 5.3, anomalies between the 'steady-shock' theory presented in Chapter 4 and those in the current literature are discussed by examples and by results of FE simulations of 2D Voronoi honeycombs.

5.2 The one-dimensional fluid-structure interaction model (Stage I) of Fleck and Deshpande (2004)

In this section the one-dimensional (1D) fluid-structure interaction model proposed by Fleck and Deshpande (2004), denoted by FD hereinafter, is revisited. Suppose a shock wave is generated following an explosion in air and this interacts with a sandwich beam. The Rankine-Hugoniot relations are first reviewed which then provide a basis for estimating the peak overpressure acting on the front face of

the sandwich beam following the reflection of the shock.

5.2.1 The Rankine-Hugoniot relations (Lighthill, 1956; Billingham and King, 2000)

For simplicity assume that the shock is planar and lies at $x = s(t)$ and is propagating in air. Figure 5.1 shows a planar shock in a frame of reference moving with the shock, with spatial co-ordinates $\bar{x} = x - \dot{s}$. The flux of mass, momentum and energy must be continuous at the shock, whilst the pressure, density and internal
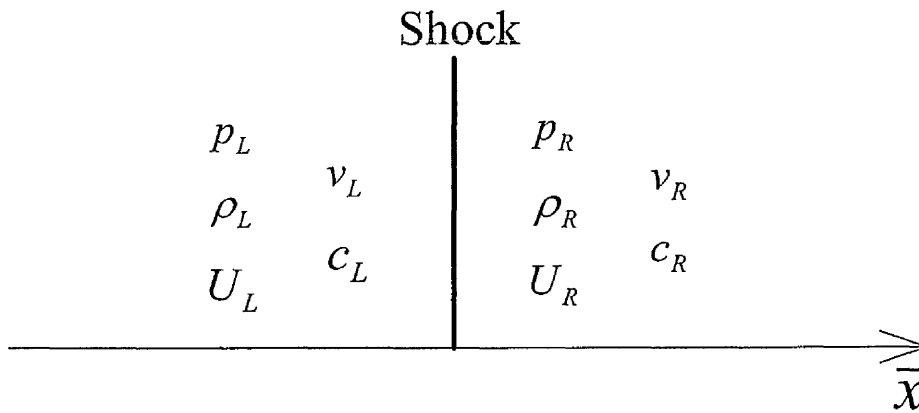
Shock

Figure 5.1 – The various physical quantities on either side of a planar shock in a frame of reference moving with the shock.

energy of the gas need not be continuous. This is expressed by the well-known Rankine-Hugoniot relationships, viz.

$$\rho_L \bar{v}_L = \rho_R \bar{v}_R \; , \tag{5.1}$$

$$\rho_L \bar{v}_L^2 + p_L = \rho_R \bar{v}_R^2 + p_R \; , \tag{5.2}$$

$$\left(\rho_L \bar{v}_L^2 / 2 + \rho_L U_L + p_L \right) \bar{v}_L = \left(\rho_R \bar{v}_R^2 / 2 + \rho_R U_R + p_R \right) \bar{v}_R \tag{5.3}$$

where quantities immediately to the left and right of the shock are denoted, respectively, by subscripts L and R; $\bar{v}$ ($\equiv v - \dot{s}$) is the particle velocity relative to the shock, $\dot{s}$ is the shock velocity, ρ is density, p is pressure and U is the internal

energy per unit mass. Since $U = p/\rho(\gamma - 1)$ for an ideal gas, where γ is the ratio of specific heats ($\equiv C_p/C_V$ where C_p and C_V are the specific heat at constant pressure and volume, respectively), Eqn. (5.3) can be rewritten as

$$\left(\bar{v}_L^2/2 + \gamma p_L/(\gamma - 1)\rho_L\right)\rho_L\bar{v}_L = \left(\bar{v}_R^2/2 + \gamma p_R/(\gamma - 1)\rho_R\right)\rho_R\bar{v}_R \qquad (5.4)$$

and using Eqn. (5.1) gives

$$\bar{v}_L^2/2 + \gamma p_L/(\gamma - 1)\rho_L = \bar{v}_R^2/2 + \gamma p_R/(\gamma - 1)\rho_R . \qquad (5.5)$$

Under adiabatic conditions, the equation of state of an ideal gas (one where there is no interaction between the air molecules) is

$$PV^\gamma = \text{constant}. \qquad (5.6)$$

Differentiating Eqn. (5.6) gives

$$\gamma p = -Vdp/dV = B \qquad (5.7)$$

and the local sound speed is

$$c = \sqrt{B/\rho} = \sqrt{\gamma p/\rho} . \qquad (5.8)$$

For an ideal gas, the Rankine-Hugoniot relations are normally written in terms of the local sound speed (Eqn. 5.8) as follows:

$$\rho_L\bar{v}_L = \rho_R\bar{v}_R , \qquad (5.9)$$

$$\rho_L\left(\bar{v}_L^2 + c_L^2/\gamma\right) = \rho_R\left(\bar{v}_R^2 + c_R^2/\gamma\right) , \qquad (5.10)$$

$$\bar{v}_L^2/2 + c_L^2/(\gamma - 1) = \bar{v}_R^2/2 + c_R^2/(\gamma - 1) . \qquad (5.11)$$

Since the Rankine-Hugoniot relations provide three equations in six unknowns, it is possible to eliminate any two to obtain a single equation involving four unknown quantities. For example, one can eliminate p_R and ρ_R from Eqns. (5.9) to (5.11) to give

$$\left(\frac{2}{\gamma+1}\right)\bar{v}_L^2 + \left(\bar{v}_R - \bar{v}_L\right)\bar{v}_L - \left(\frac{2\gamma}{\gamma+1}\right)\frac{p_L}{\rho_L} = 0.$$

(5.12)

5.2.2 Normal reflection of a shock from a planar solid wall (Taylor, 1963b)
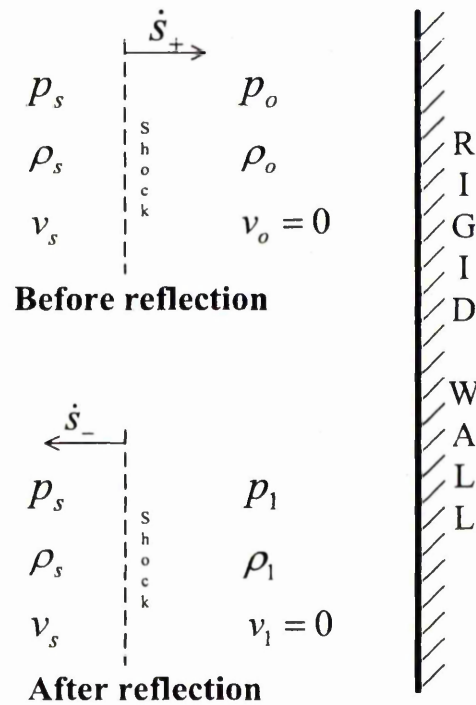
Figure 5.2 – Normal reflection of a shock from a rigid wall

Fleck and Deshpande (2004) argued that the front face sheet of the sandwich beam may be assumed to be fixed and rigid because of the large jump in acoustic impedance with air, i.e. full transmission of the blast impulse to the sandwich beam must be considered. Hence, the problem to be solved is equivalent to the normal reflection of a shock from a solid, stationary wall. The solution to this equivalent

problem is given by Taylor (1963b) whose analysis is summarized here (by adopting a different approach). Consider the case of a rightward propagating shock as shown in Fig. 5.2. Let the velocity of the shock before it reaches the rigid wall be $\dot{s}_+$, and the gas pressure, density and normal velocity behind the shock be p_s, ρ_s and v_s, respectively. The initial ambient gas pressure and density ahead of the shock is p_o and ρ_o. However, continuity requires that the normal velocity of the gas molecules be zero at the wall. The particle velocity, in a frame of reference moving with the shock, on either side of the shock before reflection is

$$\bar{v}_L = v_s - \dot{s}_+ \quad \text{and} \quad \bar{v}_R = -\dot{s}_+. \tag{5.13}$$

Substituting into Eqn. (5.12) gives

$$\left(\frac{2}{\gamma+1}\right)(v_s - \dot{s}_+)^2 - v_s(v_s - \dot{s}_+) - \left(\frac{2}{\gamma+1}\right)(p_s/\rho_s) = 0. \tag{5.14}$$

Let the normal shock velocity immediately after reflection from the wall be $-\dot{s}_-$. The gas pressure p_1 and density ρ_1 at the wall are not known although the normal velocity at the wall is still zero. The gas pressure, density and normal velocity on the other side of the shock are still p_s, ρ_s and v_s, as shown in Fig. 5.2. The relative particle velocity on either side of the shock after reflection now becomes

$$\bar{v}_L = v_s + \dot{s}_- \quad \text{and} \quad \bar{v}_R = \dot{s}_- \tag{5.15}$$

and substitution into Eqn. (5.12) gives

$$\left(\frac{2}{\gamma+1}\right)(v_s + \dot{s}_-) - v_s(v_s + \dot{s}_-) - \left(\frac{2}{\gamma+1}\right)(p_s/\rho_s) = 0 \tag{5.16}$$

It is obvious from Eqns. (5.14) and (5.16) that both $v_s - \dot{s}_-$ and $v_s + \dot{s}_-$ satisfy the

same quadratic equation given by Eqn. (5.12) (which is of the form $A\bar{v}_L^2 + B\bar{v}_L + C = 0$) and are, therefore, its two roots whose product satisfies

$$\left(v_s - \dot{s}_-\right)\left(v_s + \dot{s}_-\right) = -C/A = -\gamma p_s/\rho_s .$$ (5.17)

Eliminating $\bar{v}_R$ and ρ_R from Eqns. (5.9) – (5.11) give

$$\left(\frac{2}{\gamma+1}\right)\frac{\rho_L \bar{v}_L^2}{p_L} - \frac{p_R}{p_L} - \frac{\gamma-1}{\gamma+1} = 0 .$$ (5.18)

Substituting the various quantities on either side of the shock before and after reflection into Eqn. (5.18) gives

$$\left(\frac{2}{\gamma+1}\right)\frac{\rho_L \left(v_s - \dot{s}_+\right)^2}{p_L} - \frac{p_o}{p_s} - \frac{\gamma-1}{\gamma+1} = 0 \quad \text{and}$$ (5.19)

$$\left(\frac{2}{\gamma+1}\right)\frac{\rho_L \left(v_s + \dot{s}_-\right)^2}{p_L} - \frac{p_1}{p_s} - \frac{\gamma-1}{\gamma+1} = 0 .$$ (5.20)

Multiplying Eqns. (5.19) and (5.20) together and using (5.17) to eliminate the relative particle velocity terms, one arrives at

$$\left(\frac{p_o}{p_s} + \frac{\gamma-1}{\gamma+1}\right)\left(\frac{p_1}{p_s} + \frac{\gamma-1}{\gamma+1}\right) - \left(\frac{2\gamma}{\gamma+1}\right)^2 = 0 .$$ (5.21)

This equation forms the basis for the discussion in the next section.

5.2.3 Discussion: On the 1D fluid-structure interaction model by FD

There are three important and related issues in the fluid-structure interaction model of FD that can now be discussed below:

(1) The net pressure acting on the front face of the sandwich beam (see Eq. 15 of FD) was proposed to be the superposition of the incoming and reflected blast wave pulses. In general, this is acceptable for the *weak* shock (or sound) waves generated in underwater explosions because water is nearly incompressible. However, by using the results of the *weak* shock analysis to estimate typical impulses delivered to the front face of the sandwich beam by *strong* shock waves, say, in air blasts (see pages 389 and 397 of FD), FD imply that their modified Taylor's model (1963a) is also applicable to *non-linear*, finite amplitude disturbances propagating in a compressible medium (air). The author does not agree that linear superposition of the shock wave pulse is applicable in air blasts.

(2) FD proposed that full transmission of the blast impulse to the sandwich beam, assuming a stationary rigid face sheet, be considered for air blast loadings. This allows *safe* design charts to be constructed. The point in question is FD's assumption that the limiting (maximum) impulse transmitted is identical to that of a *weak* shock in water, where the reflected peak overpressure is twice the incident overpressure, given by

$$I = \int_0^\infty 2p_o e^{-t/\theta} dt = 2p_o\theta \tag{5.22}$$

where p_o is the overpressure and θ the decay constant of the pressure pulse (exponentially-decaying). By contrast, Eqn. (5.21) shows that for a *strong* shock ($p_s \gg p_o$) where $p_o/p_s \to 0$, $p_1/p_s \to 8$, i.e. the reflected overpressure can be up to 8 times that of the incident overpressure in an ideal gas. This gives a limiting impulse of $8p_o\theta$ by momentum considerations; a classical result well-known to fluid mechanicists (Taylor, 1963b; Baker, 1973; Billingham and King, 2000). Hence, the limiting impulse transmitted in an air blast can be a factor of four (4) greater than that considered by FD. The actual reflected overpressure could reach a factor of 20, or even higher, if real gas effects, such as dissociation and ionisation of the air molecules, are taken into consideration (Baker, 1973). In general, the relationship

124
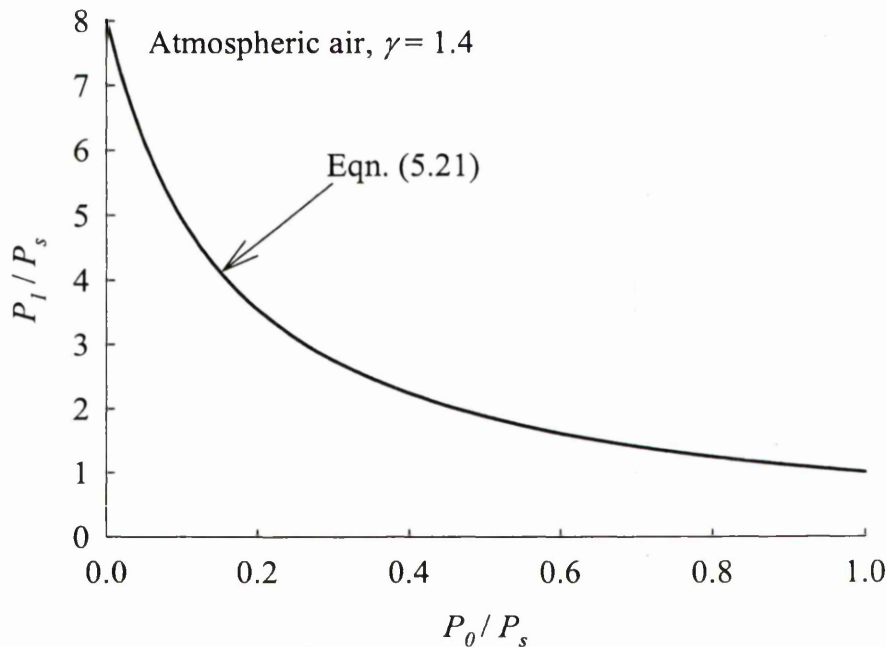
Figure 5.3 – Pressure change due to the reflection of a shock incident normally on a solid wall in air, assuming $\gamma = 1.4$. The pressures on either side of the shock before and after reflection are depicted in Fig. 5.2.

between the ratio of the reflected overpressure to the initial overpressure (p_1/p_s) is a function of the ratio of ambient gas pressure to the initial overpressure (p_o/p_s), as shown in Fig. 5.3. Therefore, it is questionable whether the performance charts constructed by FD, based on the assumption that the reflected overpressure in air is only twice the incident, are a sufficiently safe guide for the design of *air-blast* resistant sandwich beams. This point was recently raised in a discussion paper by Tan et al. (2005). In response, Fleck and Deshpande (2005) have noted that their analysis can handle strong air shocks provided one takes the transmitted impulse as an input to the model. This is undoubtedly correct, but the point in question is not on the approach rather the magnitude of the impulse felt by the sandwich beam after the shock is reflected from the front face sheet and its consequences.

(3) Following an explosion in air, a relatively compact volume of high energy gases

is generated. The outward expansion of these gases produces a pressure (or shock) wave that travels at a supersonic speed which depends on the size of the charge used (see experimental data of Swisdak, 1975). The velocity of the shock is normally greater than $330ms^{-1}$, the speed of sound in air at $0^{\circ}C$, used by FD (Page 389 of FD). Since no explicit Hopkinson scaling law (Baker, 1973) exists that could be used to estimate the speed of the shock, an alternative example is provided here. Consider a long cylinder filled with a perfect gas and closed at the left-end by a plane, rigid piston as shown in Fig. 5.4.[5] The gas is initially everywhere at rest with density ρ_o and pressure p_o. Assuming that no heat is supplied to the gas and that a steady shock is fully formed due to the piston advancing at constant velocity V_p. Using Eqns. (5.1) to (5.3), one obtains the following relations:
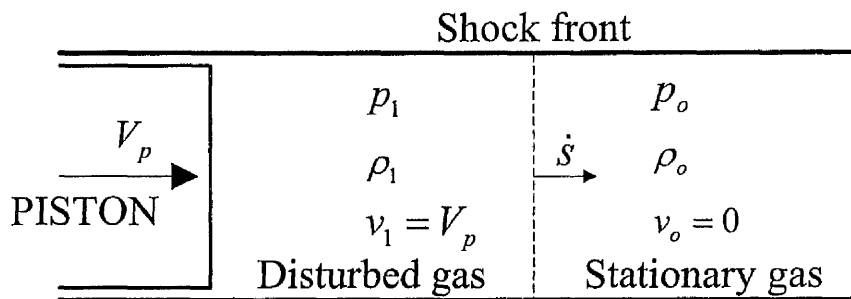
Figure 5.4 – The various quantities on either side of the shock front cause by an advancing piston.

$$\rho_1\left(\dot{s}-V_p\right)=\rho_o\dot{s} \tag{5.23}$$

$$p_o-p_1=-\rho_o V_p\dot{s} \tag{5.24}$$

$$\frac{1}{2}\dot{s}^2+\frac{\gamma}{\gamma-1}\left(\frac{p_o}{\rho_o}\right)=\frac{1}{2}\left(\dot{s}-V_p\right)^2+\frac{\gamma}{\gamma-1}\left(\frac{p_1}{\rho_1}\right) \tag{5.25}$$

where the notations have the same meaning as in previous sections. Defining the

---

[5] This is a tutorial problem the author encountered as an undergraduate at the National University of Singapore in a third-year fluid mechanics course delivered by Prof. T.S. Lee.

parameters $\alpha \equiv \dot{s}/V_p$ and $M \equiv V_p/c$ (where M is the Mach number and c is the local sound speed given in Eqn. 5.8), Eqns. (5.23) and (5.24) can be expressed as

$$\frac{\rho_1}{\rho_o} = 1 + \frac{1}{\alpha - 1} \quad \text{and} \tag{5.26}$$

$$\frac{p_1}{p_o} = 1 + \alpha \gamma M^2 \tag{5.27}$$

for which it is possible to calculate ρ_1 and p_1 once $\dot{s}$ is known. Substitute Eqns. (5.26) and (5.27) into (5.28) and simplify gives

$$2M^2 \alpha^2 - (1 + \gamma)M^2 \alpha - 2 = 0 \tag{5.28}$$

which has a positive root given by

$$\alpha = \frac{1}{4}(1 + \gamma) + \sqrt{\frac{1}{16}(1 + \gamma)^2 + \frac{1}{M^2}} . \tag{5.29}$$

Therefore, the speed of the shock is

$$\dot{s} = \frac{1}{4}(1 + \gamma)V_p + \sqrt{\frac{1}{16}V_p^2(1 + \gamma)^2 + c^2} \tag{5.30}$$

The above results show that as $M \to 0$, $\dot{s} \to c$, $\rho_1 \to \rho_o$ and $p_1 \to p_o$. When $V_p \ll c$ the shock wave is, therefore, weak in the sense that $[p] \ll p_o$ and $[\rho] \ll \rho_o$. The speed c to which $\dot{s}$ approximates is the speed of sound in the undisturbed gas. Thus because FD assumes that the pressure pulse travels at the speed of sound in air ($330 ms^{-1}$), their analysis can only applies to weak shocks and not to strong air shocks.

5.3 Application of the 'steady-shock' theory to the high velocity compression of metal foams in existing literature

In this section, detailed comments are given on the application of the 'steady-shock' theory to metal foams in recent literature which is inconsistent with the one presented in Chapter 4. The plastic shock wave analysis by Fleck and Deshpande (2004) is discussed first.

5.3.1 The plastic shock wave analysis of Fleck and Deshpande (2004)

In the analysis of the core compression phase (see Fig. 5.5), a global energy balance of the sandwich beam was given by FD to be (Eqn. 28 in FD)

$$\underbrace{\frac{1}{2}m_f v_o^2}_{\substack{\text{Initial kinetic energy} \\ \text{of front face-sheet}}} = \underbrace{\frac{1}{2}\left[m_f + \rho_c(c - X)\right]v_u^2}_{\substack{\text{Kinetic energy of foam in front} \\ \text{of shock and back face-sheet}}} + \underbrace{\frac{1}{2}\left[m_f + \rho_c X\right]v_d^2}_{\substack{\text{Kinetic energy of foam} \\ \text{behind shock and front face-sheet}}} + \underbrace{\sigma_{nY}\varepsilon_D X}_{\text{Energy absorbed by the foam}}$$

$$(5.31)$$

where the symbols used by FD also apply here. For a thermodynamic system, the first law asserts that, for any possible process, (Ericksen, 1991)

$$\frac{dE}{dt} = P + Q \tag{5.32}$$

where E is the energy (kinetic plus internal) of the system, P is the power (rate at which work is done on the system) and Q is the rate at which heat is supplied to the system. Because no heat or external power is supplied to the sandwich beam throughout Stage II (defined as the core compression phase by FD), it is reasonable to assume that core compression occurs within an isolated system. Hence, $P = Q = 0$ and Eqn. (5.32) gives
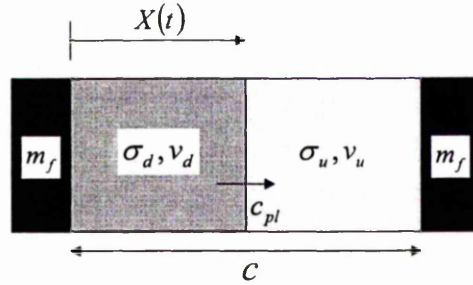
Figure 5.5 – Sketch of the propagation of a 1D shock in the sandwich core (reprinted from Fleck and Deshpande, 2004)

$$E = \text{constant} . \tag{5.33}$$

In other words, the jumps in the kinetic and internal energies per unit mass across the shock front are equal. Two issues/questions arise from Eqn. (5.31) as follows:

(i) That the energy absorbed per unit volume of core material ($\sigma_{nY}\varepsilon_D$) is independent of the initial front face velocity v_o. This is not consistent with the studies reported in Radford et al. (2005) and Deshpande and Fleck (2005), nor with the experimental data presented in Chapter 3.

(ii) That the change in the internal energy density of the core material $[\rho_c U]$ ($=\sigma_{nY}\varepsilon_D$ by FD) is independent of the particle velocity jump across the shock front, where $[\ ] \equiv (\ )_d - (\ )_u$ and U is the internal energy per unit mass. By contrast, the Rankine-Hugoniot relations predict (from Eqns. (4.26) and (4.37))

$$[\rho_c U] = \sigma_u[\varepsilon] + \rho_c[v]^2/2 . \tag{5.34}$$

As previously discussed in Section 4.4.2, the prediction by Eqn. (5.34) agrees well with the results of the numerical simulations. Since $[v] \approx v_o$, the curves in Figure 4.18 shows that the $[\rho_c U]$ is *dependent* upon $[v]$ at every stage of the compression

process. Therefore, it is questionable whether energy conservation is achieved in Eqn. (5.31). It is explained later that the identifier 'ALLIE' (abscissa of Fig. 4.18) gives the internal energy density of the core material.

The two anomalies above were highlighted in a Discussion by Tan et al. (2005). In response, Fleck and Deshpande (2005) have argued that a major component of the internal work in the FE simulations of Section 4.4.2 is probably due to the artificial viscosity inherent in the explicit simulations using ABAQUS. They show that by equating the change in internal energy in our FE calculations to the degree of axial stretch of the cell walls of the foam, in the extreme case of all the cell walls sharing equally this energy change, each cell wall will then need to undergo a nominal compressive strain of 0.99 in the case where $v_o = 200ms^{-1}$ which they conclude is physically unrealistic.

The author agrees with Fleck and Deshpande (2005) that ABAQUS Explicit does, indeed, introduce a linear bulk viscosity term[6] whose purpose is to improve the modelling of high-speed dynamic events. A brief review of how ABAQUS partitions the different energy terms in the energy balance equation is required to clarify FD's response. In ABAQUS, energy balance is expressed as (ABAQUS, 2002)

$$E_U + E_k + E_F - E_W = \text{constant} \qquad (5.35)$$

where E_k ($\equiv \int_V \frac{1}{2}\rho v.v dV$) is the kinetic energy, E_F is the energy dissipated by contact friction forces between contact surfaces, E_W is the rate of work done to the body by external forces and E_U is the internal energy which ABAQUS further divides into two separate contributions as follows (ABAQUS, 2002):

---

[6] Note that no quadratic bulk viscosity term is introduced because it only applies to solid continuum elements (ABAQUS, 2002). A general-purpose shell element (S4R) is used here in the FE model (see Section 4.4.2).

$$E_U = \int_0^t \left(\int_V \boldsymbol{\sigma}^c : \dot{\boldsymbol{\varepsilon}}\, dV \right) dt + \int_0^t \left(\int_V \boldsymbol{\sigma}^d : \dot{\boldsymbol{\varepsilon}}\, dV \right) dt \qquad (5.36)$$

$$\underbrace{\phantom{\int_0^t \left(\int_V \boldsymbol{\sigma}^c : \dot{\boldsymbol{\varepsilon}}\, dV \right) dt}}_{\text{Remaining energy}} \quad \underbrace{\phantom{\int_0^t \left(\int_V \boldsymbol{\sigma}^d : \dot{\boldsymbol{\varepsilon}}\, dV \right) dt}}_{\text{Energy dissipated by viscous effects}}$$

where $\boldsymbol{\sigma}^c$ is the stress derived from user-specified constitutive equation and $\boldsymbol{\sigma}^d$ is the viscous stress (defined for <u>bulk viscosity</u>, material damping and dashpots). Note that ABAQUS continues to call the remaining energy the internal energy. Using the strain decomposition $\dot{\boldsymbol{\varepsilon}} = \dot{\boldsymbol{\varepsilon}}^{el} + \dot{\boldsymbol{\varepsilon}}^{pl} + \dot{\boldsymbol{\varepsilon}}^{cr}$ (where $\dot{\boldsymbol{\varepsilon}}^{el}$, $\dot{\boldsymbol{\varepsilon}}^{pl}$ and $\dot{\boldsymbol{\varepsilon}}^{cr}$ are elastic, plastic and creep strain rates, respectively), ABAQUS further distinguishes the various contributions to the 'remaining energy' in Eqn. (5.36) as follows:

$$\underbrace{\int_0^t \left(\int_V \boldsymbol{\sigma}^c : \dot{\boldsymbol{\varepsilon}}\, dV \right) dt}_{\text{Remaining energy}} = \underbrace{\int_0^t \left(\int_V \boldsymbol{\sigma}^c : \dot{\boldsymbol{\varepsilon}}^{el}\, dV \right) dt}_{\text{Elastic strain energy}} + \underbrace{\int_0^t \left(\int_V \boldsymbol{\sigma}^c : \dot{\boldsymbol{\varepsilon}}^{pl}\, dV \right) dt}_{\text{Energy dissipated by plasticity}}$$

$$+ \underbrace{\int_0^t \left(\int_V \boldsymbol{\sigma}^c : \dot{\boldsymbol{\varepsilon}}^{cr}\, dV \right) dt}_{\substack{\text{Energy disipated by time dependent deformation} \\ \text{such as creep, swecling and viscoelasticity.}}}$$

$$(5.37)$$

Note that the energy dissipated through bulk viscosity is not part of the 'remaining energy'; rather, it is separately classified as the energy dissipated by viscous effects. The energy identifier ALLIE (see ABAQUS, 2002) is the sum of the 'remaining energy' (Eqn. 5.37) and three other energy terms not applicable to the simulations in Section 4.4.2. Since the last term in Eqn. (5.37) is zero, the abscissa of Fig. 4.18 gives the sum of the elastic strain energy and the energy dissipated by plasticity in the FE model. Figure 5.6 gives the variation of the different energies with time during the in-plane compression of a regular honeycomb ($\Lambda = 1$) at $200 ms^{-1}$ - the results shown are for the same numerical example given in Section 4.4.2. The figure shows that the energy dissipated by viscous effects is less than 5% of the energy dissipated through rate-independent plastic deformation (ALLPD in ABAQUS). It also shows that ALLIE $\cong$ ALLPD which suggest that the contributions from the elastic strain energy is small and, therefore, negligible. Hence, the author disagrees with the response of Fleck and Deshpande (2005).

131
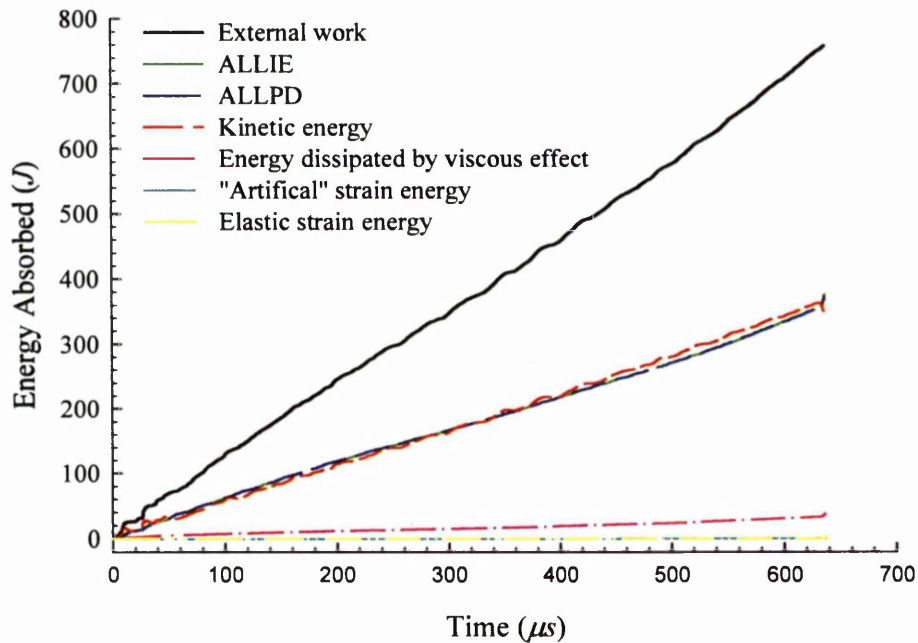
Figure 5.6 – Variation of the energies absorbed with time during the in-plane compression of a regular honeycomb ($\Lambda = 1$) at $200ms^{-1}$.

The author agrees, in principal, however with Fleck and Deshpande (2005) that the magnitude of the principal strain components in the cell walls must be checked. This is carried out for the FE model which shows that the maximum principal strains in the cell walls never exceed 0.55 for the case of $v_o = 200ms^{-1}$ and is considerably lower than the value of 0.99 estimated by Fleck and Deshpande (2005). It is the opinion of the author that this level of straining is not physically unrealistic.

5.3.2 Application of the 'shock' theory to metal foams by Ashby et al. (2000) and Lu and Yu (2003)

In a similar vein, consider the case of a one-dimensional end-on impact of a long stationary bar of foam of cross sectional area A by a rigid mass M travelling at an impact velocity V_o (see Figure 5.6a). This case was previously analysed by Ashby et al. (2000) and Lu and Yu (2003). An idealised compressive stress-strain curve shown

132

in Figure 5.6b was adopted. Their analysis assumes zero particle velocity ahead of the 'shock' and an upstream stress equal to σ_{pl}^{qs}. A global energy balance of the foam energy absorber was given as

$$\frac{1}{2}\left(M + \frac{\rho_o Al}{1-\varepsilon_D}\right)\bar{v}^2 + \sigma_{pl}^{qs}\varepsilon_D \frac{Al}{1-\varepsilon_D} = \frac{1}{2}M_b V_o^2 \ , \qquad (5.38)$$

where l is the current location of the 'shock' front measured from the impact end.


(a)

(b)
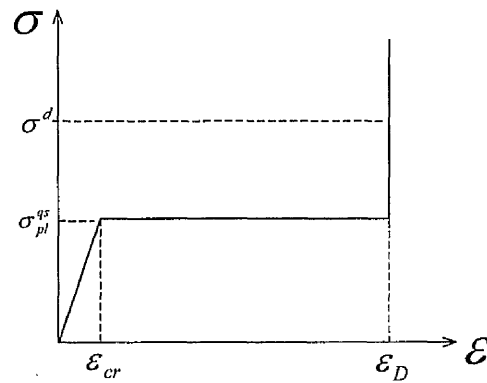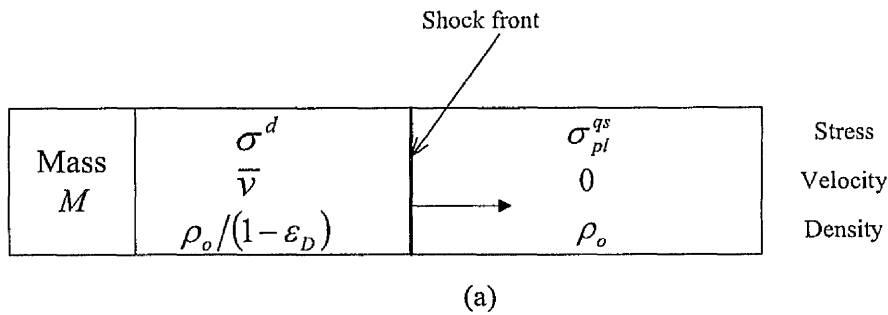
Figure 5.6 – (a) The stress, velocity on either side of the 'shock' wave front for an impacted foam by a mass M and (b) Schematic compressive stress-strain curve for a metal foam.

By comparing terms with Eqn. (4.40), they assert implicitly that the change in internal energy per unit reference area of the bar is

$$(E_U)_2 - (E_U)_1 = \sigma_{pl}^{qs}\varepsilon_D l/(1 - \varepsilon_D). \tag{5.39}$$

Assuming that Eqn. (5.39) is correct, multiplying Eqn. (4.37) with l, and writing $[\rho_o U]l = \sigma_{pl}^{qs}\varepsilon_D l/(1 - \varepsilon_D)$, gives

$$\sigma_{pl}^{qs}\varepsilon_D l/(1 - \varepsilon_D) - (\sigma^d + \sigma_{pl}^{qs})\varepsilon_D l/2 \neq 0, \tag{5.40}$$

a contradiction. Thus, by this simple argument, the assertion in Eqn. (5.39) cannot be correct; otherwise, the energy flux is not continuous across the 'shock'. Consequently, Eqn. (5.38) does not account in full for the balance of energy. The correct equation of motion for this case is presented in Section 4.3.3.

6.4 Conclusion

Anomalies between the 'steady-shock' theory presented in Chapter 4 and those in recent literature have been discussed by examples and by results of FE simulations of 2D Voronoi honeycombs. It is hoped that the apparently incorrect treatment of the energy absorbed by metal foams when subjected to impact loading have thereby been clarified.

Chapter 6

Conclusions and further research

6.1 Conclusions

6.1.1 Experimental method for high strain rate testing of metal foams

The performances of two common high strain rate testing methods, viz. the SHPB and direct-impact techniques, were examined critically in the context of testing cellular materials. Important issues in sample design, such as the sizing of the test specimens in relation to how specimen size, relative to the cell size, affects the mechanical properties of metal foams, were discussed. The localised nature of cell deformation in metal foams was demonstrated in impact tests for a broad range of loading rates in Chapter 3. A possible violation of the uniform deformation assumption during the SHPB testing of metal foams is revealed. The present study recommends the direct-impact technique for the high rate testing of metal foams.

6.1.2 Consistent method to extract key material properties

A consistent method, based on the efficiency of metal foams in absorbing energy, has been proposed to extract key material properties, viz. the plastic collapse and plateau stresses, and the strain at which densification occurs, from nominal stress-strain curves and dynamic force pulses. The method also provides a consistent framework for defining key material parameters in other cellular materials in the current literature.

6.1.3 Quasi-static and dynamic properties of Cymat and Duocel foams

The mechanical properties of the Cymat and Duocel foams have been measured

135

and their dynamic response to a wide range of loading rates is broadly classified according to velocity régimes, viz. sub and super-critical velocities. At sub-critical velocities, test samples deform by cumulative multiplication of discrete crush bands. Cell size effects and morphological defects continue to affect (knock-down) the mechanical properties measured. At super-critical velocities, samples deform by progressive cell crushing from its impact end where a different inertial phenomenon, namely 'shock' wave propagation, is responsible for the enhancement of the mechanical properties measured.

The transition from a discrete band multiplication to a 'shock-type' deformation was measured to occur at impact velocities of approximately $100ms^{-1}$ (*small* cell Cymat), $50ms^{-1}$ (*large* cell Cymat), $110ms^{-1}$ (*10L* & *40L* Duocel) and $90ms^{-1}$ (*10T* Duocel) and this agrees well with the theoretical predictions of $108ms^{-1}$, $42ms^{-1}$, $116ms^{-1}$ and $85ms^{-1}$, respectively.

Significant enhancement of the plastic collapse stress is measured in the sub-critical velocity régime for both foams. Translational and, to a lesser extent, rotational inertia of the cell walls, rather than 'shock' propagation, are responsible for the strength enhancement. They introduce an initial phase to the deformation, which is dominated by plastic axial compression of the cell walls. The linear variation of the plastic collapse strength data with impact velocity and the good agreement with the predictions of a one-dimensional plastic wave theory support the influence of Type-II microinertia effects. In the super-critical velocity régime, the data for the plastic collapse stresses varies with the square of impact velocity which is consistent with 'shock' propagation.

The plateau strength data is insensitive to the impact velocity in the sub-critical régime for both foams. Significant enhancement of the plateau stress is observed in the super-critical velocity régime where 'shock' propagation effects are important. The reason behind the lower plateau strength compared to its corresponding quasi-static value at the lower impact velocities remains to be clarified.

A direct correlation between the dynamic mechanical properties and the nominal engineering strain rate of metal foams was shown to be unviable and the reasons for the conflicting conclusions in the current literature have been clarified.

6.1.4 One-dimensional plastic wave and 'steady-shock' models, and numerical simulations of 2D Voronoi honeycombs

The one-dimensional plastic wave and 'steady-shock' models presented in Chapters 3 and 4, respectively, brings together the following features:

1. prediction of the plastic collapse stress in the sub-critical and super-critical velocity regimes.

2. prediction of the full dynamic force-time pulse and the dynamic plateau stress for proximal and distal end impacts

3. established the kinematic existence condition for continuing 'shock' propagation

4. prediction of the impact velocity for transition to a 'shock-type' deformation.

5. estimation of the additional plastic strain energy absorbed per unit volume of material associated with microinertia effects.

Both models successfully reproduce the measured strength properties qualitatively in their respective velocity régimes. At sub-critical impact velocities, the 'shock' model consistently underestimates the plastic collapse stress due to microinertia effects and the plastic wave model must be used instead. The over-estimation of the plastic collapse stress at super-critical impact velocities is due to the effect of the locking assumption at the densification strain in the 'shock' model. It is possible to rectify this deficiency by relaxing the locking assumption, for example by allowing the strain behind the 'shock' front to vary with the dynamic stress. In general, the predictions of the plateau strength by the 'shock' model are consistently overestimated; again, a consequence of the locking material assumption. But the quadratic trend has been reproduced qualitatively.

The numerical simulations of 2D Voronoi honeycombs subjected to super-critical velocity compression show an increase in energy absorption which can be attributed directly to rate-independent plastic deformation in their cell edges caused by the dynamic localisation of crushing. The 'shock' model gives an accurate prediction of the increased energy absorbed by the honeycomb.

6.2 Further research

There are numerous aspects of the dynamic mechanical properties of metal foams that would benefit from further investigations of which the following arises from the present study:

1. Using a more realistic constitutive relation with the 'steady-shock' model, such as by relaxing the rigid locking assumption at the densification strain, to give a better prediction of the plastic collapse and plateau stresses.

2. For high-velocity impact experiments, the results can be interpreted in terms of the Rankine-Hugoniot theory of shock propagation. The profiles of these high amplitude waves are satisfactorily approximated as shocks because the actual wave thickness is small (of the order of one cell-width) compared to the propagation distances of interest. For experiments performed at pressures only moderately in excess of the static threshold, the waveforms are only crudely approximated as shocks because of the large amount of dispersion present. Whilst it is easy to conceive a number of effects that would contribute to the observed dispersion, it seems probable that the most influential is the lag experienced by the material in coming to equilibrium under dynamic loading because of the time required for cell collapse. This dispersive effect is counteracted by the tendency of the propagating waves to evolve towards shock due to the rapidly decreasing compressibility of the material as it is being compacted. The observed wave thickness is a balance struck between these two conflicting tendencies and an investigation into the structure of the 'shock' wave which forms at the moderate impact-velocities is important.

3. A new 'wave' theory is required for the sub-critical velocity compression of metal foams. It must recognise and incorporate the effects produced by the presence of the saddle transition phase in the representation of the stress-strain curve. This will undoubtedly require the application of a regularised continuum theory involving higher order displacement gradients and introducing length scales characteristic of the cellular geometry, or other non local approaches.

4. The present study has emphasized the concept of the Hugoniot equation of state, i.e. one which describes the thermodynamic states attainable through a steady shock wave. Analytical procedures must be developed to treat unsteady wave propagation in metal foams.

5. A 2D Voronoi honeycomb structure is being used increasingly to shed light on the mechanics of the much more complex 3D foams in the current literature. However, it not entirely clear whether a connection exists between Voronoi diagrams in E^2 and convex polyhedra in E^3. If so, how are they related? An investigation of this type will undoubtedly require some background knowledge on computational geometry.

References

ABAQUS Theory Manual, Version 6.3, 2002. HKS Inc., Providence, Rhode Island.

Arfken, G.B., Weber, H.J., 1995. *Mathematical methods for physicist*, 4th edn., Academic Press Inc., California.

Ashby, M.F., Evans, A.G., Fleck, N.A., Gibson, L.J., Hutchinson, J.W., Wadley, H.N.G., 2000. *Metal Foams: A Design Guide*, Butterworth Heinemann, Oxford.

Bacon, C., 1998. An experimental method for considering dispersion and attenuation in a viscoelastic Hopkinson bar, *Exp. Mech.* 38, 242 – 249.

Bacon, C., 1999. Separation of waves propagating in an elastic or viscoelastic Hopkinson pressure bar with three-dimensional effects, *Int. J. Impact Engng.* 22, 55 – 69.

Baker, W.E., 1973. *Explosions in Air*, University of Texas Press, Austin and London.

Bastawros, A.F., Bart-Smith, H., Evans, A.G., 2000. Experimental analysis of deformation mechanisms in a closed-cell aluminum alloy foam, *J. Mech. Phys. Solids* 48, 301 – 322.

Billingham, J. and King, A.C., 2000. *Wave motion*, Cambridge University Press, Cambridge.

Bland, D.R., 1988. *Wave theory and applications*, Oxford University Press, Oxford.

Brillouin, L., 1946. *Wave motion in periodic structures*, McGraw-Hill, New York.

Calladine, C.R., English, R.W., 1984. Strain-rate and inertia effects in the collapse of two types of energy-absorbing structure, *Int. J. Mech. Sci.* 26, 689 – 701.

Chadwick, P., 1976. *Continuum mechanics: Concise theory and problems*, Dover Publications, New York.

Chastel, Y., Hudry, E., Forest, S., Peytour, C., 1999. Mechanical behaviour of aluminium foams for various deformation paths. Experiment and modelling, In: Banhart, J., Ashby, M.F., Fleck, N.A. (Eds.), *Cellular metals and metal foaming technology*, Verlag MIT Publishing, Bremen (Germany), 263 – 268.

Chen, C., Lu, T.J., Fleck, N.A., 1999. Effect of imperfections on the yielding of two dimensional foams, *J. Mech. Phys. Solids* 47, 2235 – 2272.

Dannemann, K.A., Lankford, J., 2000. High strain rate compression of closed-cell aluminium foams, *Mat. Sci. Eng.* A293, 157 – 164.

Davies, E.D.H., Hunter, S.C., 1963. The dynamic compression testing of solids by the method of the split Hopkinson pressure bar (SHPB), *J. Mech. Phys. Solids* 11, 155 – 179.

Deshpande, V.S., Fleck, N.A., 2000. High strain rate compressive behaviour of aluminium alloy foams. *Int. J. Impact Engng.* 24, 277 – 298.

Deshpande, V.S., Fleck, N.A., 2005. One-dimensional response of sandwich plates to underwater shock loading, *J. Mech. Phys. Solids* 53, 247 – 2383.

Ericksen, J.L., 1991. *Introduction to the thermodynamics of solids*, Chapman and Hall, London.

Eringen, A.C., Şuhubi, E.S., 1974. *Elastodynamics. Vol 1 – Finite Motions*, Academic Press, New York.

Fleck, N.A., Deshpande, V.S., 2004. The resistance of clamped sandwich beams to shock loading, *ASME J Appl. Mech.* 71, 386 – 401.

Fleck, N.A., Deshpande, V.S., 2005. Closure to "Discussion of 'The resistance of clamped sandwich beams to shock loading" (2005, ASME J. Appl. Mech., 72, pp.978 – 979), *ASME J Appl. Mech.* 72, 980.

Gibson, L.J., Ashby, M.F., 1997. *Cellular Solids: structure and properties*, 2nd edn., Cambridge University Press, Cambridge.

Gorham, D.A., Pope, P.H., Field, J.E., 1992. An improved method for compressive stress-strain measurements at very high strain rates, *Proc. R. Soc. Lond.* A438, 153 – 170.

Hall, I.W., Guden, M., Yu, C.J., 2000. Crushing of aluminium closed cell foams: density and strain rate effects. *Scripta Mater.* 43, 515 – 521.

Hanssen, A.G., 2000. *Structural crashworthiness of aluminium foam-based components,* Ph.D. Thesis, Norwegian University of Science and Technology, Trondheim, Norway.

Hanssen, A.G., Hopperstad, O.S., Langseth, M., Ilstad, H., 2002. Validation of constitutive models applicable to aluminium foams, *Int. J. Mech. Sci.* 44, 359 – 406.

Harrigan, J.J., Peng, C., Reid, S.R., 1998a. Inertia effects in impact energy absorbing materials and structures, In: Langseth, M., Krauthammer, T. (Eds.), *Transient loading and response of structures*, International Symposium in honour of Arnfinn Jenssen, Trondheim, Norway, 447 – 474.

Harrigan, J.J., Reid, S.R., Peng, C., 1999. Inertia effects in impact energy absorbing materials and structures. *Int. J. Impact Engng.* 22, 955 – 979.

Harrigan, J.J., Reid, S.R., Reddy, T.Y., 1998b. Inertial forces on the crushing of wood loaded along the grain, In: Allison, I.M. (Ed.), *Experimental Mechanics*, Balkema, Rotterdam, 193 – 198.

Harrigan, J.J., Reid, S.R., Reddy, T.Y., 1998c. Accurate measurement of impact force pulses in deforming structural components, *ibid*, 149 – 154.

Harrigan, J.J., Reid, S.R., Tan, P.J., Reddy, T.Y., 2005. High rate crushing of wood along the grain, *Int. J. Mech. Sci.* 47, 521 – 544.

Harte, A.M., Nichol, S., 2001. Scale-up issues related to producing Cymat stabilised aluminium foam, In: Banhart, J., Ashby, M.F., Fleck, N.A. (Eds.), *Cellular metals and metal foaming technology*, Verlag MIT Publishing, Bremen (Germany), 49 – 54.

Hönig, A., Stronge, W.J., 2002a. In-plane dynamic crushing of honeycomb – Part I: Crush band initiation and wave trapping. *Int. J. Mech. Sci.* 44, 1665 – 1696.

Hönig, A., Stronge, W.J., 2002b. In-plane dynamic crushing of honeycomb – Part II: application to impact, *ibid*, 1697 – 1714.

Hopkins, H.G., 1968. The method of characteristics and its application to the theory of stress waves in solids, In: Heyman, J., Leckie, F.A. (Eds.), *Engineering Plasticity*, Cambridge University Press, Cambridge, 277 – 315.

Inoue, H., Harrigan, J.J., Reid, S.R., 2001. A review on inverse analysis for indirect measurement of impact force, *ASME Appl. Mech. Rev.* 54, 503 – 524.

Inoue, H., Kamibayashi, M., Kishimoto, K., Shibuya, T., Koizumi, T., 1992. Numerical Laplace transformation and inversion using fast Fourier transformation, *JSME Int. J.* 35, 319 – 324.

Karagiozova, D., Jones, N., 1995. A note on the inertia and strain-rate effects in the Tam and Calladine model, *Int. J. Impact Engng.* 16, 637-649.

Kenny, L.D., 1996. Mechanical properties of particle stabilised aluminium foam. *Mat. Sci. Forum* 217-222, 1883 – 1890.

Lankford, J., Dannemann, K.A., 1998. Strain rate effects in porous materials. In: *Porous and Cellular Materials for Structural Applications*, Materials Research Society, Pittsburgh, P.A., 103 – 108.

Lee, S., Barthelat, F., Moldovan, N., Espinosa, H.D., Wadley, H.N.G., 2005. Deformation rate effects on failure modes of open-cell Al foams and textile cellular materials. *Int. J. Solids Structs.*, in press.

Lighthill, M.J., 1956. Viscosity effects in sound waves of finite amplitude, In: Batchelor, G.K., Davies, R.M. (Eds.), *Surveys in Mechanics*, Cambridge University Press, Cambridge, 250 – 351.

Lu, G., Yu, T.X., 2003. *Energy absorption of structures and materials*, Woodhead Publishing Ltd., Cambridge, UK.

Miyoshi, T., Mukai, T., Higashi, K., 2002. Energy absorption in closed-cell Al-Zn-Mg-Ca-Ti foam, *Materials Transactions* 43 (7), 1778 – 1781.

Montanini, R., 2005. Measurement of strain rate sensitivity of aluminium foams for energy dissipation. *Int. J. Mech. Sci.* 47, 26 – 42.

Moran, P.M., Liu, X.H., Shih, C.F., 1995. Kink band formation and band broadening in fibre composites under compressive loading, *Acta Metall. Mater.* 47, 2943 – 2958.

Morland, L.W., 1959. The propagation of plane irrotational stress waves through an

elastoplastic medium, *Phil. Trans. R. Soc. Lond.* A251, 341 – 383.

Mukai, T., Kanahashi, H., Higashi, K., Yamada, Y., Shimojima, K., Mabuchi, M., Miyoshi, T., Nieh, T.G., 1999a. Energy absorption of light-weight metallic foams under dynamic loading. In: Banhart, J., Ashby, M.F., Fleck, N.A. (Eds.), *Cellular metals and metal foaming technology*, Verlag MIT Publishing, Bremen (Germany), 353 – 358.

Mukai, T., Kanahashi, H., Miyoshi, T., Mabuchi, M., Nieh, T.G., Kigashi, K., 1999b. Experimental study of energy absorption in a close-celled aluminum foam under dynamic loading. *Scripta Mater.* 40, 921 – 927.

Onck, P., Andrews, E.W., Gibson, L.J, 2001. Size effects in ductile cellular solids. Part I: modelling, *Int. J. Mech. Sci.* 43, 681 – 699.

Papka, S.D., Kyriakides, S., 1994. In-plane compressive response and crushing of honeycomb. *J. Mech. Phys. Solids* 42, 1499 – 1532.

Paul, A., Ramamurty, U., 2000. Strain rate sensitivity of a closed-cell aluminium foam. *Mat. Sci. Eng.* A281, 1 – 7.

Poulsen, J.S., Moran, P.M., Shih, C.F., Byskov, E., 1997. Kink band initiation and band propagation in clear wood under compressive loading, *Mech. Mater.* 25, 67 – 77.

Radford, D.D., Deshpande, V.S., Fleck, N.A., 2005. The use of metal foam projectiles to simulate shock loading on a structure. *Int. J. Impact Engng.* 31, 1152 – 1171.

Reddy, T.Y., Reid, S.R., Barr, W.W., 1991. Experimental investigation of inertia effects in one-dimensional metal ring systems subjected to end impact – II: Free ended systems, *Int. J. Impact Engng.* 11, 463 – 480.

Reid, S.R., Bell, W.W., 1984. Response of 1-D metal ring systems to end impact, In: Harding, J. (Ed.), *Mechanical Properties at High Rates of Strain*. Institute of Physics Conference Series No. 70, Oxford, 471 – 478.

Reid, S.R., Bell, W.W., Barr, R.A., 1983. Structural plastic shock model for one-dimensional ring system, *Int. J. Impact Engng.* 1, 175 – 191.

Reid, S.R., Peng, C., 1997. Dynamic uniaxial crushing of wood, *Int. J. Impact Engng.* 19, 531 – 570.

Reid, S.R., Reddy, T.Y, Peng, C., 1993. Dynamic compression of cellular structures and materials, In: Jones, N., Wierzbicki, T. (Eds.), *Structural Crashworthiness and Failure*, Elsevier Applied Science Publishers, 295 – 340.

Ruan, D., Lu, G., Chen, F.L., Siores, E., 2002. Compressive behaviour of aluminium foams at low and medium strain rates. *Comp. Structs.* 57, 331 – 336.

Ruan, D., Lu, G., Wang, B., Yu, T.X., 2003. In-plane dynamic crushing of honeycombs – a finite element study. *Int. J. Impact Engng.* 28, 161 – 182.

Shim, V.P.W., Tay, B.Y., Stronge, W.J., 1990. Dynamic crushing of strain softening cellular structures – a one-dimensional analysis, *Trans. ASME J. Engng. Mater. Tech.* 112, 398 – 405.

Silva, M.J., Hayes, W.C., Gibson, L.J., 1995. The effect of non-periodic microstructure on the elastic properties of two-dimensional cellular solids. *Int. J. Mech. Sci.* 37, 1161 – 1177.

Su, X.Y., Yu, T.X., Reid, S.R., 1995. Inertia-sensitive impact energy absorbing structures, Part I: Effects of inertia and elasticity, *Int. J. Impact Engng.* 16, 651 – 672.

Swisdak, M.M., 1975. *Explosion effects and properties: Part I – Explosion effects in air*, Technical report, Naval Surface Weapons Centre, White oak, Silver spring, MD.

Tan, P.J., Reid, S.R., Harrigan, J.J., 2005. Discussion: 'The resistance of clamped sandwich beams to shock loading' (Fleck, N.A. and Deshpande, V.S., 2004, ASME J. Appl. Mech., 71, pp.386-401), *ASME J. Appl. Mech.* 72, 978 – 979.

Taylor, G.I., 1963a. The pressure and impulse of submarine explosion waves on plates, *The Scientific Papers of G.I. Taylor – Vol. III*, Cambridge Univ. Press, Cambridge, U.K., 287 – 303.

Taylor, G.I., 1963b. Pressures on solid bodies near an explosion, *ibid*, 260 – 267.

Wang, L., Labibes, K., Azari, Z., Pluvinage, G., 1994. Generalization of split Hopkinson pressure bar technique to use viscoelastic bars, *Int. J. Impact Engng.* 15, 669 – 686.

Wang, Z., Ma, H., Zhao, L., Yang, G., 2006. Studies on the dynamic compressive properties of open-cell aluminium alloy foams. *Scripta Mater.* 54, 83 – 87.

Yi, F., Zhu, Z., Zu, F., Hu, S., Yi, P., 2001. Strain rate effects on the compressive property and the energy-absorbing capacity of aluminium alloy foams. *Materials Characterization* 47, 417 – 422.

Yu, J.L., Li, J.R., Hu, S.S., 2005. Strain-rate effect and micro-structural optimization of cellular metals. *Mech. Mats.*, in press.

Zaretsky, E., and Ben-Dor, G., 1995. Compressive stress-strain relations and shock Hugoniot curves of flexible foams, *ASME J. Engng. Mat. Tech.* 117, 278 – 284.

Zhao, H., Elnasri, I., Abdennadher, S., 2005. An experimental study on the behaviour

under impact loading of metallic cellular materials, *Int. J. Mech. Sci.* 47, 757 – 774.

Zhu, H.X., Hobdell, J.R., Windle, A.H., 2001. Effects of cell irregularity on the elastic properties of 2D Voronoi honeycombs, *J. Mech. Phys. Solids* 49, 857 – 870.

APPENDIX A

Theory of the Split-Hopkinson pressure bar and Direct-impact tests

(A) Split-Hopkinson pressure bar (SHPB) test (Kolsky, 1953)

The one-dimensional wave equation is given by

$$\frac{\partial^2 u}{\partial X^2} = \frac{1}{c^2}\frac{\partial^2 u}{\partial t^2}. \tag{A1}$$

In the incident bar, the solution to Eqn. (A1) is

$$u_1(X,t) = f(X - ct) + g(X + ct) = u_i + u_r \tag{A2}$$

where f and g are arbitrary functions of the incident (subscript i) and reflected (subscript r) wave pulses and c is the elastic wave speed.
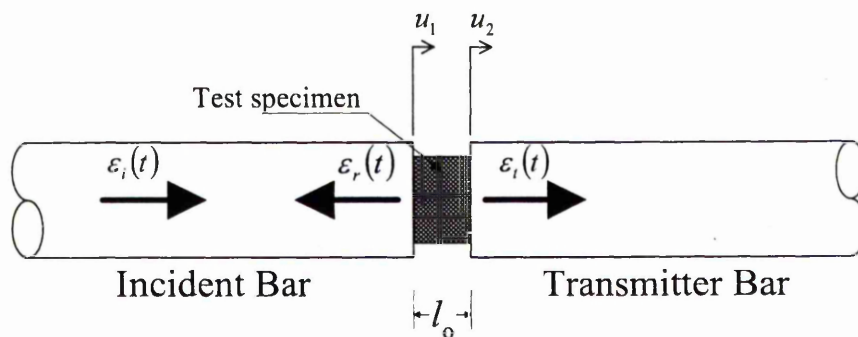

Figure A1 – Schematic of the incident bar, test specimen and transmitter bar in a SHPB setup

The strain in the incident bar is found by differentiating Eqn. (A2) with respect to X, while holding t fixed, to be

$$\varepsilon_1 = f' + g' = \varepsilon_i + \varepsilon_r. \tag{A3}$$

Note that all stresses and strains are treated as positive in compression and the subscripts 1 and 2 denote the incident and transmitter bar, respectively. Differentiating Eqn. (A2) with respect to t, while holding X fixed, and using Eqn. (A3) gives

$$\dot{u}_1 = c(-f' + g') = c(-\varepsilon_i + \varepsilon_r). \tag{A4}$$

Taking the time derivative of the displacement in the transmitter bar, $u_2 = h(X - ct)$, gives

$$\dot{u}_2 = -c\varepsilon_t. \tag{A5}$$

where the subscript t denotes transmitted pulse. The nominal engineering strain rate in the test specimen is given by

$$\dot{\varepsilon} = (\dot{u}_1 - \dot{u}_2)/l_o \tag{A6}$$

where $\dot{u}_1$ and $\dot{u}_2$ are the velocities at the incident bar-specimen and specimen-transmitter bar interfaces, respectively (see Fig. A1). Substituting Eqns. (A4) and (A5) into (A6) give

$$\dot{\varepsilon} = c(-\varepsilon_i + \varepsilon_r + \varepsilon_t)/l_o \tag{A7}$$

The forces at the incident bar – specimen and specimen – transmitter bar interfaces are, respectively,

$$F_1 = A_b E_b (\varepsilon_i + \varepsilon_r) \quad \& \quad F_2 = A_b E_b \varepsilon_t \qquad \text{(A8 \& A9)}$$

where A_b is the cross sectional area and E_b is the Young's modulus of the bars (both pressure bars are of identical material and cross sectional area).

Based on the assumptions that *the test specimen is always in force equilibrium and deforms uniformly*, i.e. $F_1 = F_2$, this gives

$$\varepsilon_t = \varepsilon_i + \varepsilon_r. \qquad \text{(A10)}$$

Using Eqn. (A10) with Eqn. (A7) gives

$$\dot{\varepsilon} = 2c\varepsilon_r / l_o \qquad \text{(A11)}$$

The average compressive stress in the test specimen is given by

$$\sigma_f = (F_1 + F_2)/2A_o \qquad \text{(A12)}$$

where A_o is the cross-sectional area of the test specimen. Substituting Eqns. (A8) and (A9) into (A12), and using (A10), gives

$$\sigma_f = E_b \left(\frac{A_b}{A_o} \right) \varepsilon_t \qquad \text{(A13)}$$

(B) Direct-impact test
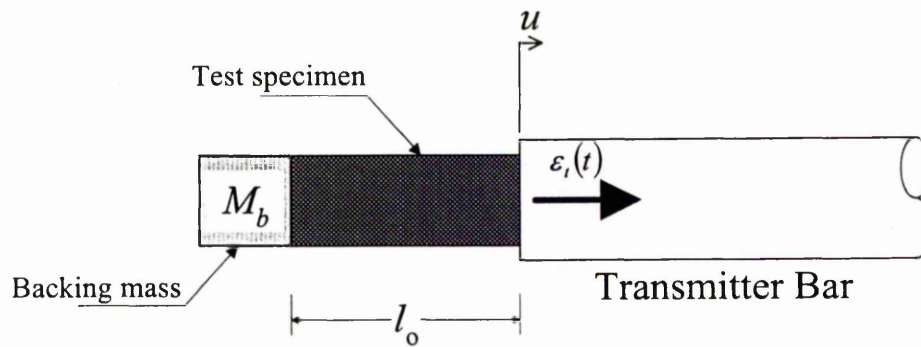
Figure A2 – Schematic of a direct-impact set-up.

The compressive stress in the test specimen is given by

$$\sigma_f = \frac{F_2}{A_o} = \frac{A_b}{A_o} E_b \varepsilon_t \tag{A14}$$

and the nominal engineering strain rate is defined as

$$\dot{\varepsilon} = V_i / l_o \tag{A15}$$

where V_i is the initial impact velocity of the foam projectile or the backing mass. Equations (A14) and (A15) are valid for both proximal and distal end impacts considered in Chapter 4.

APPENDIX B

Different forms of physical laws

A physical law can be expressed in various forms depending on the nature of the function in question. In the present thesis, compression of the foam rod is assumed to be unidirectional, along the OX axis (see Fig. 4.1); and from symmetry, the dependent variables can be expressed as functions of the Lagrangian co-ordinates (X,t) alone. Since there is dependence on just one space dimension X and time t, many of the physical laws are expressed in an integral form as follows (Bland, 1988):

$$F(X_1,t) - F(X_2,t) = \frac{d}{dt} \int_{X_1}^{X_2} G(X,t)dX + \int_{X_1}^{X_2} H(X,t)dX \qquad \text{(B1)}$$

where F, G and H are arbitrary functions of X and t; and X_1 and X_2 are constant values of X where $X_1 < X_2$. In the main body of this thesis, Eqn. (B1) may also appear in a differential and/or jump (or shock) forms as follows:

Case 1: Suppose both $\partial G/\partial t$ and $\partial F/\partial X$ exists.
Since $\partial G/\partial t$ exists, and X_1 and X_2 are constant, then

$$\frac{d}{dt} \int_{X_1}^{X_2} G(X,t)dX = \int_{X_1}^{X_2} \frac{\partial G}{\partial t}dX . \qquad \text{(B2)}$$

Writing $X_2 = X_1 + \Delta X$ and dividing Eqn. (B1) through by ΔX gives

$$\frac{1}{\Delta X}[F(X_1,t) - F(X_1 + \Delta X,t)] = \frac{1}{\Delta X}\frac{d}{dt}\int_{X_1}^{X_1 + \Delta X} G\cdot dX + \frac{1}{\Delta X}\int_{X_1}^{X_1 + \Delta X} HdX$$

$$\text{(B3)}$$

In the limit as $\Delta X \rightarrow 0$, and since $\partial F/\partial X$ exists, Eqn. (B3) can, therefore, be written as

$$-\frac{\partial F}{\partial X} + \frac{\partial G}{\partial t} + H = 0, \qquad (B4)$$

also know as the differential form of Eqn. (B1) (Bland, 1988).

Case 2: Suppose the function G has a discontinuity at $X_s(t)$ such that $X_1 < X_s(t) < X_2$ and $\partial G/\partial t$ exists everywhere else.

Separate the integral $\int_{X_1}^{X_2} G(X,t)dX$ into $\int_{X_1}^{X_s(t)}$ and $\int_{X_s(t)}^{X_2}$ so that

$$\frac{d}{dt}\left(\int_{X_1}^{X_s(t)} + \int_{X_s(t)}^{X_2} \right) G(X,t)dX = \int_{X_1}^{X_s(t)} \frac{\partial G}{\partial t}dX + G^-(X_s(t),t)\frac{dX_s(t)}{dt} +$$
$$\int_{X_s(t)}^{X_2} \frac{\partial G}{\partial t}dX - G^+(X_s(t),t)\frac{dX_s(t)}{dt} \qquad (B5)$$

where $G^-(X_s(t),t)$ and $G^+(X_s(t),t)$ denote the values of $G(X,t)$ immediately behind and ahead of the discontinuity, respectively. Substituting $X_2 = X_s(t)+\Delta X/2$ and $X_1 = X_s(t)-\Delta X/2$ into Eq. (B5) gives

$$F\left(X_s(t)-\frac{\Delta X}{2},t\right) - F\left(X_s(t)+\frac{\Delta X}{2},t\right) = \left(\int_{X_s(t)-\Delta X/2}^{X_s(t)} + \int_{X_s(t)}^{X_s(t)+\Delta X/2} \right)\frac{\partial G}{\partial t}dX +$$
$$\int_{X_s(t)-\Delta X/2}^{X_s(t)+\Delta X/2} HdX + V_s[G]$$

$$(B6)$$

where the symbol $[h] \equiv h^- - h^+$ denotes a jump in the dependent variable, say h, across the discontinuity and the superscripts $-$ and $+$ denote the region immediately behind and just ahead of the discontinuity, respectively; and the velocity of the propagating discontinuity is given by

$$V_s \equiv \frac{dX_s(t)}{dt} \qquad (B7)$$

In the limit as $X_1 \to X_s^-$ and $X_2 \to X_s^+$, Eqn. (B6) becomes (Bland, 1988)

$$[F] - V_s[G] = 0 , \qquad (B8)$$

also known as the jump form of Eqn. (B1). The jumps in Eqn. (B8) are strong discontinuities of the functions in Eqn. (B4).

Note that Eqns. (B1), (B4) and (B8) are the integral, differential and jump (or shock) forms of the same physical law. In general, any laws expressible in the form of Eqn. (B1) are often referred to as 'conservation' laws (Bland, 1988).

APPENDIX C

Hadamard's Lemma

Suppose the function $\phi(X,t)$ is defined and continuously differentiable, i.e. the partial derivatives of $\partial\phi/\partial X$ and $\partial\phi/\partial t$ is continuous everywhere, in a region of the X-t space except across the curve C. Let the suffix $+$ to denote the value of a variable just to the right of and below C and the suffix $-$ to the left and above. Define $[h] \equiv h^- - h^+$ as in Appendix A and d/dt be the time differentiation following curve C. Hadamard's lemma states that

$$\frac{d}{dt}[\phi] \equiv \left[\frac{d\phi}{dt}\right] = \left[\frac{\partial\phi}{\partial t}\right] + V_s\left[\frac{\partial\phi}{\partial X}\right]. \tag{C1}$$
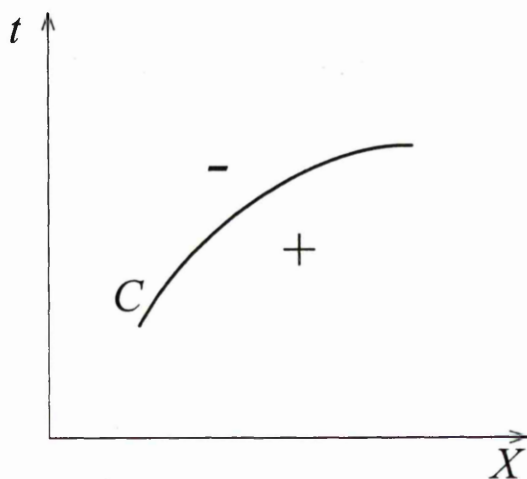
Hadamard's lemma imposes certain restrictions called *compatibility conditions* among various orders of discontinuities of ϕ. Its proof is similar to the one in classical analysis and can be found in Bland (1988).